## UNIVERSITY OF SOUTHAMPTON

## FACULTY OF ENGINEERING, SCIENCE & MATHEMATICS

## OPTOELECTRONICS RESEARCH CENTRE

# UV-written devices in rare-earth doped silica-on-silicon grown by FHD

by

Denis Alain Guilhot

Thesis submitted for the degree of Doctor of Philosophy

December 7, 2004

UNIVERSITY OF SOUTHAMPTON

## ABSTRACT

Faculty of Engineering, Science and Mathematics
Optoelectronics Research Centre

Doctor of Philosophy

# UV-written devices in rare-earth doped silica-on-silicon grown by FHD

By Denis A Guilhot

This thesis is concerned with the fabrication of all-UV-written devices in rare-earth doped silica-on-silicon to demonstrate the viability of this versatile single step channel definition process for the production of light sources.

The requirements for the glass substrate and the fabrication of waveguiding structures through use of the Flame Hydrolysis Deposition technique are discussed. The development of a process for rare-earth doping of the core layer through the immersion of a partially consolidated soot into a solution containing rare-earth ions is presented. The pre-requisites for direct-UV-writing of channels in a three-layer buried waveguide structure are then considered and results on the physical behaviour of the channels and spectroscopic properties of the rare-earth ions are reported. This study has resulted in the first demonstration of an all-UV-written waveguide laser in silica-on-silicon. Low-loss operation (0.11-0.3$dBcm^{-1}$) of a 10$mm$ long channel waveguide laser doped with 1.26$wt\%$ of neodymium was demonstrated with efficient lasing action ($\approx 33\%$ slope efficiency).

Erbium, ytterbium and thulium doping have been investigated to allow the production of light sources at other wavelengths. Further optimisation is still required to allow lasing to be achieved. Nevertheless, demonstration of y-splitters and Bragg grating fabrication in the doped material shows the potential of the combined fabrication techniques for the production of DFB laser-arrays for WDM technology. The additional developments required for the production of such devices are also discussed.

- Even a stopped clock gives the right time twice a day. -

Marwood, in *Withnail and I.*

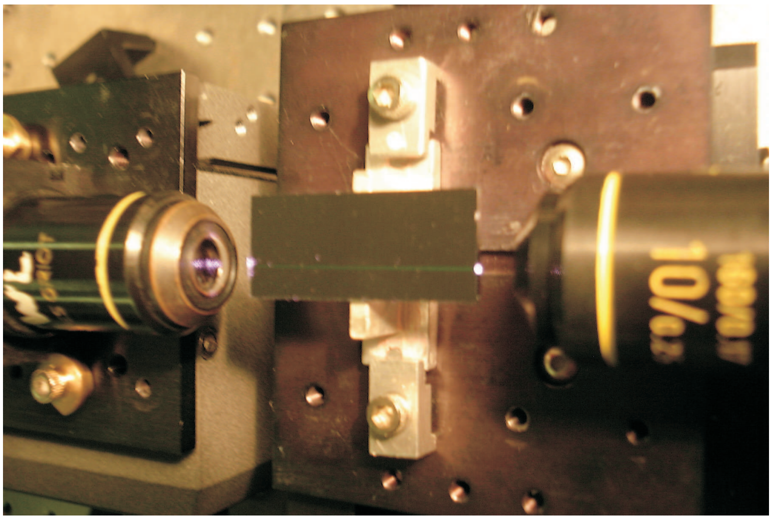

Figure 1: Pumping of an erbium doped channel waveguide

## Acknowledgements

This PhD was, in my view, performed as a concerto. I was only the composer and soloist and have required the assistance of a whole number of people. First of all, Peter Smith and Richard Williams, the conductor and the leader of the orchestra. Then the string section, Corin, Sam, Greg, Ian the piano man and Rafiq, helping to keep the direction of the piece and the show going. The drum section, from the technicians to the secretaries, without whom there would be no basis to the band. The horn section and the guest stars, giving their support and blowing life into the music, mainly the people from the Casa Loca (Em, MrT and all the others, thanks), Simon and Della, Taj, Angélique, Juliette, Yann, jeanKi and so many more. The spectators of course who managed to help in spite of the distance, all my friends and family.

None of this would have been possible without the mécènes, my parents, who trusted me even when I did not. Extra thanks to Taj and Simon for helping me out with the arrangements.

Finally, every piece has a Muse. Thanks Jenni babes.

# Contents

# Chapter 1

# Introduction and background to optical telecommunications

## 1.1 Integrated optics

The driving force behind integrated optics is the potential of optical communication to fulfill the increasing demand in bandwidth for telecommunications. Low loss transmission links are a primary requirement for long distance optical transmission. In 1966, Kao and Hockman demonstrated the first silica-based optical fibres with a sufficiently low propagation loss to enable their use as a communication medium [1]. This established the potential of optical communications for providing a high bandwidth, long distance data transmission network. Corning Glass Works were the first to produce an optical glass with a transmission loss of 20dBkm$^{-1}$ [2], which was thought to be the threshold value to permit efficient optical communications. Since then, silica-based optic fibres have become the preferred means of transmission in both long and short haul telecom networks. An all-optical network has the potential for a much higher data rate than a combined electrical and optical network and allows simultaneous transmission of multiple signals along one fibre optic link. This is achieved by encoding the different signals as different wavelengths, a process known as Wavelength Division Multiplexing (WDM).

The concept of integrated optics was first introduced by S.E. Miller in 1969 [3]. Integration allows different optical elements to be combined on a single substrate, which has many inherent advantages. Integrated optics avoid misalignment issues, as coupling between devices is achieved inside the substrate, and provide the compactness required for installation of devices in the network. The development of integrated optics technology has been relatively slow compared to fibre optic technology. Nevertheless, Planar Lightwave Circuits (PLC), which are ideal building blocks for integrated components, have begun to find application in telecommunications, such as the Arrayed Waveguide Grating (AWG) used for WDM channel separation. However, there is still a need for a number of integrated functions such as grating based wavelength selective filters, laser arrays for WDM applications or amplifiers.

A number of different glass hosts can be used for the development of integrated optics devices. When electro-optic effects are required, lithium niobate is a material of choice. Semiconductor technology can be used for integrated optics devices such as lasers, although the coupling with silica fibres is inefficient. Silica-on-silicon has a number of advantages that makes it a material of predilection. The minimum transmission loss in silica, occurring in the third transmission window around 1550nm, is lower than that reported in other materials. Nowadays, the losses can be as low as 0.148dB$\text{km}^{-1}$ at 1550nm in silica fibres [4] and 0.05dB$\text{cm}^{-1}$ [5] for channel waveguides. If needed, electronic and optical devices can be integrated in the same sample using both the substrate and the glass layers. Also, because of the compatibility with the existing fibre network, coupling losses can be minimised compared to that of other materials.

## 1.2 Rare-earth doped waveguide lasers

The laser was invented in 1960 [6] and provided a suitable light source for optical communication technology to develop, which helped convince people of fibre's relevance. The first laser was flashlamp pumped with a cavity formed from a ruby crystal. Ever since, considerable research has been directed towards glass based lasers, as glass is both mechanically stable and relatively low cost. An inherent benefit of glass-based lasers is that their refractive index is generally relatively close to that of the existing silica fibre network. Glass can act as an amplifying medium by bulk-doping with an optically active element, such as a rare-earth ion, followed by pumping with light of an appropriate wavelength. The pump wavelength is converted by the rare-earth ions, generally towards longer, but in some cases also shorter laser wavelengths (e.g.: upconversion lasers). A range of lasing wavelengths, which to date covers most of the spectrum from Ultra Violet (UV) to mid infrared [8], can be obtained by doping glasses with different ions.

The first demonstration of laser action in a rare-earth doped waveguide was reported in 1961 [9]. The waveguide consisted of two concentric glass rods, a neodymium-doped barium crown glass core and a soda-lime silicate cladding. The refractive index of the inner rod was designed to be higher than that of the outer rod, so that the confinement offered by this design could be used to overcome the poor quality of the glass. Total internal reflection at the boundary of the waveguide prevents the light from diverging, which reduces the cavity mode volume and therefore the pump power required to reach threshold [10]. The first rare-earth-doped glass laser in planar geometry was realised 11 years later, in 1972 [11]. Coherent emission was obtained from holmium ions in an aluminium garnet crystal, however, the laser needed cooling and required a high pump power to reach threshold. This result was followed a year later by the report of the first room temperature operation of a neodymium doped silica fibre geometry laser [12]. The first planar glass waveguide laser was demonstrated in 1989 and used a silica-on-silicon design with a neodymium doped core [13].

The waveguide geometry has inherent advantages for laser devices. Not only does it reduce the threshold power of a laser but it also provides compact devices that are immune to cavity misalignment. The waveguide geometry also allows the use of certain low-gain transitions that cannot be implemented in bulk materials, due to excessively high thresholds [14]. It also considerably reduces the problem of thermal effects, encountered in bulk, and allows high power densities to be obtained due to its small size [15]. The planar waveguide geometry can offer an even lower sensitivity to these effects than optical fibres [16]. They are also naturally compatible with planar lightwave circuits and the asymmetric output of diode lasers, which allows pumping, in some cases with no coupling optics [17].

## 1.3 Existing state of research at the start of the PhD

At the outset of this PhD, the Flame Hydrolysis Deposition (FHD) equipment was already installed at the ORC [18]. Phosphosilicate layers, germanosilicate and boro-germanosilicate layers had been previously deposited on silica and silicon substrates. The simultaneous doping of layers with germanium, phosphorus and boron was not possible until the installation of a boron trichloride supply by the author. This has further standardised the deposition of layers and has increased the composition flexibility, as all three dopants are available at any time. The result is a more accurate control of the refractive index and consolidation temperature of the deposited layers. The PhD thesis of Sam Watts [18] reports the creation of a three-layer index-matched structure that was used during the course of this work for UV-writing of waveguides. Other general modifications have been carried out on the system such as designing and replacing the burner gas supply system with a more accurate device which increased the homogeneity of the layers. At present, a layer thickness of 5 to 16 $\mu m$ can be obtained, with a thickness variation of 200 to 500nm on a 50 millimeter square sample, and a roughness of 50 to 70nm. Further details on this subject, and the FHD system itself, can be found in chapter 3.

Solution doping was developed in the ORC for fibre technology. However, the technology had not been applied to the planar format at the ORC. A goal of this thesis was to complete solution doping in a planar geometry. The UV writing set up was already working and producing channels. Finally, although the numerical aperture, grating and laser characterisation experiments were established, there was no facility for the study of the spectroscopy of planar samples. This had to be installed by the author before measurements could be made.

## 1.4 Aim of the research

The main aim of this research was to design, demonstrate and investigate the process of rare-earth solution doping of FHD layers, and compare their response to UV writing to that of undoped samples. The completion of this objective can be separated into a number of stages. First of all, the standard solution doping technique had to be adapted to the planar format. The preliminary experiments were performed using boron and aluminium to acquire some knowledge of the solution doping method. Active layers were then fabricated using different rare-earth ions, namely erbium, neodymium, thulium and ytterbium. Waveguides and Bragg gratings were then defined using the direct UV-writing technique. Doped and undoped channels were subsequently analysed to characterise the differences in behaviour of active and passive layers when submitted to UV writing. Finally, during the course of this work, the first all-UV-written waveguide laser in silica-on-silicon was produced.

## 1.5 Outline of the thesis

The remainder of this thesis will describe the work carried out during this PhD project. After outlining the relevant theory, the results of the experiments necessary to the development of the samples will be related in a chronological order.

The basic theory of light propagation in an optical waveguide is described in chapter 2. The propagation in a symmetric three-layer slab waveguide is studied before an introduction to propagation in a channel waveguide. An overview of rare-earth ions is included. Finally the equations that govern laser theory are presented, and equations for the expression of threshold power and slope efficiency are derived.

Fabrication of the planar layers by FHD is described in chapter 3. This includes a review of existing techniques available for the fabrication of rare-earth doped glass and rare-earth doping of silica. A brief description of the advantages of silica-on-silicon technology over other glasses is also included. The principles of FHD, and a description of the existing FHD system are reported alongside the modifications performed by the author. Finally, the layer compositions fabricated during the course of this work are detailed.

The principles of the solution doping of planar waveguide layers forms the core of chapter 4. Initially, the principles of solution doping and soot sintering are described, followed by a comparison of the different experimental set ups developed. The results obtained for aluminium doping and rare-earth doping are reviewed. Finally, the influence of consolidation temperature upon layer quality is discussed.

Reactive ion etching followed by photolithography, a possible method for channel definition in an existing layer, is summarised and compared to UV-writing in chapter 5. The system used for UV-writing is described, and the results obtained from the characterisation of the channels are presented. Finally, experiments are performed to illustrate the feasibility of y-splitters, and the results are listed.

Chapter 6 begins with a review of planar UV-written waveguide lasers. The absence of lasing, observed from some samples, is discussed. The lasing characteristics of the UV-written neodymium doped waveguide lasers fabricated in silica-on-silicon are then reported. Finally, different methods for the calculation of the waveguide propagation loss are described.

An overview of the theory behind Bragg gratings is detailed in chapter 7, and is followed by a review of grating definition techniques. The remainder of the chapter is dedicated to a comparison of gratings in undoped and rare-earth doped samples, which were produced by the FHD system. The results are compared to a model, which allows an assessment of the refractive index dependence on wavelength and the dispersion of the neodymium doped silica layer.

In chapter 8, the work presented in this thesis is summarised. Conclusions are drawn and possible future work is suggested. The optimisations necessary for the creation of DFB rare-earth doped UV-written lasers in silica-on-silicon are discussed.

## 1.6 References

[1] K.C. Kao and G.A. Hockham. Dielectric-fibre surface waveguides for optical frequencies. *Proceedings of the IEE*, 113(7) : p1151–1158, 1966.

[2] F.P. Kapron, D.B. Keck and R.D. Maurer. Radiation losses in glass optical waveguides. *Applied Physics Letters*, 187 : p423–425, 1970.

[3] S.E. Miller. Integrated Optics: an introduction. *The Bell System Technical Journal*, 48(7) : p2059–2069, 1969.

[4] G. Brambilla, V. Finazzi and D.J. Richardson. Ultra-low-loss optical fiber nanotapers. *Optics Express*, 12(10) : p2258–2263, 2004.

[5] R.A. Bellman, G. Bourdon, G. Alibert, A. Beguin, E. Guiot, L.B. Simpson, P. Lehuede, L. Guiziou and E. LeGuen. Ultralow lowss high delta silica germania planar waveguides. *Journal of the Electrochemical Society*, 151(8) : pG541–G547, 2004.

[6] T. Maiman. Stimulated optical radiation in ruby. *Nature*, 187 : p493–494, 1960.

[7] R.J. Mears, L. Reekie, I.M. Jauncey and D.N. Payne. Low-noise erbium-doped fibre amplifier operating at 1.54 $\mu m$. *Electronics Letters*, 23(19) : p1026–1028, 1987.

[8] W. Koechner. Solid-state laser engineering, Chap. 2. *Springer Verlag*, 1999.

[9] E. Snitzer. Optical maser action of neodymium in a barium crown glass. *Physical Review Letters*, 7(12) : p444–446, 1961.

[10] C.J. Koester and E. Snitzer. Amplification in a fiber laser. *Applied Optics*, 3(10) : p1182–1186, 1964.

[11] J.P. Van der Ziel, W.A. Bonner, L. Kopf and L.G. Van Uitert. Coherent emission from $Ho^{3+}$ ions in epitaxially grown thin aluminium garnet films. *Physics Letters*, 42A(1) : p105–106, 1972.

[12] J. Stone and C.A. Burrus. Neodymium-doped silica lasers in end-pumped fiber geometry. *Applied Physics Letters*, 23(7) : p388–389, 1973.

[13] Y. Hibino, T. Kitagawa, M. Shimizu, F. Hanawa and A. Sugita. Neodymium-doped silia optical waveguide laser on silicon substrate. *IEEE Photonics Technology Letters*, 1(11) : p349–350, 1989.

[14] D.C. Hanna, A.C. Large, D.P. Shepherd, A.C. Tropper, I. Chartier, B. Ferrand and D. Pelenc. A side-pumped $NdY_3Al_5O_{12}$ epitaxial waveguide laser. *Optics Communications*, 91 : p229–235, 1992.

[15] J.E. Townsend. The development of optical fibres doped with rare-earth ions. *PhD thesis, University of Southampton*, 1990.

[16] J.M. Eggleston, T.J. Kane, K. Khun, J. Unternahrer and R.L. Byer. The slab geometry laser - part I: theory. *IEEE Journal of Quantum Electronics*, QE-20(3) : p289–301, 1984.

[17] C.L. Bonner, T. Bhutta, D.P. Shepherd and A.C. Tropper. Double-Clad Structures and Proximity Coupling for Diode-Bar-Pumped Planar Waveguide Lasers. *IEEE Journal of Quantum Electronics*, 36(2) : p236–242, 2000.

[18] S.P. Watts. Flame Hydrolysis Deposition of photosensitive silicate layers suitable for the definition of waveguiding structure through direct ultraviolet writing. *PhD thesis, University of Southampton*, 2002.

# Chapter 2

# Elements of waveguide and laser theory

## 2.1 Introduction

The theory necessary to the understanding of rare-earth doped laser waveguides is outlined in this chapter. For a more detailed account, the reader is directed to the literature in particular Lee for waveguide theory [1] and Fan or Risk for the model of lasing action [2,3].

The chapter is set-out as follows: the 3-layer slab waveguide is introduced followed by the electromagnetic theory of the allowed modes of propagation in this waveguide. The wave equation and the guidance conditions are examined for both transverse electric (TE) and transverse magnetic (TM) modes. The Marcatili method and effective index methods are introduced for an approximation of the propagation phenomenon in a channel waveguide. Rare-earth ions are then reviewed before the quasi-three level model of laser action in rare-earth ions is introduced, which can be applied to three and four level transitions. Starting from the rate equations, expressions for the threshold power and the slope efficiency are derived and then applied to the specific case of end pumped waveguide lasers.

## 2.2 Modes in planar geometry

### 2.2.1 Introduction to the symmetric 3-layer slab waveguide

An understanding of the physics of light propagation in a waveguide can most readily be gained by studying the 3-layer symmetric slab whilst more complicated structures, such as channel waveguides, require numerical modelling. As shown in figure 2.1, the slab consists of three superposed layers of different refractive indices. The outer layers form the cladding of the waveguide and are of the same refractive index, while the central layer (the core) has a refractive index that is higher than that of the cladding to allow optical guidance to occur. In the y and z directions, there is no refractive index variation as the waveguide is assumed to extend infinitely. Therefore, the slab waveguide is made of two regions : the cladding, which is characterised by its permittivity and permeability $\epsilon_1$ and $\mu_1$, and is located at $|x| > |D/2|$ and the core located at $|x| < |D/2|$, with $\epsilon_2$ and $\mu_2$. The refractive index of each region m can be expressed as:

$$n_m = \sqrt{\frac{\epsilon_m}{\epsilon_0}} \tag{2.1}$$

Where $\epsilon_0$ is the permittivity of free space and $\mu = 1$.

Each possible mode of propagation is a set of electromagnetic fields which maintain their transverse spatial distribution whilst propagating. The structure has two distinct polarisation states [4]:

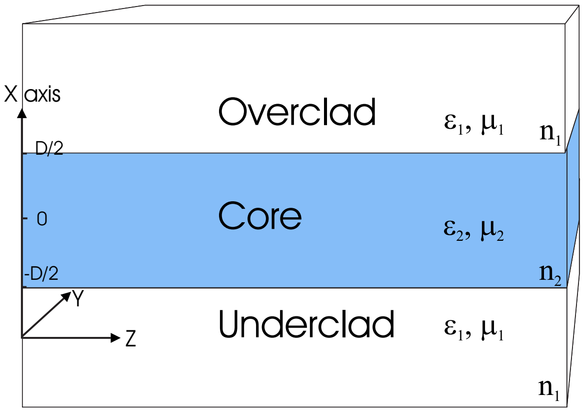

Figure 2.1: Schematic of 3-layer slab waveguide

- transverse electric (TE) where the E field is polarised in the y-direction i.e. $E_x = E_z = 0$ and $H_z \neq 0$.
- transverse magnetic (TM) where the H field is polarised in the y-direction i.e. $H_x = H_z = 0$ and $E_z \neq 0$.

### 2.2.2 Electromagnetic theory : the wave equation

The spatial distribution of the modes within a waveguide can be determined using Maxwell's equations as a starting point. For a linear isotropic charge-free medium the electric (E) and magnetic (H) field vectors are linked by the following forms of Maxwell's equation :

$$\nabla \times \underset{\sim}{E} = -\mu \frac{\partial}{\partial t} \underset{\sim}{H} \tag{2.2}$$

$$\nabla \times \underset{\sim}{H} = \varepsilon \frac{\partial}{\partial t} \underset{\sim}{E} \tag{2.3}$$

$$\nabla \cdot \underset{\sim}{E} = 0 \tag{2.4}$$

$$\nabla \cdot \underset{\sim}{H} = 0 \tag{2.5}$$

Where $\mu$ and $\varepsilon$ are the permeability and permittivity of the medium, $\partial/\partial t$ is the partial derivative with respect to time $t$ and $\nabla$ is the spatial vector operator:

$$\nabla = \frac{\partial}{\partial x}\hat{x} + \frac{\partial}{\partial y}\hat{y} + \frac{\partial}{\partial z}\hat{z} \tag{2.6}$$

Taking the curl of equation 2.2 and using the vector identity (where $\underset{\sim}{U}$ is any vector) :

$$\nabla \times \left(\nabla \times \underset{\sim}{U}\right) = \nabla \left(\nabla \cdot \underset{\sim}{U}\right) - \nabla^2 \underset{\sim}{U} \tag{2.7}$$

leads to :

$$\nabla\left(\nabla\cdot\underset{\sim}{E}\right)-\nabla^2\underset{\sim}{E}=-\mu\frac{\partial}{\partial t}\nabla\times\underset{\sim}{H} \tag{2.8}$$

Using equations 2.3 and 2.4 allows us to derive the homogeneous wave equation to be calculated in terms of the E field. This equation relates the spatial and temporal components of the E field in a loss-less dielectric medium:

$$\nabla^2\underset{\sim}{E}-\epsilon\mu\frac{\partial^2}{\partial t^2}\underset{\sim}{E}=0 \tag{2.9}$$

The wave equation can also be expressed in terms of the H field by applying the same reasoning to equation 2.3. The same equation is obtained in terms of H instead of E:

$$\nabla^2\underset{\sim}{H}-\epsilon\mu\frac{\partial^2}{\partial t^2}\underset{\sim}{H}=0 \tag{2.10}$$

Solving the wave equation is simplified by allowing the radiation to propagate along the z-axis as this eliminates the spatial variation of the field along this axis. For radiation propagating along the z-axis, the following general form of the solutions can be assumed [6]:

$$E=(E_x(x,y)\hat{\mathbf{x}}+E_y(x,y)\hat{\mathbf{y}}+E_z(x,y)\hat{\mathbf{z}})e^{i(\omega t-\beta z)} \tag{2.11}$$

$$H=(H_x(x,y)\hat{\mathbf{x}}+H_y(x,y)\hat{\mathbf{y}}+H_z(x,y)\hat{\mathbf{z}})e^{i(\omega t-\beta z)} \tag{2.12}$$

where $\beta$ is the mode propagation constant and $\omega$ the angular frequency. The unit vectors in each direction are $\hat{\mathbf{x}},\hat{\mathbf{y}}$ and $\hat{\mathbf{z}}$, while $E_x, E_y$ and $E_z$ are the relative magnitude coefficients of the electric field in the x, y and z directions respectively and $H_x, H_y$ and $H_z$ those of the relative magnitude coefficients of the magnetic field. The field does not have a z dependence as it is the axis of propagation. The solutions can be calculated by using the continuity condition at the interfaces. The mathematics needed in the following derivations can be simplified by using the concept of duality. It has been found that by making the substitutions $-H\rightarrow E$, $E\rightarrow H$, $\mu\rightarrow\varepsilon$ and $\varepsilon\rightarrow\mu$, the solutions calculated for one field can be used for the other one thanks to the symmetry of Maxwell's equations [1].

### 2.2.3 Solution for a symmetric waveguide

As seen in subsection 2.2.1, the structure considered here offers a step-index between core and cladding with the refractive index of the cladding lower than the refractive index of the core, and extends indefinitely in the y and z directions. Hence, using equation 2.9, the two mutually orthogonal polarization states : Transverse Electric (TE) and Transverse Magnetic (TM) supported by this structure can be calculated. They have to be considered separately. Their non-zero field components are listed in table 2.1, on the left side for TE and on the right side for TM [7].

| TE mode | TM mode |
|---|---|
| $E_y$ | $H_y$ |
| $H_x = -\frac{\beta}{\omega\mu_0}E_y$ | $E_x = \frac{\beta}{\omega\epsilon_0 n^2}H_y$ |
| $H_z = -\frac{1}{i\omega\mu_0}\frac{\partial}{\partial x}E_y$ | $E_z = \frac{1}{i\omega\epsilon_0 n^2}\frac{\partial}{\partial x}H_y$ |

Table 2.1: TE and TM mode field components

These will be used in the following derivations to obtain solutions for the TE and TM modes separately using also the continuity conditions across the waveguide boundaries.

#### 2.2.3.1 Transverse Electric mode solutions

For the TE modes, the x and z components of the E field are zero. Hence, the expression of the field can be written as:

$$\underset{\sim}{E} = E_y(x)e^{i(\omega t-\beta z)} \tag{2.13}$$

Due to the symmetry of the structure the decay in both cladding layers must be the same and the modes are expected to be symmetric or anti-symmetric around the position $x = 0$. Within the core, $E_y$ is assumed to be oscillatory. Consequently, the proposed TE solutions are as follows [1]:

$$E_y(x,z) = E_{y0}\left\{\begin{array}{l} Ae^{-\alpha x} \\ \cos{(kx)}\text{even} \\ \sin{(kx)}\ \text{odd} \\ \pm Ae^{-\alpha x} \end{array}\right\}\begin{array}{l} x > D/2 \\ \\ D/2 \geqslant x \geqslant -D/2 \\ \\ x < -D/2 \end{array} \tag{2.14}$$

Where $A$ is a relative amplitude coefficient for the solutions in each region of the waveguide, $\alpha$ is the decay coefficient for the over and undercladding, $k$ is the transverse wavevector within the core and $E_{y0}$ is the maximum amplitude of the electric field in the y-direction. Combining equation 2.14 and equation 2.13 gives us the complete TE E field solution. Inserting this solution into the E field wave equation leads to the following conditions, if the expression defined for the cladding layers is used:

$$\alpha^2 = \beta^2 - \omega^2\mu_1\epsilon_1 \tag{2.15}$$

and if the expression defined for the core layer is used:

$$\kappa^2 = \omega^2\mu_2\epsilon_2 - \beta^2 \tag{2.16}$$

The propagation constant $\beta$ is just the effective wavenumber for a given mode and so must be constant. Thus, the guidance condition can be derived from equation 2.15 and 2.16 and expressed in the form:

$$\kappa^2 + \alpha^2 = \omega^2(\mu_2\epsilon_2 - \mu_1\epsilon_1) \tag{2.17}$$

The boundary condition states that across the two boundaries ($x = \pm D/2$) H and E must be continuous. Maxwell's equations show that the longitudinal component of both fields satisfy this condition. Therefore, only the tangential components $E_y$ and $H_z$ of the fields will be considered here with boundary conditions identical at $x = \pm D/2$. Using the expression from table 2.1 for $E_y$ and the solutions from equation 2.14 yields:

$$Ae^{-\alpha\frac{D}{2}} = cos(\frac{\kappa D}{2}) \tag{2.18}$$

Using the expression from table 2.1 for $H_z$ gives :

$$H_z = -\frac{1}{i\omega\mu_0}\frac{\partial}{\partial x}E_y \tag{2.19}$$

and using the solutions from equation 2.14, the z component of the H field within the waveguide can therefore be expressed as:

$$H_z(x,z) = \left\{ \begin{array}{l} \frac{i\alpha}{\omega\mu_1} A e^{-\alpha x} E_{y0} \\ \frac{ik}{\omega\mu_2} \sin(kx)\, E_{y0} \\ -\frac{ik}{\omega\mu_2} \cos(kx)\, E_{y0} \\ \pm\frac{i\alpha}{\omega\mu_1} A e^{-\alpha x} E_{y0} \end{array} \right\} e^{-i\beta z} \quad \begin{array}{l} x > D/2 \\ \\ D/2 \geqslant x \geqslant -D/2 \\ \\ x < -D/2 \end{array} \tag{2.20}$$

Using the boundary condition once more leads to:

$$\frac{1}{\mu_1}\alpha A e^{-\frac{\alpha D}{2}} = \frac{\kappa}{\mu_2} sin(\frac{\kappa D}{2}) \tag{2.21}$$

The unknown A can be eliminated by taking the ratio of equations 2.18 and 2.21 and the guidance conditions for the even modes to propagate becomes:

$$\frac{\mu_2 \alpha}{\mu_1 \kappa} = tan(\frac{\kappa D}{2}) \tag{2.22}$$

Applying the same procedure to odd modes gives the conditions the mode has to satisfy to propagate:

$$\frac{\mu_2 \alpha}{\mu_1 \kappa} = cot(\frac{\kappa D}{2}) \tag{2.23}$$

The values of $\alpha$ and $\kappa$ can be determined by solving these two equations numerically or graphically in conjunction with the wavenumber condition for a given waveguide structure. Substituting them in equation 2.18 gives a value for the amplitude coefficient $A$. The shape of the mode profile can then be determined by replacing $A$, $\alpha$ and $\kappa$ by their value in the proposed solutions (equation 2.20). Each solution of the guidance conditions gives an allowed guided propagation mode.

#### 2.2.3.2 Transverse Magnetic mode solutions

The principle of duality has been mentioned earlier. It allows the TM mode solutions to be deduced from the previous results rather than proceeding with the same arguments and conditions used in the previous section. Replacing $\epsilon$ by $\mu$ and E by H in the equations gives the guidance conditions for even (eq. 2.24) and odd (eq. 2.25) TM modes. Thus it follows that:

$$\frac{\epsilon_2 \alpha}{\epsilon_1 \kappa} = \tan(\frac{\kappa D}{2}) \tag{2.24}$$

$$\frac{\epsilon_2 \alpha}{\epsilon_1 \kappa} = \cot(\frac{\kappa D}{2}) \tag{2.25}$$

And the proposed TM solutions can be deduced by replacing $E$ for $H$:

$$H_y(x,z) = H_{y0} \left\{ \begin{array}{l} Ae^{-\alpha x} \\ \cos{(k_x x)}\text{even} \\ \sin{(k_x x)}\ \text{odd} \\ \pm Ae^{-\alpha x} \end{array} \right\} \begin{array}{l} x > D/2 \\ \\ D/2 \geqslant x \geqslant -D/2 \\ \\ x < -D/2 \end{array} \tag{2.26}$$

Values of $\alpha$ and $\kappa$ can be determined by numerically solving 2.24 and 2.25 and substituing these values into 2.26 to determine the TM mode profiles.

## 2.3 Channel waveguide

The study of propagation of light in a three-layer slab waveguide provides an understanding of the physical phenomenon of guidance and of the parameters influencing it but is quite limited in the sense that the geometry used in this work is that of a channel waveguide. The guidance afforded in this case is the result of a confinement in both the x and y direction. The different refractive indexes in the x direction are due to the three layers of different materials. The direct-UV-writing process induces an additional refractive index-difference in the y direction in all three layers as they all are photosensitive. The resulting structure can be viewed as a two-dimensional grid of refractive index when seen in the z direction, as shown in figure 2.2.

The propagation through this type of structure generally cannot be analytically solved but requires numerical treatment, except for some cases with very simplified structures. To that effect, a number of methods have

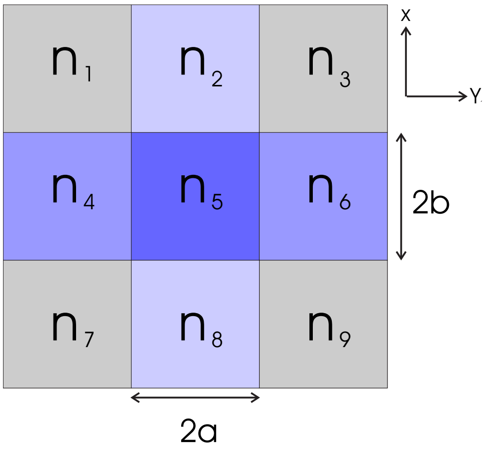

Figure 2.2: Schematic of channel waveguide

been developed such as the finite elements method and the finite difference method [8]. The draw-back to these methods is that they are quite computationally intensive. Cruder approximations can be obtained using methods such as the *Marcatili* and *effective index* methods which are still reasonably accurate.

*Marcatili*'s method is still commonly used although it was proposed in 1969 [9]. It considers that the light is confined to the core area so $n_1, n_3, n_7$ and $n_9$ can be ignored as the electric and magnetic fields are assumed not to exist in these areas (see figure 2.2). Another assumption is that the other four areas surrounding the core region are of equal refractive index. Hence, the continuity conditions only need to be applied to these four cladding-core interfaces. Because of the techniques used for the fabrication of channel waveguides used during the course of the work related in this thesis, this method is not well suited to the structures discussed and the *effective index* method was preferred for the modelling reported in chapter 7.

The *effective index* method is an extension of the 3-layer slab optical waveguide analysis [10]. Due to the channel geometry, the mode propagates along a medium with a refractive index $n(x, y)$ which depends on the coordinates of the point examined. The effective refractive index of the waveguide can therefore be considered as an average over the refractive index of the medium [5]. The two dimensional optical waveguide is considered to be a combination of three slab waveguides. The analysis is applied to each slab in the y-direction in turn to calculate their effective index. Hence, the system with refractive index $n_1$, $n_2$ and $n_3$ is solved, then the system with $n_4$, $n_5$ and $n_6$ then $n_7$, $n_8$ and $n_9$. This gives a new system of three regions of different refractive index. The method is then applied to the resulting slab waveguide in the x-direction with each area having the calculated effective refractive index. Solving this slab gives an estimation of the actual effective index of the channel.

## 2.4 Rare-earth doped laser theory

### 2.4.1 Introduction

The following sections introduce rare-earth ions and describe the theoretical laser operation of a rare-earth (RE) doped waveguide laser. The quasi-three level model, first described by Fan [2], is used to explain the laser behaviour. It is a powerful tool for describing laser operation as it is applicable to three, quasi-three and four-level laser transitions.

### 2.4.2 Rare-earth ions

Rare-earth ions have been used extensively in optics since the first rare-earth doped glass laser using neodymium ions was fabricated [11]. They have important characteristics that lead to excellent performance in laser and amplifier applications [12], mainly narrow emission lines and long lifetime of the metastable states. Also, the absorption and emission characteristics of the ion are relatively unaffected by the host. All these characteristics are due to the fact that it is energetically more favourable for electrons to fill the outer lying $5s$ and $5p$ electron shells than the inner $4f$ electron shells [13].

In the work done for this thesis, four rare-earth ions have been used, namely neodymium (Nd), erbium (Er), thulium (Tm) and ytterbium (Yb).

These laser ions are all related to the idealised quasi-three-level and four-level energy level diagrams shown in figure 2.3.

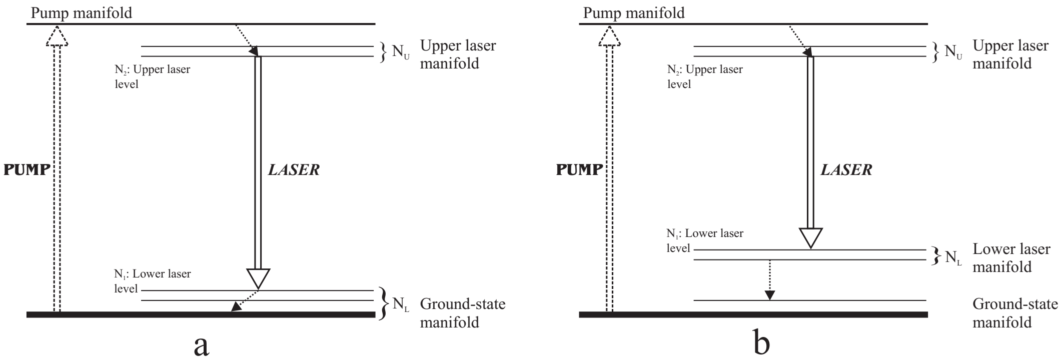

Figure 2.3: Idealised energy levels of: a/ quasi-three-level laser, b/ four-level laser

### 2.4.3 Quasi-Three Level Laser Operation

By absorption of a photon produced by a pump laser, a rare-earth ion can be excited from the ground-state to the pump manifold. The excited ion then decays non-radiatively to the upper laser level $N_2$, which is a lower lying Stark level of the upper laser manifold. Lasing occurs between this level and the lower laser level $N_1$, which is one of the higher lying Stark levels of the lower laser manifold. Due to the rapid non-radiative relaxation between the Stark split levels, the populations of each Stark level within a manifold are said to be in quasi-thermal equilibrium, and therefore can be modelled with a Boltzmann distribution [14]. The quasi-three-level theory is applied to a four level laser by assuming that the lower laser level is unpopulated (i.e. $N_L = N_1 = 0$). This can only occur if the lower laser level is not part of the ground-state manifold. In this case, after the lasing transition, the ion then decays non-radiatively from the level in the lower laser manifold to the ground state.

If the total population density of the lower laser manifold is called $N_L$ and $f_1$ is the fraction of the total population within the appropriate Stark level of the lower laser manifold, the population density of the lower laser level $N_1$ can be expressed as [3]:

$$N_1 = f_1 N_L \tag{2.27}$$

Similarly, for the upper laser manifold $N_2$, if $N_U$ is the total population density and $f_2$ the fraction of the total population within the appropriate Stark level of the upper laser manifold, the population density can be expressed as:

$$N_2 = f_2 N_U \tag{2.28}$$

The energy gap between the upper and lower laser level is assumed to be large enough that in equilibrium (i.e. no pumping), the upper laser level is unpopulated (i.e. $N_U^0 = N_2^0 = 0$) and the lower laser level population is described by $N_1^0 = f_1 N_L^0$ where the superscript is used to denote the equilibrium values of the population. Spatial hole burning is neglected, and it is assumed that there is negligible depopulation of the ground state.

#### 2.4.3.1 Rate equation

For both the upper and lower levels, the change in population density with time can be described by the steady-state rate equation [3]:

$$\begin{aligned}&\frac{\partial N_U(x,y,z)}{\partial t} = \\ &\eta_p r(x,y,z) - \frac{N_U(x,y,z)}{\tau} - c_n \sigma [N_2(x,y,z) - N_1(x,y,z)]\phi(x,y,z) = 0\end{aligned} \tag{2.29}$$

$$\begin{aligned}&\frac{\partial N_L(x,y,z)}{\partial t} = \\ &-\eta_p r(x,y,z) + \frac{N_U(x,y,z)}{\tau} + c_n \sigma [N_2(x,y,z) - N_1(x,y,z)]\phi(x,y,z) = 0\end{aligned} \tag{2.30}$$

Where $\eta_p$ is the pump quantum efficiency, $r(x,y,z)$ is the pump rate density, $\tau$ is the upper laser level lifetime, $c_n$ is the speed of light in the waveguide, $\sigma$ is the gain cross-section and $\phi(x, y, z)$ is the laser photon density. The first term on the right side of the equation represents the number of electrons removed from the lower level and added to the higher level by pumping per second, the second term represents the spontaneous emission rate and the third term is the stimulated emission rate. By integrating the pump rate density and the laser photon density over the waveguide cavity, the total pump rate $R$ and the total number of laser photons $\Phi$ can be defined as:

$$\iiint\limits_{cavity} r(x, y, z)\partial x\partial y\partial z = R\,; \iiint\limits_{cavity} \phi(x, y, z)\partial x\partial y\partial z = \Phi \tag{2.31}$$

These two parameters can be expressed as follows:

$$\begin{aligned} R &= \frac{P_p}{h\nu_p} \\ \Phi &= \frac{2l_c P_l}{c_n h\nu_l} \end{aligned} \tag{2.32}$$

Where $P_p$ is the absorbed pump power, $h$ is Planck's constant, $\nu_p$ is the pump frequency, $l_c$ is the cavity length, $P_l$ is the laser power travelling in one direction, $c_n$ is the speed of light in the waveguide, and $\nu_l$ is the laser frequency. The factor 2 arises because $P_l$ is the number of photons travelling in one direction while $\Phi$ is the total number of laser photons, i.e. travelling in both directions.

The evolution of the number of photons in the cavity with time can be expressed as [3]:

$$\frac{\partial\Phi}{\partial t} = c_n\sigma \iiint\limits_{cavity} [N_2(x, y, z) - N_1(x, y, z)]\phi(x, y, z)\partial x\partial y\partial z - \frac{\Phi}{\tau_c} = 0 \tag{2.33}$$

Where $\tau_c = 2l_c/c_n(L+T)$ is the cold cavity photon lifetime (i.e. the time taken for $\Phi$ to fall to $\frac{1}{e}$ of its initial value in a passive cavity), $L$ is the round trip waveguide loss and $T$ is the output coupling.

Using normalised spatial distributions:

$$\iiint\limits_{cavity} r_p(x,y,z)dxdydz = 1 \quad \iiint\limits_{cavity} \phi_l(x,y,z)dxdydz = 1 \tag{2.34}$$

the pump rate density $r$ and the laser photon density $\phi$ can be expressed as:

$$r(x,y,z) \equiv Rr_p(x,y,z) \text{ and } \phi(x,y,z) \equiv \Phi\phi_l(x,y,z) \tag{2.35}$$

The condition for laser operation is that the round-trip gain ($G$), averaged over the laser mode must be equal to the total round-trip loss ($L + T$). Equation 2.33 can be rearranged to give an expression for the round trip gain coefficient [3]:

$$G = 2\sigma l_c \iiint\limits_{cavity} \Delta N(x,y,z)\phi(x,y,z)dxdydz = L + T \tag{2.36}$$

The fractional population densities of the upper and lower laser levels can be expressed from equations 2.29 and 2.30 taking into account that for the upper laser level $\partial N_2/\partial x = f_2 \partial N_U/\partial x$ and $f_2 N_L = N_2$ and for the lower laser level $\partial N_1/\partial x = f_1 \partial N_L/\partial x$ and $f_1 N_U = f_1(N_L^0 - N_L) = N_1^0 - N_1$ as the total population density must be a constant. Hence:

$$\begin{aligned}\frac{\partial N_2(x,y,z)}{\partial t} &= f_2\eta_p Rr_p(x,y,z)\\ &- \frac{N_2(x,y,z)}{\tau} - f_2 c_n \sigma[N_2(x,y,z) - N_1(x,y,z)]\Phi\phi_l(x,y,z) = 0\end{aligned} \tag{2.37}$$

$$\begin{aligned}\frac{\partial N_1(x,y,z)}{\partial t} &= -f_1\eta_p Rr_p(x,y,z)\\ &+ \frac{N_1^0(x,y,z) - N_1(x,y,z)}{\tau} + f_1 c_n \sigma[N_2(x,y,z) - N_1(x,y,z)]\Phi\phi_l(x,y,z) = 0\end{aligned} \tag{2.38}$$

The population inversion density $\Delta N$ can be expressed by subtracting these two equations giving:

$$
\begin{aligned}
\frac{\partial \Delta N(x,y,z)}{\partial t} &= (f_1+f_2)\,\eta_p R r_p(x,y,z) \\
&- \frac{\Delta N(x,y,z)-N_1^0}{\tau} - (f_1+f_2)\,c_n\sigma\Delta N(x,y,z)\Phi\phi_l(x,y,z) = 0
\end{aligned} \tag{2.39}
$$

For simplification purposes, a factor $f$ is defined as $f_1 + f_2$. Hence this equation becomes:

$$
\Delta N(x,y,z) = \frac{f\tau\eta_p R r_p(x,y,z) - N_1^0}{1 + f\tau c_n \sigma \Phi \phi_l(x,y,z)} \tag{2.40}
$$

Using this expression in equation 2.36, in conjunction with the expressions for the pump rate $R$ and the total number of laser photons $\Phi$, and defining the output power as $P_{out} = TP_l$, the following equation is obtained:

$$
2\sigma l_c \int_0^l \int_{-\infty}^{\infty} \int_{-\infty}^{\infty} \frac{\frac{\tau f \eta_p}{h\nu_p} P_p r_p(x,y,z) - N_1^0}{1 + \frac{2l_c P_{out}}{T} I_{sat} \phi_l(x,y,z)} \phi_l(x,y,z)\partial x \partial y \partial z = L + T \tag{2.41}
$$

Where the saturation intensity $I_{sat} = (f\sigma\tau)/(h\nu_L)$ [3]. Equation 2.41 is the equation that governs the laser behaviour above threshold. The power required to reach threshold $P_{th}$ can be calculated by stating $P_{out} = 0$ and $P_P = P_{th}$ [15]:

$$
P_{th} = \frac{h\nu_p}{2\sigma l_c f \tau \eta_p}\left(L + T + 2\sigma l_c N_1^0\right)\left[\int_0^l \int_{-\infty}^{\infty} \int_{-\infty}^{\infty} r_p(x,y,z)\phi_l(x,y,z) dx dy dz\right]^{-1} \tag{2.42}
$$

the additional loss suffered by three level lasers due to reabsorption is represented by the $2\sigma l_c N_1^0$ term.

#### 2.4.3.2 Application to waveguide lasers

In the following analysis of laser operation, the terms that describe the pump and laser distributions are expanded. It is assumed that the pump radiation is coupled to the fundamental mode of the cavity. Thus Gaussian distributions can be used to model the behaviour of fundamental pump and laser modes within a waveguide laser. The normalised pump and laser distributions can be expressed as [3]:

$$r_p(x,y,z) = \frac{2\alpha_P}{\pi\omega_{Px}\omega_{Py}(1-e^{-\alpha_p l_c})} e^{(-\frac{2x^2}{\omega_{Px}^2})} e^{(-\frac{2y^2}{\omega_{Py}^2})} e^{-\alpha_P z} \tag{2.43}$$

$$\phi_l(x,y,z) = \frac{2}{\pi\omega_{Lx}\omega_{Ly}l_c} e^{(-\frac{2x^2}{\omega_{Lx}^2})} e^{(-\frac{2y^2}{\omega_{Ly}^2})} \tag{2.44}$$

here $\omega_{Lx}$ and $\omega_{Ly}$ are the laser mode spot sizes in the $x$ and $y$ directions, $\omega_{Px}$ and $\omega_{Py}$ are the pump mode spot sizes in the $x$ and $y$ directions and the subscript $n = P$ or $L$. As the fundamental mode is being considered in this analysis it is possible to define the spot size as the radius for which the intensity falls to $1/e^2$ of its maximum value. The pump is assumed to make a single pass in the medium and $\alpha_p$ is the absorption coefficient. Equation 2.42 can be then be expressed by using the pump and laser distribution expressions and integrating, which produces the following equation:

$$P_{th} = \frac{\pi h\nu_p}{4\sigma f\tau\eta_p}\left(L + T + 2\sigma l_c N_1^0\right)\sqrt{\omega_{Px}^2 + \omega_{Lx}^2}\sqrt{\omega_{Py}^2 + \omega_{Ly}^2} \tag{2.45}$$

The above equation also describes a four-level laser transition [16], in which case the re-absorption loss term can be ignored as the population of the lower laser level is assumed to be zero.

Equation 2.45 illustrates the parameters influencing the laser threshold power. To minimise the threshold power for a given laser transition, the pump and laser spot sizes must be as small as possible which is the case of a high NA channel waveguide geometry. Careful fabrication and the use of low-loss waveguide fabrication techniques is also necessary as the threshold is proportional to the propagation loss. It is less critical for quasi-three-level system lasers where the reabsorption loss is usually dominant but it is fundamental to efficient operation of four-level lasers as the propagation loss is usually predominant. Another possibility to reduce the threshold of a quasi three level laser is cooling [14] but it is a less practical method. It reduces the lower laser level population and hence the reabsorption term.

The laser slope efficiency $\eta_{SE}$ gives an idea of the conversion efficiency of pump power to laser power. Although for a quasi-three-level transition, numerical evaluation is necessary, by using the expressions for $r_p$ and $\phi_l$ at various input and output powers, a definite formula can be expressed for the four-level laser [16]:

$$\eta_{SE} = \frac{\partial P_{out}}{\partial P_p} = \frac{\lambda_l}{\lambda_p}\frac{T}{L+T}\eta_p \eta_{pl} \tag{2.46}$$

Where $\eta_p$ is the pump quantum efficiency, $\eta_{PL}$ is a term which describes the overlap of the pump and laser modes and $\lambda_l/\lambda_p$ gives the quantum defect of the laser transition. It is assumed that the laser operates at low power and that the pump and laser radiations are non-divergent within the waveguide. The overlap of the pump and laser modes can also be expressed as:

$$\eta_{pl} = \frac{\omega_{Lx}\omega_{Ly}\sqrt{2\omega_{Px}^2 + \omega_{Lx}^2}\sqrt{2\omega_{Py}^2 + \omega_{Ly}^2}}{\left(\omega_{Px}^2 + \omega_{Lx}^2\right)\left(\omega_{Py}^2 + \omega_{Ly}^2\right)} \tag{2.47}$$

In a waveguide, the pump and laser modes are confined to the core. As the pump normally has a lower wavelength than the laser, the pump mode within a waveguide is smaller, or nearly equivalent in size to the laser mode, leading to a good overlap that can be calculated from equation 2.47. For $\omega_{Px} \approx \omega_{Lx}$ and $\omega_{Py} \approx \omega_{Ly}$, $\eta_{PL} \approx 0.75$. This illustrates the necessity to reduce the propagation loss with this type of laser device as it is the most influential factor.

An increase of the transmittance of the output coupler will also increase the slope efficiency. However, this also increases the threshold power. Hence it is necessary to use an intermediate output coupler that provides the highest slope efficiency with a reasonable threshold power.

## 2.5 Summary

To understand the behaviour and principle of rare-earth doped waveguide lasers, it is important to understand the basic theory that governs them. The channel waveguide theory is very complex and needs to be solved numerically. The three-layer slab waveguide was introduced in the first section of this chapter as it illustrates the principle of light propagation and can easily be derived. The wave equation was then derived from Maxwell's equation and the solutions calculated for both transverse electric and transverse magnetic modes.

Rare-earth ions were then introduced before the laser theory was derived, concentrating on the rate equation for a quasi-three level system. This model is very useful as it can be applied to all the ions used in this thesis i.e. three and four level ions. An expression was derived for both the threshold power and the slope efficiency. These will be used in chapter 6 to calculate the propagation loss of the laser.

## 2.6 References

[1] D.L. Lee. Electromagnetic Principles of Integrated Optics. *J. Wiley & Sons*, New York, Ch.2, 1986.

[2] T.Y. Fan and R.L. Byer. Modelling and CW Operation of a Quasi-Three-Level 946nm Nd:YAG Laser. *IEEE Journal of Quantum Electronics*, QE-23(5) : p605–612, 1987.

[3] W.P. Risk. Modelling of longitudinally pumped solid state lasers exhibiting reabsorption losses. *Journal of the Optical Society of America B*, 5(7) : p1412–1423, 1988.

[4] A. Tropper. Fibre and waveguide lasers. *Proceedings of the 52nd Scottish Universities Summer School in Physics*, p39–59, 1998.

[5] J.M. Senior. Optical fiber communications, principles and practice, 2nd edition. *Prentice Hall*, New York, 1992.

[6] W.T. Silfvast. Laser fundamentals. *Cambridge University Press*, New York, 1996.

[7] H. Nishihara, M. Haruna and T. Suhara. Optical integrated circuits. *R.R. Donelley & sons*, 1996.

[8] K. Kawano and T. Kitoh. Introduction to optical waveguide analysis. *John Wiley and sons*, 2001.

[9] E.A. Marcatili. Dielectric rectangular waveguide and directional coupler for integrated optics. *Bell systems technology journal*, 48 : p2071–2102, 1969.

[10] D.L. Lee. Electromagnetic Principles of Integrated Optics. *J. Wiley & Sons*, Ch. 5, New York, 1986.

[11] E. Snitzer. Optical maser action of neodymium in a barium crown glass. *Physical Review Letters*, 7(12) : p444–446, 1961.

[12] M.J.F. Digonnet. Rare-earth doped fiber lasers and amplifiers. *Marcel Dekker, Inc.*, 2001.

[13] W. Koechner. Solid-state laser engineering, Chap. 2. *Springer Verlag*, 1999.

[14] T.Y. Fan. Solid State Lasers: New Developments and Applications. *Plenum Press*, New York, 1993.

[15] T. Taira, W.M. Tulloch and R.L. Byer. Modelling of quasi-three-level lasers and operation of cw Yb:YAG lasers. *Applied Optics*, 36(9) : p1867–1874, 1997.

[16] W.A. Clarkson and D.C. Hanna. Effects of transverse-mode profile on slope efficiency and relaxation oscillations in a longitudinally-pumped laser. *Journal of Modern Optics*, 36(4) : p483–498, 1989.

# Chapter 3

# Flame Hydrolysis Deposition

## 3.1 Introduction

Since the first demonstration of laser action [1], a great deal of research has focussed on solid state lasers. Host materials have been extensively studied with lasing being observed in semiconductors, ceramic-based materials [2], crystals [3–6] and glass [7, 8]. Glass is cheap and offers a refractive index similar to that of the existing silica network and thus it is preferred for applications in communications. Such glass lasers consist of a glass matrix doped with active ions. These may be transition metals such as titanium [9, 10] although rare-earth ions are often preferred as they exhibit a number of sharp fluorescence transitions representing almost the whole visible and near infrared portions of the optical spectrum with a high quantum efficiency [11]. Also, rare-earth ions have full 5s and 5p electron shells acting as shield for the 4f electrons which are responsible for the lasing. This shielding allows the absorption and emission characteristics of the ion to be relatively unaffected by doping in different hosts [12]. Another effect of the shielding is to produce relatively narrow emission lines. In the past, crystal hosts have been used for active waveguides and laser fabrication, using various methods such as diffusion [3], pulsed laser deposition [4], contact-bonding [5] and ion implantation [6]. Crystal host lasers often show better thermal conductivity than their glass counterpart and their fluorescence lines are narrower resulting in lower thresholds. Nevertheless, glass is a more frequently used material if high power applications are not involved. Large substrate sizes are available, with a high homogeneity and doping flexibility and a closer index match with fibres [11].

The scope of this thesis is limited to rare-earth doped glass. Thousands of glasses have been fabricated to achieve optical amplification and lasing action including silica, phosphate glasses, halide glasses, chalcogenide glasses and more [13]. The reasons that make silica-on-silicon a favoured technology are described in the following section. Then the fabrication techniques suitable for the production of rare-earth doped glasses are reviewed and our choice of methods justified. If the material is not intrinsically active, rare-earth ions can be incorporated in the matrix by a variety of techniques, as listed in section 3.4. The principles of the FHD technique, which was used throughout the course of this PhD, will be explained, followed by the theory of the sintering of FHD soot. The fabrication system utilised is then presented. Finally, the compositions used during the work presented in this thesis will be detailed.

## 3.2 Silica-on-silicon technology for integrated optics

As a consequence of optical telecommunications development, the need for optical components increases. Optical fibre technology can provide the add-drop filters, amplifiers, and other components needed for optical networks with unsurpassed low loss. However, integrated optics provides the compactness useful for installation of the device in the network, for instance, 1×16 splitters can be made on a single chip instead of using many optical fibre 1×2 splitters cascaded together [14]. Photolithography and UV writing can provide a route towards the fabrication of very complex devices and new devices not possible with fibres [15]. Silicon wafers are very flat, smooth, and available in large sizes and thus provide a very good substrate for the fabrication of high quality thin film layers. Also, silicon can be processed by microelectronic methods, making it possible to integrate electronics and optics if silicon wafers are used as substrates [15]. Silica is a stable material with a refractive index that can be accurately controlled. The optical loss in the third telecom window is much lower in silica than in soft glasses or polymers for instance, and the major part of the existing optical network is made of silica fibres. Thus, silica-on-silicon is very promising as the refractive index is identical to that of fibre, therefore the connection between the two systems is possible with very low loss. Moreover, the silica film is naturally very stable as it is in compression, the thermal expansion coefficient of silicon being greater than that of silica. It also has a high chemical durability.

Silica is a very abundant material existing naturally as crystals such as quartz, cristobalite and tridymite. It is formed by tetrahedra comprising a $Si^{4+}$ ion and four $O^{2-}$ ions. When the crystals are heated to a temperature above 1710°C and cooled rapidly, the crystalline arrangement is broken and the silica tetrahedra are constrained in the form of a glass, which is called ″vitreous silica″. This is the form of silica used in optics [16]. The melting temperature of silica is about 2000°C a value that can be reduced to under 1500°C by the addition of dopants [14]. Physically speaking, the inclusion of dopants in the layers leads to Si-O-Si bonds breaking, creating weak points in the system thence lowering melting temperature. This enables the use of silicon (melting point 1410°C) as the substrate for FHD. The dopants also allow control of the refractive index.

## 3.3 Fabrication techniques suitable for rare-earth doped glass

The following is a non-exhaustive review of fabrication techniques suitable for the fabrication of rare-earth doped silicate glass. Planar waveguide lasers have been obtained in glass with techniques such as MCVD [17] or direct-bonding [18], but in this section only the most widely used fabrication techniques will be mentioned. They are divided into two types: layer alteration and layer deposition. Layer alteration techniques, such as ion implantation and ion exchange, involve the alteration of the upper layer of a substrate. The refractive index difference created is low, resulting in a small Numerical Aperture (NA). In contrast, layer deposition techniques, namely the sol-gel process, sputtering, Plasma-Enhanced Chemical Vapour Deposition (PECVD) and FHD, consist of growing a layer on top of the substrate. Waveguides with bigger thicknesses can be produced and the layer difference in composition means a larger refractive index difference can be obtained as well as higher NA values.

### 3.3.1 Ion implantation

The first report of this technique for waveguide fabrication was published in 1968 [19]. Ion implantation uses ions accelerated to sufficiently high energy ($\sim MeV$) for them to penetrate beyond the surface of a target. The ions are selected by an analyser magnet. By adjusting the magnetic field strength, the magnet only picks the desired species which are then directed onto a substrate. At high energy, the lattice is relatively unaffected. The ions lose their kinetic energy through a series of collisions inducing disorder in the crystal lattice of the target, and come to rest in the target material, a few microns under the surface. The apparatus comprises an ion generator, an accelerator, an ion separator and a deflector. It permits accurate control of the ion distribution but is expensive and cumbersome and thus it is not widely used. Propagation losses in ion implanted waveguides can be as low as 0.15dB/cm [20], although they are often higher [21]. A wide range of ions has been used to fabricate waveguides, including $N^+$, $Be^+$ or $B^+$. This technique has been applied to both rare-earth doped crystals [22] and glass, resulting in lasing action [23].

### 3.3.2 Ion exchange

The principle of ion-exchange is the replacement of mobile ions within a glass substrate by an ion of larger size and/or polarisability to locally modify the refractive index. Typically, the ions come from a molten salt bath [24] or a metal film [25]. The temperature and the duration of the process affect the size of the waveguide produced. Izawa and Nakagome reported the first ion-exchanged waveguides by exchange of $Ti^+$ ions in a silicate glass [26]. Any glass containing monovalent ions can be used as a substrate for ion-exchange [27]. However, the host glass must be carefully chosen to minimise the propagation loss in the resulting waveguide. This technique can be used to fabricate channel devices through masking techniques [28]. The main drawback is that the waveguides produced have a graded refractive index profile with maximum index at the surface of the waveguide [29]. The losses can be as low as 0.1dB/cm [30] and buried structures can be obtained by a secondary heat treatment [31, 32]. To get better control over the exchange speed and the refractive index profile, an electric field can be used in conjunction with thermal ion-exchange. By applying the electric field across the substrate, Field-Assisted Ion-Exchange provides a mean of fabricating step-index profile waveguides [33]. Lasing has been obtained in phosphate [34] and silicate glass [35, 36] among others.

### 3.3.3 Sol-Gel method

In sol-gel-based waveguide fabrication processes, a silicon compound is used, which is hydrolysed, resulting in a homogeneous solution of silica particles in a solvent. This colloid is then coated onto appropriate substrates by dipping or spin coating. The particles coalesce to form a gel and the sample is then baked to evaporate the solvent, leading to a fully dense layer. Cores for optical fibres [37] and planar waveguides [38] have been made using this method. Sol-gel fabrication is, in principle, low cost, easy and versatile [39]. It is difficult to avoid cracking of the layer as it dries [40], however low losses can be achieved, with typical values being

0.2dB/cm at 1.5$\mu m$ [41]. Erbium and neodymium have been introduced in sol-gel layers with indications that lasing in planar waveguides made from these material would be possible [42–44].

### 3.3.4 Sputtering

Fabrication of planar waveguide layers by sputtering involves creating a plasma, usually in argon, by a high voltage discharge in a vacuum chamber. The positive ions of the plasma, having kinetic energies in the range 10eV to 2keV, are directed onto a negatively charged glass target [45]. The composition of the target is similar to that of the layer that is to be deposited. High-energy ions cause these particles, atoms or molecules, to be ejected from the target and the particles settle on a nearby substrate, producing the desired layer. Several different variations on the basic technique exist using different potentials, gas pressures and physical arrangements. RF sputtering is usually preferred to DC sputtering for the deposition of insulators partially to avoid charge build up on the surface of the sample and deposition of insulator on the electrodes. Many active layers have been fabricated, as well as photosensitive films [46], leading to the demonstration of erbium-doped amplifiers [47–49] and neodymium-doped lasers [50]. The advantages of sputtering are that it is a relatively simple technique, which can, in principle, be used with any material [51]. However, the disadvantages are that it can be difficult to achieve very low loss layers, the deposition rate is slow and it is hard to preserve the stoichiometry of the deposited material.

### 3.3.5 PECVD

Plasma Enhanced Chemical Vapour Deposition is one of the most widely used chemical vapour deposition techniques. Chemical vapours are deposited on a substrate by provoking chemical reactions in a deposition chamber at low pressure (0.2-1.0Torr) where an initial, low-temperature reactant gas reacts with other gases to give a solid phase deposit on the substrate surface. In the case of PECVD, a radio frequency discharge creates a low-pressure plasma in an appropriate gas mixture that is used to initiate the reactions. $SiH_4$ and $N_2O$ is the most usual mixture used for PECVD [52]. Doping the layer with phosphorus, germanium or boron controls the refractive index. This is done by adding phosphine ($PH_3$), germane ($GeH_4$) and borane ($BH_3$). The deposition is a three phase process [53]:

- Free radical and ion generation by the plasma. The primary electrons acquire a high energy, some of which they lose by colliding with particles, giving ions and secondary electrons. These will then help the formation of free radicals.
- Radical adsorption and ion incorporation at the film surface. The free radicals are absorbed by the layer.
- Rearrangement of the adsorbed atoms and desorption of reaction by-products from the surface. The atoms are then diffused into stable sites on the surface, and the by-products out-diffused.

PECVD gives layers with good uniformity and the deposition times are realistic, generally of the order of a few hours (the deposition rates are between 2000 and 5000 angstrom per minute). PECVD offers many advantages. For instance, a dopant may be introduced easily and the layers are very high quality and low loss. It also is a one step process operating at relatively low temperature (about 300°C) followed by an annealing stage at a temperature above 600°C [54]. This annealing step is needed, as the layer produced by PECVD is not fully dense [55]. Glasses with volatile components such as phosphorus can be deposited, as it is a low temperature process. Finally, PECVD is an industry proven technique, developed for the microelectronics industry [56]. Rare-earth doped layers can be grown by evaporating the appropriate chelates and adding them to the silane gas flow [57]. Rare-earth doped lasers and amplifiers have been fabricated using a combination of PECVD and Reactive Ion Etching (RIE) [57–59].

### 3.3.6 FHD

The first report of planar films made using Flame Hydrolysis Deposition was published in 1983 [60]. In this technique, the reagents are oxidised in an oxy-hydrogen flame that is directed on the substrate. The reagents are liquid halide materials, which are vaporised in bubblers. The temperature of the halide container (bubbler), and the flow rate of the gas through the bubbler, control the quantity of halide transported to the burner. A carrier gas, usually nitrogen or oxygen, is used to transport the vapour into the flame [61]. The oxidisation of the particles by the flame produces low-density soot that deposits on the substrate. The flame is translated across the substrate to deposit uniform layers of soot. The soot is then consolidated in a furnace to form a transparent fully dense glass layer [62]. By varying the speed of the translation stage and the gas flow rate, the quantity of soot deposited can be modified so that different thicknesses can be obtained for the silica layer. FHD has been shown to produce very low loss films, with results as low as 0.01dB/cm [63]. The layers produced can be very uniform and it is easier to prevent the contamination by particles or the formation of large cluster complexes than in PECVD processes. It is well adapted to solution doping and is an industry proven technique. Numerous groups have demonstrated rare-earth doped FHD produced layers [64–67].

The primary factors in deciding which planar waveguide fabrication technique to use for optical processes are low loss, homogeneity in thickness and refractive index, reproducibility and dopant flexibility. The sol-gel process is not suitable for our devices because of the high risk of contamination. The sputtering technique can lead to layers in which the composition is hard to control and the losses are high. Ion implantation requires costly and complicated equipment and ion exchange requires a rare-earth doped substrate making it less flexible. Based on these arguments, Flame hydrolysis deposition (FHD) was chosen as it seems to offer good quality and low loss layers with a great number of dopants suitable for rare-earth doping.

## 3.4 Review of rare-earth doping techniques

There are two main techniques for doping FHD layers with materials for which there are no suitable volatile inorganic compounds to use in a conventional bubbler. These are solution doping and aerosol doping. Solution doping, which has been developed for fibre manufacture, was first used for rare-earth doping in 1973 by Stone and Burrus [68]. This technique involves doping a soot layer. The deposited soot has to be partially sintered into a robust soot layer [69]. The sample is then immersed in a solution of the chosen precursor. When removed, the sample is dried and consolidated into a solid layer. The final concentration of dopants in the soot depends on the solution concentration, the immersion time and the degree of pre-sintering of the layer [70]. This technique will be described in detail in section 4.2. Aerosol doping involves doping the layer during fabrication [71]. It was patented in 1982 [72, 73] and is a one step process. Solutions of the dopants are atomised in a gas flow that carries the droplets to the flame in which the water evaporates, leaving a particle containing the dopant [74]. Oxidation of the dopant takes place, and it is subsequently deposited into the layer [75]. The main advantage of this technique is its simplicity. The process does not involve much handling of the soot, resulting in a lower contamination of the resulting layer. However, the drawback is that it is not a proven technique and it may prove difficult to control in terms of dopant uniformity and concentration.

## 3.5 FHD principles

The idea of flame hydrolysis deposition was patented in 1942 by J.F. Hyde [76], and was first used in a planar geometry by Kawachi et al. in 1983 [60]. Nowadays, FHD is a common technique used to make doped silica glass by depositing a soot layer using the oxidation of halides in an oxy-hydrogen flame, followed by a consolidation treatment. The reagents are vapourised in halide containers called bubblers. A carrier gas, usually nitrogen or oxygen, is used to transport the vapour into the flame and the temperature of the bubbler and flow rate of the carrier gas control the quantity of halide transported to the burner. The reactants are injected into the centre of an oxy-hydrogen flame which is a highly reactive environment where endothermic breakdown of reagents and exothermic recombination of radicals take place, forming reaction products. An oxygen-hydrogen flame can be characterised by the endothermic reactions:

$$O + H_2 \rightleftharpoons OH + H \tag{3.1}$$

$$H + O_2 \rightleftharpoons OH + O \tag{3.2}$$

and the propagation step:

$$OH + H_2 \rightleftharpoons H_2O + H \tag{3.3}$$

leading to a build up of an excess population of free atoms and radicals in the reaction zone [77].

An operating temperature of approximately 2000℃ (at the centre of the flame) causes oxidation to occur. Direct oxidation is the principal reaction occurring. Particles of silica are formed by this reaction:

$$SiCl_4 + O_2 \rightleftharpoons SiO_2 + 2Cl_2 \tag{3.4}$$

The $Cl_2$ formed reacts with water to give HCl. For temperatures under 1200C, the principal reaction is hydrolysis:

$$SiCl_4 + 2H_2O \rightleftharpoons SiO_2 + 4HCl \tag{3.5}$$

$$2POCl_3 + 3H_2O \rightleftharpoons P_2O_5 + 6HCl \tag{3.6}$$

$$4BCl_3 + 6H_2O \rightleftharpoons 2B_2O_3 + 12HCl \tag{3.7}$$

The particles of $SiO_2$, $B_2O_3$ and $P_2O_5$ are formed within the flame, while $GeO_2$ can both be formed within the flame and condense on the substrate [62]. The oxide vapour concentration gradient within the flame dictates the maximum size that single particles can achieve. The deposited particle size depends on the dwell time of halides in the flame and the distance between flame and substrate. This is because once the particles are formed, they tend to aggregate and coagulate before reaching the substrate. The temperature of the substrate itself affects the rate of deposition by changing the temperature gradient near the substrate surface.

The particle growth mechanisms that take place in the particle stream between particle creation and soot deposition can be summarised in the following manner:

- Condensation of a specific oxide via nucleation from the saturated vapour phase
- Growth of a single particle within the vapour rich region of the flame
- Aggregation and coalescence of particles in the flame
- Coagulation of solid particles within the flame-substrate distance

The temperature of the substrate can also affect the relative amount of dopants deposited in a crystalline phase. This is not too critical as the crystalline phase tends to disappear during consolidation. Nevertheless, it can lead to compositional inhomogeneities when compared to layers that are amorphous at all stages.

The flame is translated across the substrate to deposit uniform layers of the agglomeration of particles widely called soot. By varying the speed of the translation stage and the number of scans over the substrate, the quantity of soot deposited can be modified, so that different thicknesses can be obtained for the silica layer. The deposited soot is then consolidated into a full density amorphous solid.

## 3.6 Principle of sintering

The mechanism responsible for consolidating FHD soot into a fully densified glass layer is called viscous sintering [78]. Sintering occurs when powders, in this case FHD silica soot, are heated to near their melting point. Particles are assumed to be spherical and heating induces a certain degree of particle softening, resulting in the growth of a neck between adjacent particles (Fig. 3.1). This is followed by the reduction of the centre-to-centre separation of two adjacent particles [79]. Both effects are attributed to surface tension. Such necking results in a gradual closure of the open struc-

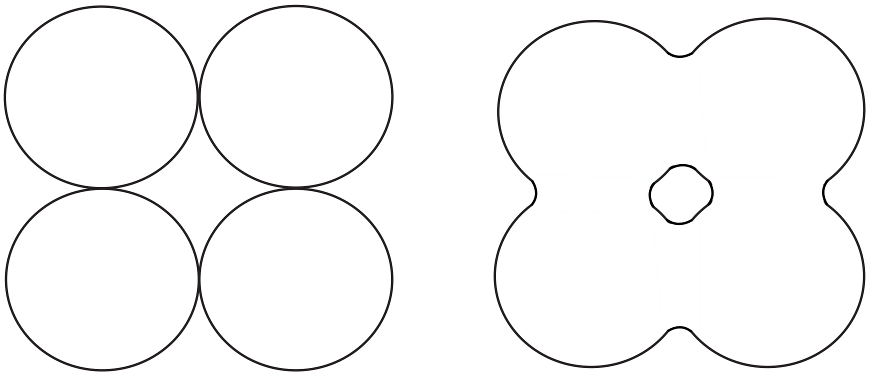

Figure 3.1: Necking of particles during sintering

ture between spheres and the formation of pores which are also spherical due to macroscopic viscous flow and surface tension effects. The soot produced by FHD has a very open structure made of silica particles joined together, forming a network of randomly connected bridges [61]. In the very first stages of the sintering, the necking begins and the inter-particle distance decreases until the pores are closed. At this point, the effect of surface tension produces a capillary pressure that is responsible for the closure of the pores.

At the beginning of the sintering process, a solid solution of the silica matrix and the dopants is formed. The densification of the soot as a glass phase requires having a sufficient volume of the amorphous material at a viscosity that allows particles to coalesce and pore closure to happen without crystallisation taking place [62]. The melting point of the dopants is lower than that of silica which lowers the viscosity of the system and leads to a fully dense glass layer at lower temperatures than would normally be needed. This consolidation is complete after one hour at about 1000-1400°C depending on the composition. The sample is inserted into a furnace that has reached the consolidation temperature, ensuring that the samples are ramped from room temperature to consolidation temperature at the maximum rate. The samples are removed from the furnace directly to room temperature giving a very rapid cooling rate to avoid crystallization.

## 3.7 Description of the FHD system

The FHD system used to create the samples described throughout this thesis comprises three parts: the gas supply system, the burner system and the boron supply system. For more information on the FHD system, readers are directed to Sam Watts's thesis [40].

### 3.7.1 Gas supply system

The gas supply system is placed in a glove box for safety reasons. It comprises three bubblers in which the reactant vapour is actually produced. These are cylindrical borosilicate containers, each holding a different precursor. The carrier gas (dry oxygen) is inserted into the liquid at the bottom of the bubbler via the pressure in the line. It produces bubbles in the liquid reactant, producing saturated vapour in the free volume above the liquid which is transported by the carrier gas all the way to the burner. The liquid level within the bubbler has to be maintained for all the depositions to have a comparable amount of dopants in the vapour and thus in the layer. Each bubbler is placed in a silicone oil bath with a water cooling system and also has an independent heating system and temperature controller to achieve optimum vapour pressure. For typical photosensitive samples, the precursors used are silicon tetrachloride ($SiCl_4$), phosphorous oxychloride ($POCl_5$), and germanium tetrachloride ($GeCl_4$), the germanium dopants making the layer photosensitive. Three mass flow controllers (MFC) monitor the flow rate of each individual gas supply which are then mixed together. Dry oxygen is used to dilute this supply stream before it gets into the burner. The MFC, control valves and temperature controllers are interfaced to a computer and a program has been written to control all these devices, record the data for each deposition and display the information needed for real time monitoring of the deposition. This program allows the user to define a layer recipe, and then the program monitors the deposition and sets it to the purge mode when the deposition is finished.

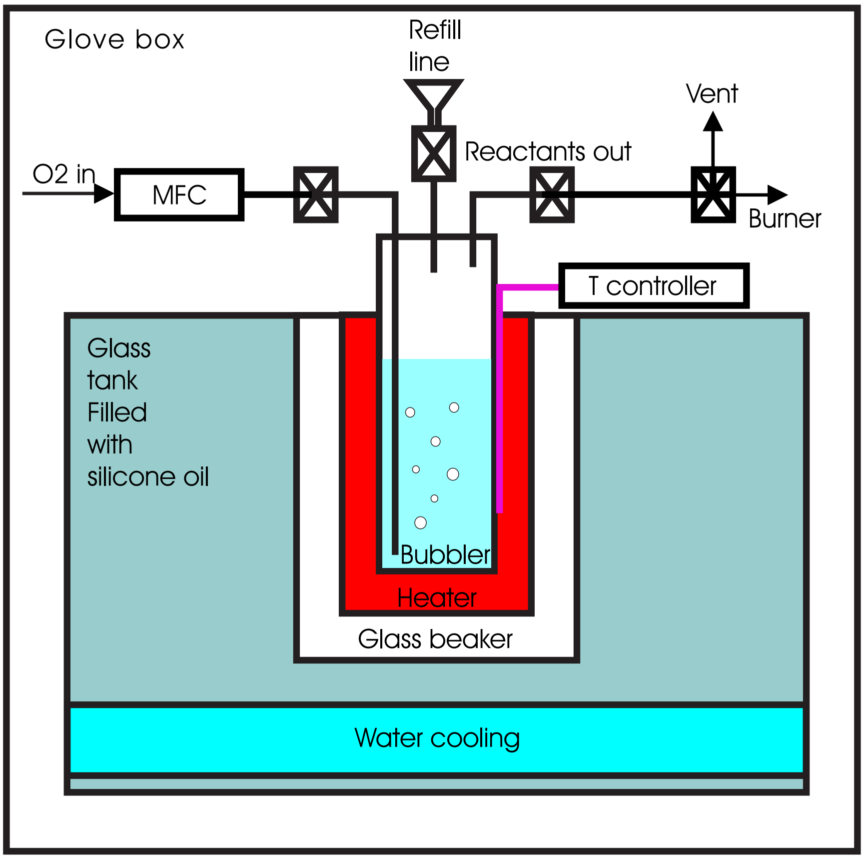

Figure 3.2: Gas supply system

### 3.7.2 Burner system

The burner consists of six rings and is made of stainless steel. The central ring is used to supply the reactants into the flame by means of a carrier gas while the other rings supply the burner gases. The reagent and carrier gases can be directed towards the first ring of the burner or the extract to allow the flame to stabilize before flowing the reactants into the reaction area. Nitrogen purging occurs through this central ring when the reactants are not flowing to avoid moisture entering the FHD system and causing a reaction inside the burner. The hydrogen fuel is supplied through ring 5 while ring 3 supplies the oxygen required for combustion. Three rings flow nitrogen, used to separate the reactive gases from each other while in close proximity of the burner nozzle. The nitrogen flowing through ring 2 stops the formation of soot in the burner by pushing the reaction zone higher up in the flame. The shield produced by ring 4 helps to keep the burner cool by separating it from the flame. The flow rate introduced through ring 6 minimizes the recirculation of particles back into the flame. This prevents the particles from passing more than once through the flame, which keeps the particles smaller.

The flame gases are supplied by a dedicated supply system. It comprises flash back arresters for the oxygen and hydrogen lines. This is used to stop a potential flame burn-back for the hydrogen line or the flame being forced back into the oxygen line. These two lines are also fitted with solenoid actuated valves that are controlled using a key switch and an emergency stop button. This makes the system safe in case of power failure and permits a quick extinction of the flame if necessary. Each line is also fitted with an MFC that regulates the flow of the gas supplied. The fluctuations of flow rate are of about $0.01 l/min$ on a short time scale which is in agreement with the precision of the MFC (0.7% of flow rate).

During sample preparation, the substrate is placed upside down above the flame and held in place by a vacuum pump. This design keeps the flame as symmetric as possible to ensure a greater homogeneity of the deposition across the substrate. Secondly, it reduces the possible contamination of the layer as atmospheric dust and soot waste cannot fall on the soot layer, improving the cleanliness of the resulting glass layers. The substrate is heated to temperatures between 200 and 600°C to protect the soot by avoiding the inclusion of liquid water. As the temperature of the substrate affects the deposition rate of the soot, the uniformity has to be as good as possible. This has been achieved by radiative heating delivered by a set of halogen lamps. For practical reasons, all the layers deposited for the work related in this thesis have been deposited on samples at about 240°C. This is mainly because most of the deposition characteristics were known from previous experiments for the compositions used [40]. In order to keep a maximum of conditions identical, so that all alterations are due to the solution doping itself, the same temperature was used.

Waste gases and soot are removed from the system by an extract applied between two concentric rings of borosilicate spaced by approximately 10 mm. The inner tube is also about 10mm shorter than the outer one, permitting it to mainly extract the gases present within the area of the burner. Computer controlled translation stages move the burner and the extract system, by means of stepper motors, across the sample, to ensure homogeneity of the layer thickness over the sample. The two translation stages are mounted perpendicularly, one to the other, and fastened to the FHD rig. A sliding seal, made of piled aluminium sheets, minimises the amount of corrosive gas products of the deposition going into the FHD rig, increasing the longevity of the rig components and improve the operating safety. It also protects the FHD from soot or hot substrates falling into the rig in case of failure of the vacuum pump holding the samples in place. At the end of the deposition, the samples are removed from the deposition chamber and the soot is consolidated in a resistance furnace (Elite). When closed, this furnace has a thermal uniformity better than 1°C but problems of temperature stability can arise when the furnace is opened to insert a sample. Here, the temperature can drop by 20-30°C. It then overshoots by less than 2°C within 30 seconds and reverts back to the set temperature within 5 minutes. This can cause problems when consolidating layers with an acute dependence on the consolidation temperature.

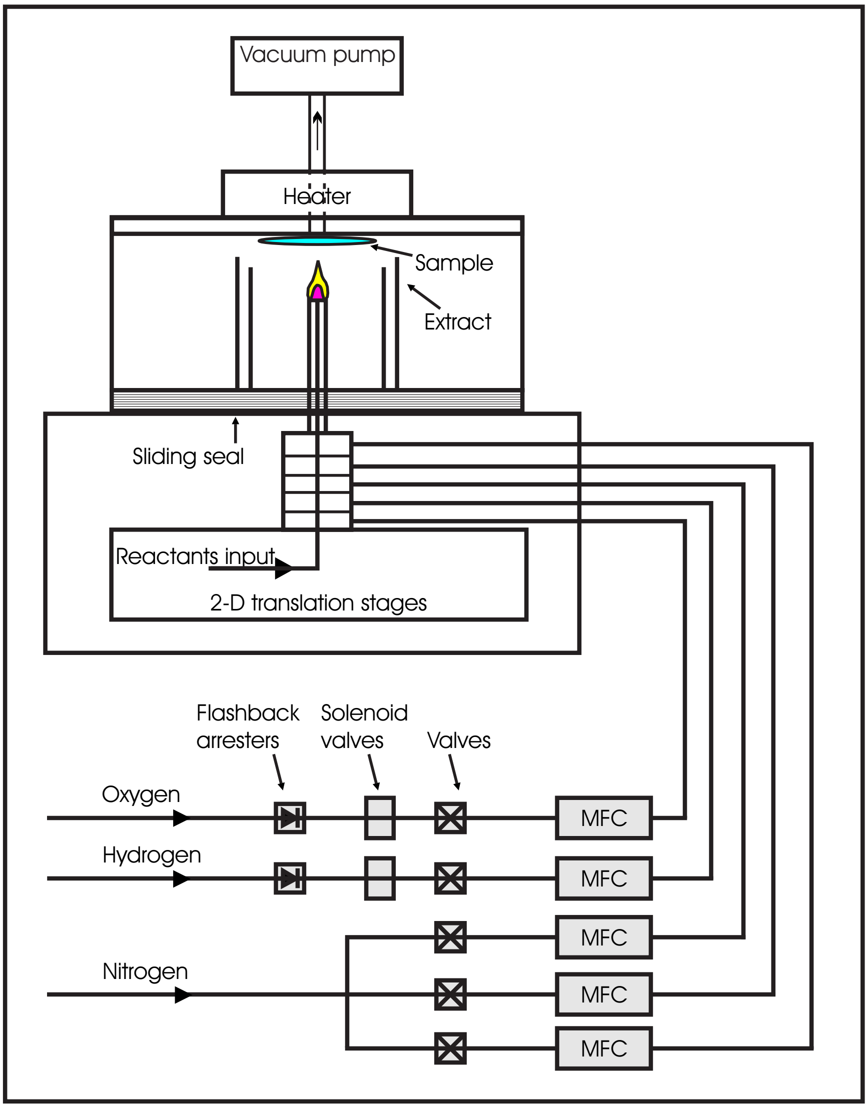

Figure 3.3: Deposition system

### 3.7.3 $BCl_3$ system

Doping layers with boron is important for the control of refractive index and consolidation temperature of a planar waveguide layer. Incorporating boron decreases the refractive index of a layer with increasing doping level. This can be used to compensate for the increase in refractive index due to the germanium doping that is required for UV writing of channel waveguides (see section 5.3). This compensation is required in order to have three layers of equal refractive index prior to UV writing. The slab waveguide should be avoided so the mode propagation would only happen in the UV defined core region and the mode profile would have a symmetrical profile matching the mode profile in fibres. This would improve the coupling efficiency into fibres. The birefringence and polarisation dependent losses due to the refractive index difference between layers would then be reduced. We have included boron tri-chloride ($BCl_3$) in our choice of dopants to replace boron tri-bromide ($BBr_3$). Boron and phosphorus co-doping is not possible with $BBr_3$ and $P_2O_5$ as they react together. The doping of silica with this three-dopant system induces lower temperature consolidation.

As the three layers need to have compatible consolidation temperatures, co-doping is used to grow one lightly phosphorus and boron doped layer, then a germanium, boron and phosphorus doped layer, then a phosphorus and boron doped layer with a higher concentration of dopants in order to have a lower consolidation temperature, however resulting in the same refractive index. This limits the contamination of an existing layer by the newly grown one. Another reason to prefer $BCl_3$ is that $BBr_3$ requires nitrogen as the carrier gas, hence depending on the amount of $BBr_3$ needed the nitrogen flow has to change. For all our others dopants, oxygen can be used as the carrier gas. The high vapour pressure of $BCl_3$ at ambient temperature allows it to be treated as a gas, which means an independent carrier gas is not needed. This means that the flame condition will be more similar between depositions when using $BCl_3$ instead of $BBr_3$. The $BCl_3$ flows from a cylinder into the pipe work through a series of valves, then via an MFC that regulates its flow rate. It then goes to the burner through two solenoid valves. These valves allow the system to be purged by dry nitrogen when $BCl_3$ is not required, and direct the $BCl_3$ to the extract in the event of failure of the system.

## 3.8 FHD layers

### 3.8.1 Current capabilities and aims

With this system, three layer samples have been fabricated. Many different compositions have been investigated. Initially, these were layers with only two dopants, such as germanium and boron doped silica on phosphorus doped silica, or germanium and boron doped silica on boron doped silica. Later, layers using the three dopants have been realised. These germanium-boron-phosphorus doped silica layers allowed us to decrease the consolidation temperature from 1400°C to anywhere between 1000 to 1400°C depending on the composition. This is important as silicon wafers melt at 1410°C. Single layers of 5 to 15$\mu m$ thickness can be fabricated, with a thickness variation across a 50mm square sample of 200 to 500nm, and a roughness of 50 to 70nm measured using a profilometer. The refractive index of the layer can be accurately controlled by changing the dopant concentration such that any value between 1.46 and 1.49 can be achieved. A standard 3-layer set of compositions for underclad, core and overclad layers has been developed and an index matched set of compositions with germanium-free cladding is still being investigated to this day.

### 3.8.2 Layers used

For the solution doping experiments, three different types of layers have been created, mainly because of the addition of $BCl_3$ into our deposition equipment. Some experiments were conducted using a germanium and boron doped soot before the $BCl_3$ system was installed. The vapour contained 10 atomic% $BBr_3$ and 30 atomic % $GeCl_4$. The appropriate consolidation treatment for that soot was three hours at 1400°C. Another soot was tried later using the three-dopant system of phosphorus-boron-germanium doped soot. The proportions were 10at% for $POCl_5$, 12at% for $BCl_3$ and 20at% for $GeCl_4$ and the consolidation treatment was found to be 1 hour at 1075°C. In the mean time, a standard composition for a three-layer system was developed by Sam Watts [40]. The underclad layer consists of a 16 micron thick layer of phosphorus-boron-germanium doped silica glass. The vapour stream contains 14at% $POCl_5$, 3at% for $BCl_3$ and 2at% $GeCl_4$ and the layer has a refractive index of 1.4641 as measured by prism coupling at 633nm. The core layer is a 6 micron thick layer with dopant proportions of 20at% for $POCl_5$, 10at% for $BCl_3$ and 5at% for $GeCl_4$. This corresponds to doping levels of respectively 12.28wt%, 1.11wt% and 4.08wt% as measured by secondary ion mass spectroscopy (SIMS) with a refractive index of 1.4818 at 633nm. The vapour stream for the overclad layer contains 13at% $POCl_5$, 8at% $BCl_3$ and 2at% $GeCl_4$. The layer formed is 10 microns thick and has a refractive index of 1.4641. This set of compositions has been used for the more recent work on rare-earth doping of layers (see chapter 4). The layers had optimum consolidation at 1350°C, 1250°C and 1200°C respectively. It can be noted that the structure is not index matched anymore due to the increase in refractive index caused by the introduction of the rare-earth ions in the core. The experiments were performed with this structure anyway with the idea that a better matched composition set could be developed in later experiments.

## 3.9 Summary

In this chapter, the advantages of silica-on-silicon technology have been reviewed. The fabrication techniques that can be used for the production of rare-earth doped glass have been listed and then the techniques available for the rare-earth doping of silica have been described and compared. Following this, the principles of the FHD system have been explained and the in-house system used for the fabrication of devices described in this work was introduced. Finally, the compositions used have been detailed.

## 3.10 References

[1] T. Maiman. Stimulated optical radiation in ruby. *Nature*, 187 : p493–494, 1960.

[2] J.H. Lu, J.R. Lu, T. Murai, K. Takaichi, T. Uematsu, J.Q. Xu, K. Ueda, H. Yagi, T. Yanagitani and A.A. Kaminskii. 36-W diode-pumped continuous-wave 1319-nm Nd:YAG ceramic laser. *Optics Letters*, 27(13) : p1120–1122, 2002.

[3] S.J. Hettrick, J.S. Wilkinson and D.P. Shepherd. Neodymium and gadolinium diffusion in yttrium vanadate. *Journal of the Optical Society of America B*, 19(1) : p33–36, 2002.

[4] C.L. Bonner, A.A. Anderson, R.W. Eason, D.P. Shepherd, D.S. Gill, C. Grivas and N.A. Vainos. Performance of a low-loss pulsed-laser-deposited Nd:$Gd_3Ga_5O_{12}$ waveguide laser at 1.06 and 0.94$\mu m$. *Optics Letters*, 22(13) : p988–990, 1997.

[5] D.P. Shepherd, C.L. Bonner, C.T.A. Brown, W.A. Clarkson, A.C. Tropper, D.C. Hanna and H.E. Meissner. High-numerical-aperture, contact-bonded, planar waveguides for diode-bar-pumped lasers. *Optics Communications*, 160 : p47–50, 1999.

[6] F. Chen, H. Hu, J.H. Zhang, K.M. Wang, Z.X. Cheng, Q.M. Lu and D.Y. Shen. Planar optical waveguide formation in erbium-doped $NaY(WO_4)_2$. *Materials letters*, 51 : p543–546, 2001.

[7] Y. Hibino, T. Kitagawa, M. Shimizu, F. Hanawa and A. Sugita. Neodymium-doped silica optical waveguide laser on silicon substrate. *IEEE Photonics Technology Letters*, 1(11) : p349–350, 1989.

[8] A.K. Mairaj, A.M. Chardon, D.P. Shepherd and D.W. Hewak. Laser performance and spectroscopic analysis of optically written channel waveguides in neodymium-doped gallium lanthanum sulphide glass. *IEEE Journal of Selected Topics in Quantum Electronics*, 8(6) : p1381–1387, 2002.

[9] A.A. Anderson, R.W. Eason, L.M.B. Hickey, M. Jelinek, C. Grivas, D.S. Gill and N.A. Vainos. A Ti:sapphire planar waveguide laser grown by pulsed laser deposition. *Optics Letters*, 22(20) : p1556–1158, 1997.

[10] L.M.B. Hickey and J.S. Wilkinson. Titanium diffused waveguides in sapphire. *Electronics Letters*, 32(34) : p2238–2239, 1996.

[11] W. Koechner. Solid-state laser engineering, Chap. 2. *Springer Verlag*, 1999.

[12] M.J.F. Digonnet. Rare-earth doped fiber lasers and amplifiers. *Marcel Dekker, Inc.*, 2001.

[13] D.W. Hewak. Glass and rare-earth doped glasses for optical fibres. *Short Run press Ltd*, 1998.

[14] M. Yamane and Y. Asahara. Glasses for photonics. *Cambridge university press*, 1999.

[15] Y.P. Li and C.H. Henry. Silica-based optical integrated circuits. *IEE proceedings-optoelectronics*, 143(5) : p263–280, 1996.

[16] W.E. Worral. Clays and ceramic raw materials. *Applied science publishers Ltd*, 1975.

[17] B. Wu and P.L. Chu. Fabrication of high concentration rare-earth-doped silica-based waveguide by MCVD method. *IEEE Photonics Technology Letters*, 7(6) : p655–657, 1995.

[18] C.B. Gawith, A. Fu, T. Bhutta, P. Hua, D.P. Shepherd, E.R. Taylor, P.G.R. Smith, D. Milanese and M. Ferraris. Direct-UV-written buried channel waveguide lasers in direct-bonded intersubstrate ion-exchanged Nd:SGBN glass. *Applied Physics Letters*, 81(19) : p3522–3524, 2002.

[19] E.R. Schineller, R.P. Flam and D.W. Wilmot. Optical waveguides formed by proton irradiation of fused silica. *Journal of the Optical Society of America*, 58(9) : p1171–1176, 1968.

[20] C.M. Johnson, M.C. Ridgway and P.W. Leech. Thermal annealing of implantation-induced compaction for improved silica waveguide performance. *Applied Physics Letters*, 69() : p984–986, 1996.

[21] D.L. Lee. Electromagnetic principles of integrated optics. *John Wiley and sons*, 1986.

[22] P.J. Chandler, S.J. Field, D.C. Hanna, D.P. Shepherd, P.D. Townsend, A.C. Tropper and L. Zhang. Ion-implanted Nd:YAG planar waveguide laser. *Electronics Letters*, 25(15) : p985–986, 1989.

[23] D.P. Shepherd, D.J.B. Brinck, J. Wang, A.C. Tropper, D.C. Hanna, G. Kakarantzas and P.D. Townsend. 1.9$\mu m$ operation of a Tm:lead germanate glass waveguide laser. *Optics Letters*, 19(13) : p954–956, 1994.

[24] T.G. Giallorenzi, E.J. West, R. Kirk, R. Ginther and R.A. Andrews. Optical waveguides formed by thermal migration of ions in glass. *Applied Optics*, 12(6) : p1240–1245, 1973.

[25] S.S. Gevorgyan. Single-step buried waveguides in glass by field-assisted copper ion-exchange. *Electronics Letters*, 26(1) : p38–39, 1990.

[26] T. Izawa and H. Nakagome. Optical waveguide formed by electrically induced migration of ions in glass plates. *Applied Physics Letters*, 21(12) : p584–586, 1972.

[27] E.K. Mwarania. Planar ion-exchanged waveguide lasers in glass. *PhD thesis, University of Southampton*, 1992.

[28] S.J. Hettrick, J.I. Mackenzie, R.D. Harris, J.S. Wilkinson, A.C. Tropper and D.P. Shepherd. Ion-exchanged tapered waveguide laser in neodymium-doped BK7 glass. *Optics Letters*, 25(19) : p1433–1435, 2000.

[29] A. Opilski, R. Rogozinski, M. Blahut, P. Karasinski, K. Gut and Z. Opilski. Technology of ion exchange in glass and its application in waveguide planar sensors. *Optical Engineering*, 36(6) : p1625–1638, 1997.

[30] N.V. Nikonorov and G.T. Petrovskii. Ion-exchanged glasses in Integrated Optics: the current state of research and prospects (a review). *Glass physics and chemistry*, 25(1) : p16–55, 1999.

[31] R.V. Ramaswamy and S.I. Najafi. Planar, buried, ion-exchanged glass waveguides: diffusion characteristics. *IEEE Journal of Quantum Electronics*, QE-22(6) : p883–891, 1986.

[32] P.C. Noutsios and G.L. Yip. Shallow buried waveguides made by purely thermal migration of $K^+$ ions in glass. *Optics Letters*, 15(4) : p212–214, 1990.

[33] P.C. Noutsios and G.L. Yip. Characterization and modeling of planar surface and buried waveguides made by field-assisted $K^+$ ion exchange. *Applied Optics*, 31(25) : p5283–5291, 1992.

[34] K.J. Malone, N.A. Sandford and J.S. Hayden. Integrated optic laser emitting at 906, 1057 and 1358nm. *Electronics Letters*, 29(8) : p691–693, 1993.

[35] E.K. Mwarania, J. Wang, J. Lane and J.S. Wilkinson. Neodymium-doped ion-exchanged waveguide lasers in BK-7 glass. *Journal of Lightwave Technology*, 11(10) : p1550–1558, 1993.

[36] C. Florea and K.A. Winick. Ytterbium-doped glass waveguide laser fabricated by ion exchange. *Journal of Lightwave Technology*, 17(9) : p1593–1601, 1999.

[37] K. Susa, I. Matsuyama, S. Satoh and T. Suganuma. New optical fibre fabrication method. *Electronics Letters*, 18(12) : p499–450, 1982.

[38] M. Usui, S. Imamura, S. Sugawara, S. Hayashida, H. Sato, M. Hikita and T. Izawa. Low-loss polymeric optical waveguides with high thermal stability. *Electronics Letters*, 30(12) : p958–959, 1994.

[39] B.L. Booth. Low loss channel waveguides in polymers. *Journal of Lightwave Technology*, 7(10) : p1445–1453, 1989.

[40] S.P. Watts. Flame Hydrolysis Deposition of photosensitive silicate layers suitable for the definition of waveguiding structure through direct ultraviolet writing. *PhD thesis, University of Southampton*, 2002.

[41] G. Fishbeck, R. Moosburger, C. Kostrzewa, A. Achen and K. Peterman. Singlemode optical waveguides using a high temperature stable polymer with low losses in the 1.55$\mu m$ range. *Electronics Letters*, 33(6) : p518–519, 1997.

[42] C. Strohhofer, S. Capecchi, J. Fick, A. Martucci, G. Brusatin and M. Guglielmi. Active optical properties of erbium-doped $GeO_2$-based sol-gel planar waveguides. *Thin Solid Films*, 326 : p99–105, 1998.

[43] Q. Xiang, Y. Zhou, B.S. Ooi, Y.L. Lam, Y.C. Chan and C.H. Kam. Optical properties of $Er^{3+}$-doped $SiO_2$-$GeO_2$-$Al_2O_3$ planar waveguide fabricated by sol-gel processes. *Thin Solid Films*, 370 : p243–247, 2000.

[44] S.S. Wang, Y. Zhou, Y.L. Lam, C.H. Kam, Y.C. Chan and X. Yao. Fabrication and characterisation of neodymium-doped silica glass by sol-gel process. *Material Research Innovation*, 1 : p92–96, 1997.

[45] H. Nishihara, M. Haruna and T. Suhara. Optical integrated circuits. *Fischer and Smith Series Editor*, 1989.

[46] J. Nishii, H. Yamanaka, H. Hosono and H. Kawazoe. Preparation of Bragg gratings in sputter-deposited $GeO_2$-$SiO_2$ glasses by excimer-laser irradiation. *Optics Letters*, 21(17) : p1360–1362, 1996.

[47] G. Nykolak, M. Haner, P.C. Becker, J. Shmulovich and Y.H. Wong. Systems evaluation of an $Er^{3+}$-doped planar waveguide amplifier. *IEEE Photonics Technology Letters*, 5(10) : p1185–1187, 1993.

[48] R.N. Ghosh, J. Shmulovich, C.F. Kane, M.R.X. de Barros, G. Nykolak, A.J. Bruce and P.C.Becker. 8-mW threshold $Er^{3+}$-doped planar waveguide amplifier. *IEEE Photonics Technology Letters*, 8(4) : p518–520, 1996.

[49] W. Huang and R.A. Syms. Analysis of folded erbium-doped planar waveguide amplifiers by the method of lines. *Journal of Lightwave Technology*, 17(12) : p2658–2664, 1999.

[50] G.R.J. Robertson and P.E. Jessop. Optical waveguide laser using an rf sputtered Nd:glass film. *Applied Optics*, 30(3) : p276–278, 1991.

[51] R.G. Hunsperger. Integrated optics: theory and technology. *Springer-Verlag*, 1985.

[52] A. Sherman. Chemical Vapor Deposition for Microelectronics: Principles, Technology, and Applications. *Noyes publications*, 1987.

[53] K.E. Mattson. Silica-on-silicon fabrication technology for telecommunication. *PhD thesis, Technical University of Denmark* , 1984.

[54] S.C. Deshmukh and E.S. Aydil. Low-temperature plasma enhanced chemical vapor deposition of $SiO_2$. *Applied Physics Letters*, 65(25) : p3185–3187, 1994.

[55] M.V. Bazylenko, M. Gross and D. Moss. Mechanisms of photosensitivity in germanosilica films. *Journal of Applied Physics*, 81(11) : p7497–7505, 1997.

[56] J. Canning, D.J. Moss, M. Faith, P. Leech, P. Kemeny, C.V. Poulsen and O. Leistiko. Ultrastrong UV written gratings in PECVD grown germanosilicate rib waveguides. *Electronics Letters*, 32(16) : p1479–1480, 1996.

[57] J. Hubner, S. Guldberg-Kjaer, M. Dyngaard, Y. Shen, C.L. Thomsen, S. Balslev, C. Jensen, D. Zauner and T. Feuchter. Planar Er- and Yb-doped amplifiers and lasers. *Applied Physics B: Lasers and Optics*, B 73 : p435–438, 2001.

[58] K. Shuto, K. Hattori, T. Kitagawa, Y. Ohmori and M. Horiguchi. Erbium-doped phosphosilicate glass waveguide amplifier fabricated by PECVD. *Electronics Letters*, 29(2) : p139–141, 1993.

[59] S. Guldberg-Kjaer, J. Hubner, M. Kristensen, C. Laurent-Lund, M. Rysholt Poulsen and M.W. Sckerl. Planar waveguide laser in Er/Al-doped germanosilicate. *Electronics Letters*, 35(4) : p302–303, 1999.

[60] M. Kawachi, M. Yasu and T. Edahiro. Fabrication of $SiO_2$-$TiO_2$ glass planar optical waveguides by flame hydrolysis deposition. *Electronics Letters*, 19(15) : p583–584, 1983.

[61] G.D. Maxwell. Optical waveguide fabrication in silica using flame hydrolysis. *PhD Thesis, University of Glasgow*, 1990.

[62] S. Sakaguchi. Consolidation of GeO2 soot body prepared by flame hydrolysis reaction. *Journal of Non-crystalline Solids*, 171(3) : p228–235, 1994.

[63] M. Kawachi. Silica waveguides on silicon and their application to integrated-optic components. *Optical and Quantum Electronics*, 22 : p391–416, 1990.

[64] K. Hattori, T. Kitagawa, M. Oguma, Y. Ohmori and M. Horiguchi. Erbium-doped silica-based waveguide amplifier integrated with a 980/1530nm WDM coupler. *Electronics Letters*, 30(11) : p856–857, 1994.

[65] J.R. Bonar, M.V.D. Vermelho, A.J. McLaughlin, P.V.S. Marques, J.S. Aitchison, J.F. Martins-filho, A.G. Bezerra-Jr, A.S.L. Gomes and Cid.B. de Araujo. Blue light emission in thulium doped silica-on-silicon waveguides. *Optics Communications*, 141 : p137–140, 1997.

[66] T. Kitagawa, K. Hattori, M. Shimizu, Y. Ohmori and M. Kobayashi. Guided-wave laser based on erbium-doped silica planar lightwave circuit. *Electronics Letters*, 27(4) : p334–335, 1991.

[67] R. Tumminelli, F. Hakimi and J. Haavisto. Integrated-optic Nd:glass laser fabricated by flame hydrolysis deposition using chelates. *Optics Letters*, 16(14) : p1098–1100, 1991.

[68] J. Stone and C.A. Burrus. Neodymium-doped silica lasers in end-pumped fiber geometry. *Applied Physics Letters*, 23(7) : p388–389, 1973.

[69] J.A. Bebbington, G. Barbarossa, J.R. Bonar and J.S. Aitchinson. Rare-earth doped silica waveguides on Si fabricated by flame hydrolysis deposition. *Applied Physics Letters*, 62(4) : p337–339, 1993.

[70] J.E. Townsend, S.B. Poole and D.N. Payne. Solution-doping technique for fabrication of rare-earth doped optical fibres. *Electronics Letters*, 23(7) : p329–331, 1987.

[71] P. Marques, A.P. Leite and A.P. Aitchinson. Bragg gratings in two layer core planar silica waveguides and its application to integrated lasers. *POWAG*, 2000.

[72] S. Takahashi, K. Sanada and O. Fakuda. *US Patent 4336049*, 22 June 1982.

[73] S. Takahashi, K. Sanada and O. Fakuda. *US Patent 4388098*, 14 June 1983.

[74] T.F. Morse, A. Kilian and L. Reinhard. Aerosol techniques for glass formation. *Journal of Non-crystalline Solids*, 129 : p93–100, 1991.

[75] J.R. Bonar. Waveguide lasers in rare-earth doped planar silica. *PhD Thesis, University of Glasgow*, 1995.

[76] J.F. Hyde. *US Patent 2272342*, 10 fevrier 1942.

[77] A.G. Gaydon and H.G. Wolfhard. Flames. *Chapman and Hall Ltd*, 1970, ISBN 0-412-09330-8.

[78] M.B. Waldron and B.L. Daniell. Sintering. *Heydon and sons Ltd*, 1978, ISBN 0-85501-178-5.

[79] G.W. Scherer. Sintering of low-density glasses I: theory. *Journal of the American Ceramic Society*, 60(5-6) : p236–239, 1977.

# Chapter 4

# Solution Doping of FHD layers

## 4.1 Introduction

Solution doping of silica is an established technique that is widely used to incorporate rare-earth ions in fibres [1–4]. It has been used for the fabrication of planar lasers [5, 6]. The solution doping technique became widely used following the discovery of the amplification of light in a neodymium-doped fibre [7] and the first practical source for optical communication [8]. The technique was developed for fibres to produce single mode room temperature laser operation of a neodymium doped silica fibre [9] and then adapted to the planar format, mainly for the fabrication of lasers [10] however it cannot be considered to be a mature technique.

When silica is produced using the FHD technique, it is deposited as particles in contact with each other, separated by pores (see section 4.3). It is known from fibre fabrication techniques and work on planar structures that the pore size and the number of pores in the soot changes the amount of dopants that can be incorporated into the finished layer [11]. A small amount of work has been published on solution doping in a planar geometry, however this technique needed to be further developed to create active devices in photosensitive glasses.

In the remainder of this chapter, the principles of solution doping and of sintering of FHD soot will be explained. The different set ups developed for this thesis will be described and the resultant defects listed. A study of aluminium solution doping was performed in order to study the parameters affecting this process and the trends observed are detailed. A study of rare-earth ions solution doping is then related which led to the development of the photosensitive rare-earth doped layers used throughout the remainder of the work related in this thesis. Finally, the influence of doping on the consolidation temperature is studied.

## 4.2 Solution doping principles

The principle of solution doping involves a partially consolidated porous layer being immersed in an aqueous or alcohol solution of the selected dopant. Two main mechanisms have been identified for the incorporation of the dopants into the soot, the first of which is the physical mechanism: the soot acts as a sponge, taking up solution by capillary action. The dopants are deposited in the pores when the solvent evaporates. The consolidation of the glass then traps them inside the glass matrix. In this case, the surface area of contact between the solution and the soot changes the amount of dopants that is incorporated. The second mechanism is where the atoms are chemically trapped. The dopant is in its ionic form and thus bonds are created between the dopant ions and the soot ions. Evidence has previously been reported for both mechanisms [12]. The solution doping method has been used to dope layers with rare-earth materials such as neodymium [8], erbium [13], thulium [14] and more. Dopants other than rare earths can be included in the layer such as boron, aluminium [15] or CdS [11].

In this work, the initial stages for the development of the solution doping set up have been carried out using aluminium as the dopant. This is because aluminium is more easily inserted in the glass matrix by solution doping thanks to its small ionic size compared with rare earths, and it can easily be measured using EDX where the x-ray fluorescence of excited electrons is observed, each atom exhibiting characteristic x-ray emission.

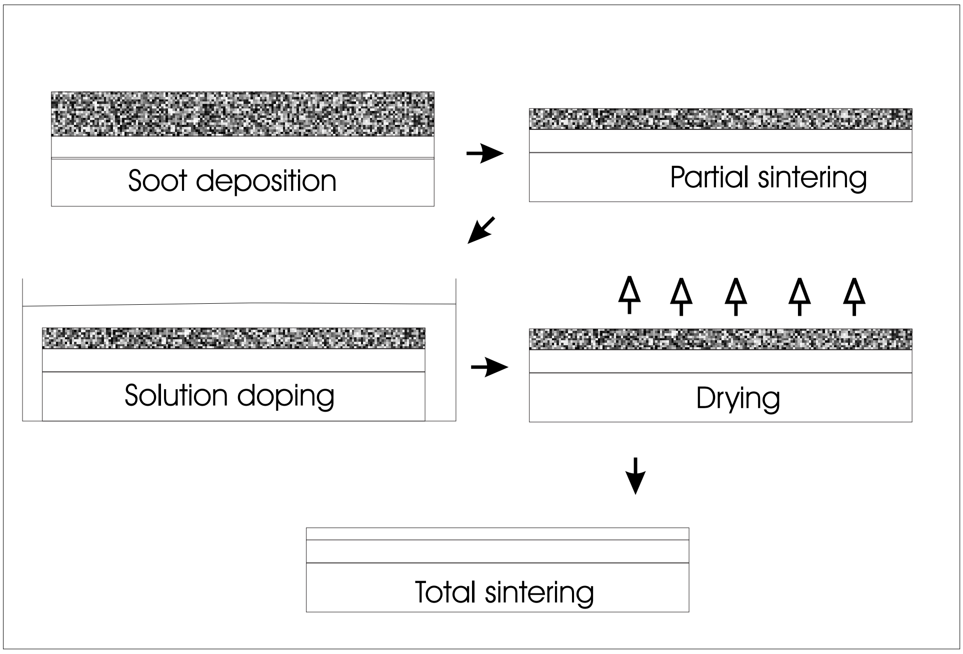

Figure 4.1: Principles of solution doping

The sample to be doped was inserted in the solution and left for one hour at room temperature so the dopants could be absorbed. The concentration of dopants can be modified by changing the concentration of dopants in the solution, the immersion time and the state of pre-sintering. In these experiments, the immersion time was kept constant and only the strength of the solution and the pre-sintering treatment were altered to tailor the amount of dopants incorporated in the layer. The sample was then removed from the solution. It was left to dry at room temperature for about half an hour, or until the soot was white indicating that it was dry. The drying was completed by placing the sample in a furnace at 200°C for another half hour, inside a petri-dish to reduce particle contamination from the atmosphere. The layer could then be consolidated in the furnace (see figure 4.1).

## 4.3 Pre-sintering of the soot

When the raw FHD soot was solution doped, the soot tended to disintegrate in the solution as the fragile soot matrix is easily damaged. Hence, the FHD soot needs to be pre-sintered in order to strengthen the matrix and allow solution doping. During the FHD process, the particles form a tenuous network containing pores. They adhere together through molecular forces [16]. The skeleton of the glass matrix is formed by sintering the particles of the layer together, by heating of the sample. This induces an increase in particle size and pore size as the pores agglomerate during the consolidation process. The pores also become more spherical due to material transfer between the particles. At the interface between two molecules, a neck is formed, where the material transfer takes place. These pores then out-diffuse during the final step of the consolidation process, leading to a fully dense glass layer [17]. The minimum pre-sintering step is desired because it permits a maximum and uniform absorption of dopants. If the glass is too fused, i.e. too close to consolidated state, it is more likely to have isolated dopant centers which lead to non-uniform doping [18]. Hence, we need to find the minimum pre-sintering temperature. SEM photography is used to show the growth of the particles and the out-diffusion of the pores. Figure 4.2 shows doped silica raw soot as produced by our FHD system while figures 4.3 and 4.4 show two different states of pre-sintering of FHD soot. We can see the particles and the pores becoming bigger as the pre-sintering temperature increases.

With the layer shown in figure 4.4, the doping process would give rise to uneven and low dopant concentration, as the skeleton of the matrix is made of relatively big particles. For this composition of the soot (10at% for $POCl_5$, 12at% for $BCl_3$ and 20at% for $GeCl_4$ in the vapour stream), the solution doping process has been found to be feasible for a pre-sintering step of fifteen minutes at temperatures above 775°C, but the layer is still quite fragile and requires very careful handling of the sample. The most successful treatment is forty five minutes at 800°C. The relative density of the soot has been calculated by measuring the layer thickness for different pre-sintering stages using an optical microscope and an SEM, and com-

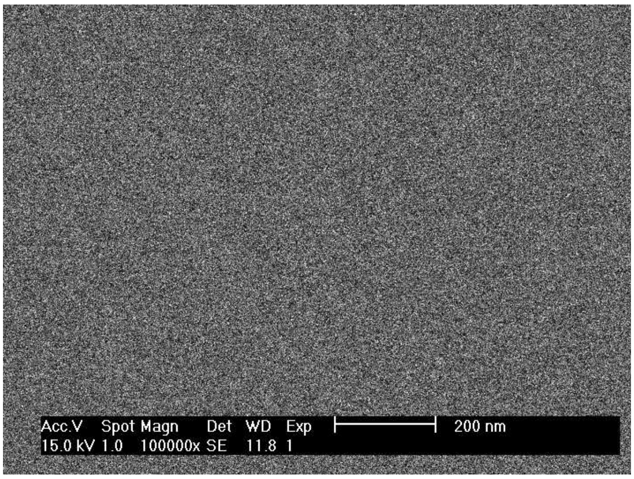

Figure 4.2: SEM image of raw FHD soot

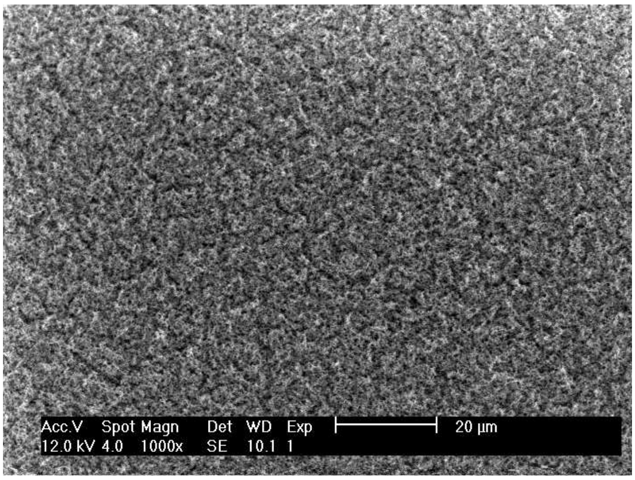

Figure 4.3: SEM image of FHD soot presintered at 775°C for 15 minutes

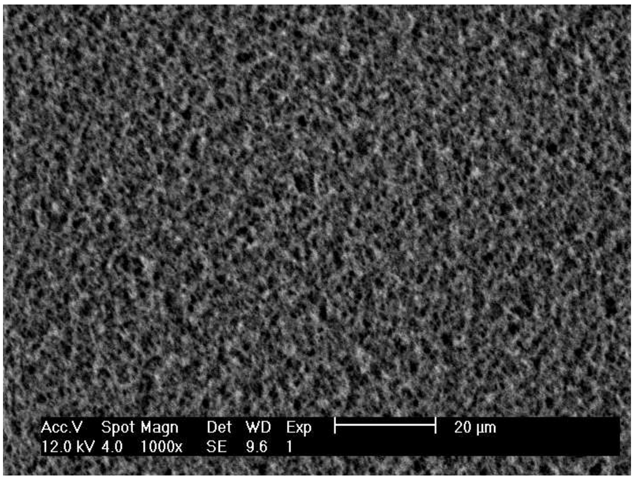

Figure 4.4: SEM image of FHD soot presintered at 850°C for 15 minutes

paring it with the consolidated layer thickness. The layer thickness has been measured using an optical microscope and the SEM for raw soot and pre-sintered soot treated 15 minutes at 750°C, 775°C, 800°C, 850°C, 900°C, 950°C, 1000°C and 1075°C. The thickness has been found to decrease with increasing temperature (Fig. 4.5).

## 4.4 Solution doping set up and induced defects

As we generally used the minimum practicable pre-sintering treatment for the samples, the skeleton of the glass matrix was still very fragile. It was important to find a gentle way of immersing the layer into the solution as turbulence can affect the soot, resulting in various consolidation problems. Different set ups have been investigated in order to get the best quality layer.

The first experiments were conducted using a set up very similar to that used for fibre doping (Fig 4.6). The sample is placed in a beaker and the solution is removed from a bottle and inserted slowly in the beaker containing the sample by means of a peristaltic pump. This is meant to minimize the turbulence the soot is submitted to, in order to limit the defects in the resulting glass layer. The solution is carried between the bottle and

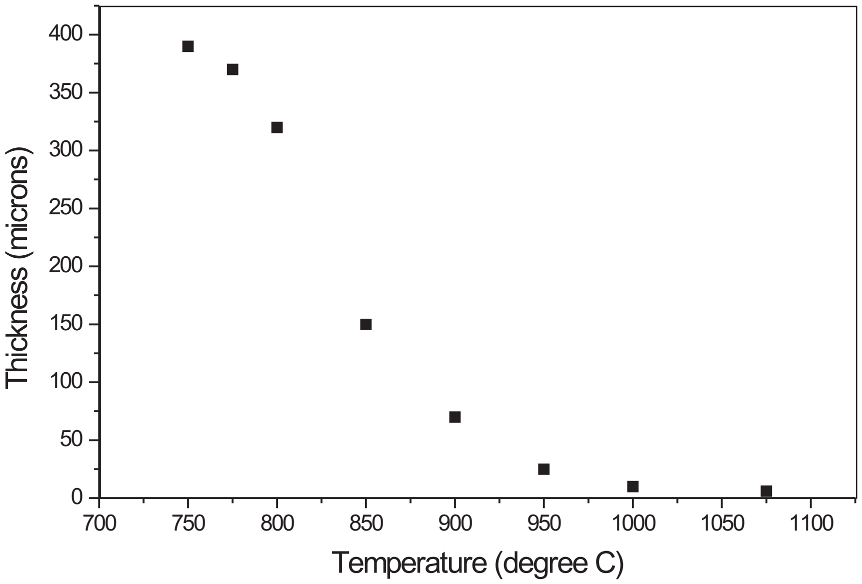

Figure 4.5: Thickness of the soot related to pre-sintering treatment

the beaker in a plastic pipe. A filter was placed at the beaker end of the pipe to avoid contamination. It was found that the contamination due to the solution itself was negligible so the filter was discarded in the later experiments. After a duration of one hour, the solution is removed again using the peristaltic pump, and the sample left to dry.

The peristaltic pump was found not to insert the liquid in a smooth manner but by fits and starts. This causes the plastic pipe connected to the pump to jerk and disturb the solution. If the sample is placed flat on the

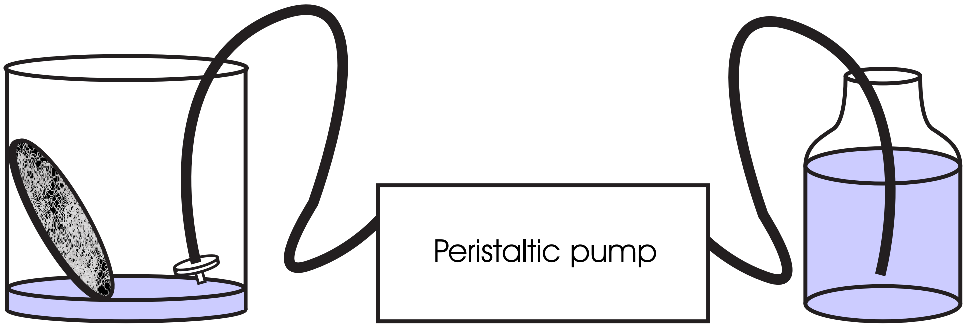

Figure 4.6: Solution doping set up

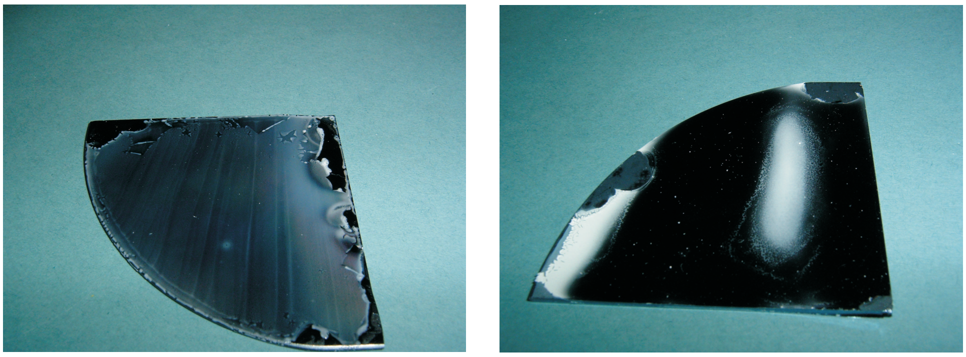

Figure 4.7: defects induced by solution doping in set-up 1: a on the left, b on the right

Figure 4.8: defects induced by solution doping in set-up 2

bottom of the beaker, the soot layer gets unstuck and lifts off in the solution. If the sample is placed at an angle, each jerk from the pump disturbs the soot. This can be noticed whilst the solution evaporates from the soot. This induced parallel-line defects in the resulting glass layer as illustrated in figure 4.7a. In figure 4.7b, the plastic pipe used to convey the solution touched the sample and disturbed the soot stopping it from consolidating properly.

To avoid the regular disturbance of the soot by the peristaltic pump, the solution was introduced by hand. The sample was placed in the beaker and the solution poured very slowly against the side of the beaker. The sample was then removed from the beaker after a one hour treatment. Unfortunately, this induced even more turbulence and led to badly consolidated layers and even unstuck layers of soot that would fly off when moved near the consolidation furnace (see figure 4.8).

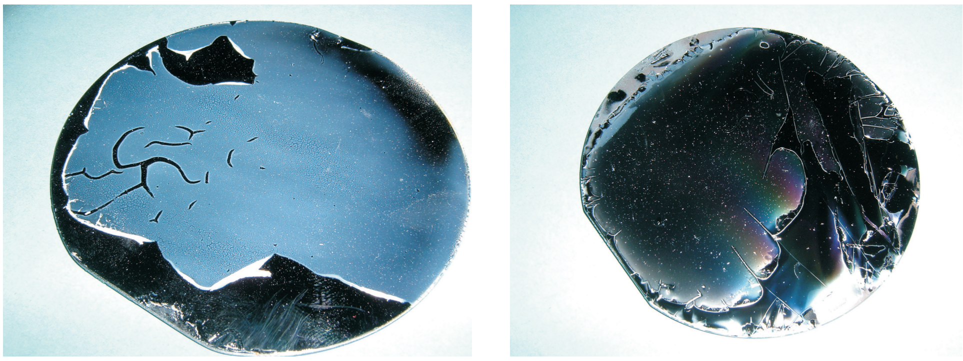

Figure 4.9: defects induced by solution doping in set-up 3

To avoid the turbulence in the solution as much as possible, it was decided to insert the sample into the solution rather than the opposite. The solution is placed in a beaker. The sample is then inserted in the beaker very cautiously, up against the side, at an angle of approximately 45°. After a period of an hour, the sample is removed from the solution in the same manner. If the sample is not inserted and extracted very slowly and at a constant rate, many problems can arise. The resulting glass layer can contain localised defects or unconsolidated areas, or the soot layer can break or even fly off the substrate when moved close to the consolidation furnace (see figure 4.9).

## 4.5 Study of solution doping

Experiments were performed with boron-germanium doped soot deposited onto silicon wafers with the FHD system. The concentrations given in this section have been measured using EDX. Unfortunately, this is not a very accurate method and the values are therefore not used as absolute values. Nevertheless, it gives a good basis for comparative measurements and the trends are believed to be correct.

It was found that the samples disintegrated during solution doping if they were treated at 600°C for 15 minutes and 1 hour, indicating that they were under-pre-sintered. Samples treated at 800°C for 15 and 30 minutes were also under-pre-sintered, although the soot did not disintegrate, the layer

| Pre sintering | Dopant concentration in the soot layer (at%) |
|---|---|
| 800°C for 45 minutes | 10 |
| 1000°C for 15 minutes | 2.5 |

Table 4.1: Concentration of erbium in the soot layer as a function of pre-sintering treatment

cracked while drying. However, solution doping is possible if the sample is pre-sintered at 800°C for 45 minutes or more, or at a higher temperature. By solution doping these samples for one hour at room temperature in a solution of 0.041M of $AlCl_3$-$6H_2O$, then analyzing the composition using the EDX technique, the amount of dopant included in the layer was measured.

The two samples have been prepared in the same manner, the only difference being the degree of pre-sintering. If the sample has been pre-sintered at 800°C for 45 minutes, the dopant concentration of rare-earth ions in the subsequent layer is measured to be 10 atomic percent. If the sample has been pre-sintered at 1000°C for 15 minutes, the amount is approximately 2.5 at%. Thus, there is a relation between the degree of pre-sintering and the dopant concentration included in the layer. The concentration included decreases when the layer is further consolidated prior to doping. This result has been represented in the table 4.1.

A more detailed study of the influence of the pre-sintering temperature on the incorporated quantity of dopants for a given time of 15 minutes on the same soot layer, still using aluminium as the dopant was performed. Four different temperatures have been used: 800°C, 850°C, 900°C and 950°C. For each temperature, the amount of dopants in the soot layer and in the consolidated glass layer has been measured using EDX. The atomic concentration of the dopant was seen to decrease towards the high temperatures(Fig 4.10 and 4.11), following the trend observed in the density of the soot (Fig. 4.5). This indicates that the amount of dopants incorporated is related to the contact surface area with the soot in agreement with the mechanism described in section 4.2.

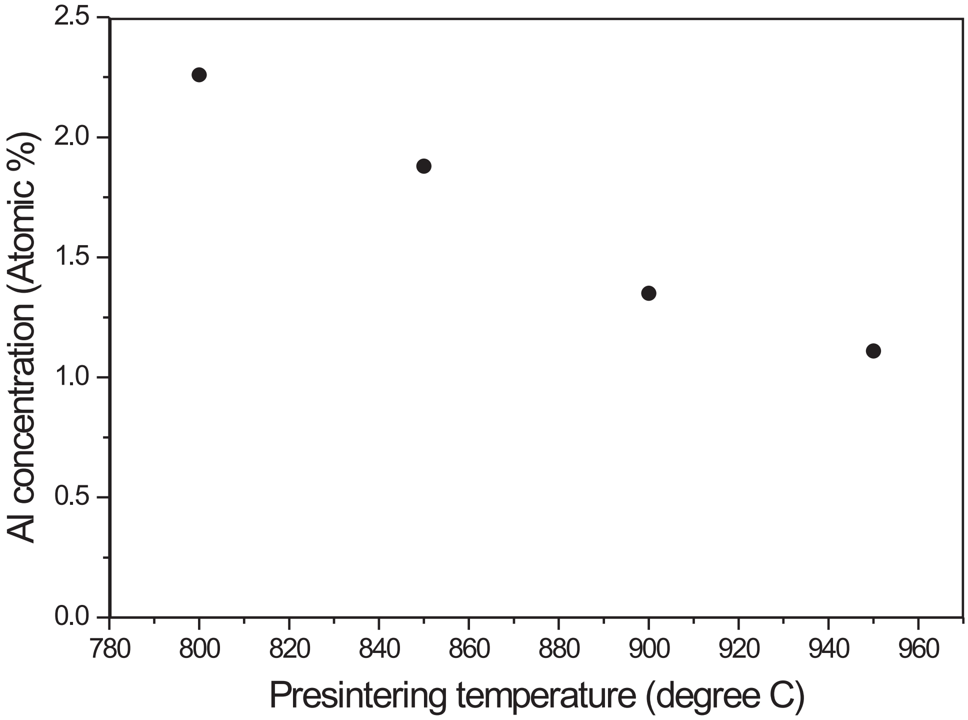

Figure 4.10: Concentration of aluminium in the soot as a function of pre-sintering temperature, solution strength 0.041M

Another parameter affecting the dopant concentration in the glass layer is the concentration of the solution used for the solution doping process. Different solutions have been used to dope samples. The graphs 4.12 and 4.13 display the dopant concentration in the layer as a function of the dopant concentration in the solution. Unsurprisingly, it was found that the more concentrated the solution, the higher the dopant concentration in the processed layer with an approximately linear relationship. The dopant concentration in both the soot (Fig. 4.12) and the consolidated glass (Fig. 4.13) were analysed using the EDX technique. The gradient for the consolidated glass layer is about half of that for the soot layer. The difference in the amount of dopants between the two layers is attributed to volatisation of the dopant during the consolidation treatment. It may also be due to diffusion as aluminium diffuses very easily.

For the sample doped with a solution of 0.041M of $AlCl_3$-$6H_2O$, the consolidated layer has a white colour that suggests that phase separation is happening [19]. It is likely that cristobalite and sillimanite crystallise in

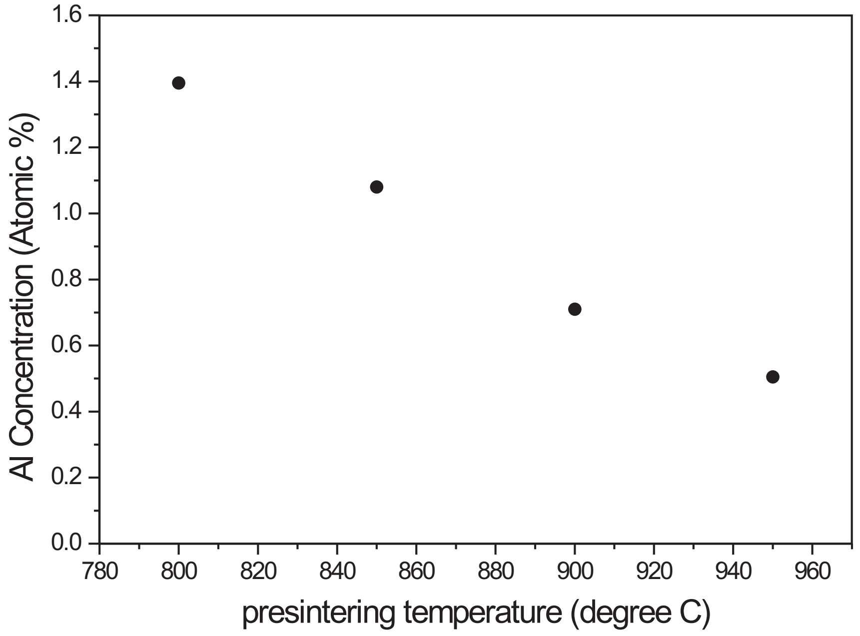

Figure 4.11: Concentration of aluminium in the glass layer as a function of pre-sintering temperature, solution strength 0.041M

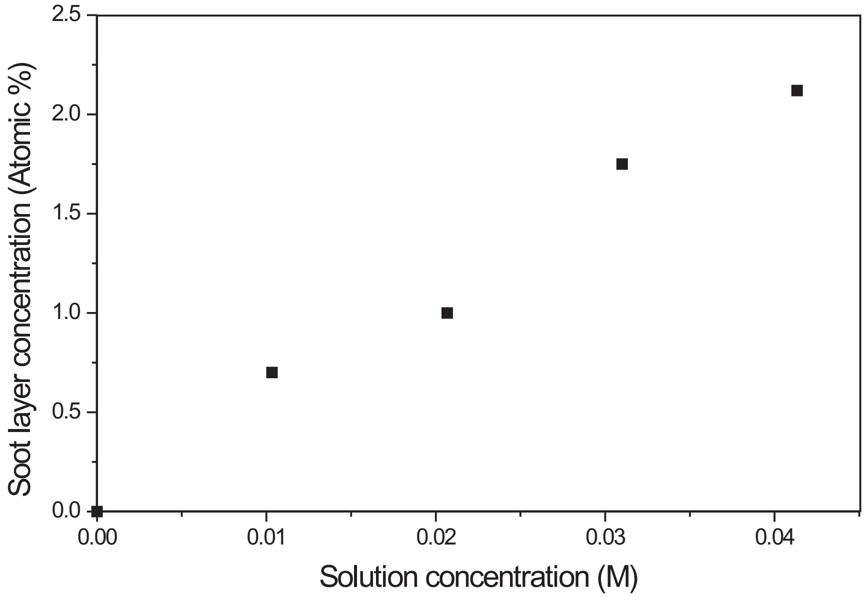

Figure 4.12: Concentration of aluminium in the soot as a function of solution concentration, presintering 15min at 800°C

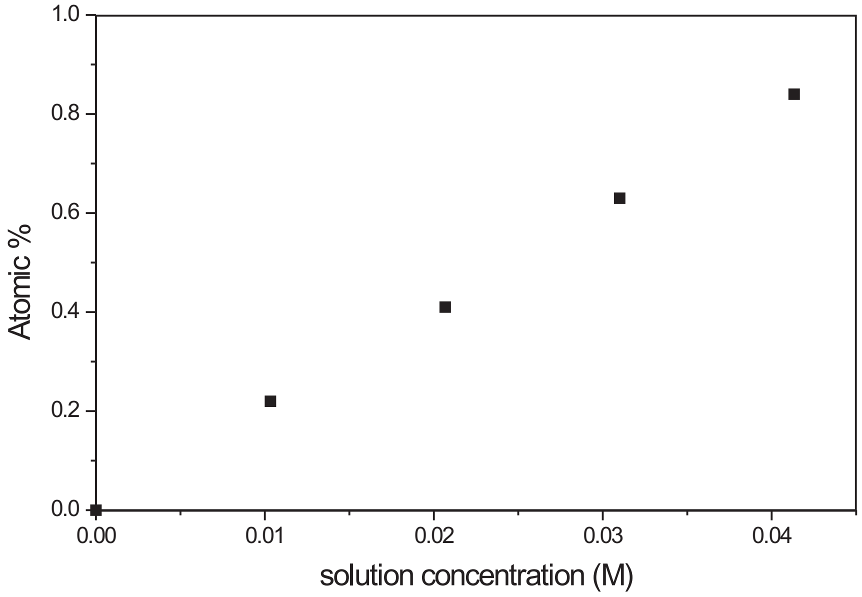

Figure 4.13: Concentration of aluminium in the glass as a function of solution concentration, consolidation 3h at 1400°C

the layer causing devitrification [20], a phenomenon where tetrahedra of vitreous silica become arranged into cristobalite crystals [21]. A lower concentration of aluminium chloride in the layer solves this problem. If the concentration of the solution is above 0.03M, devitrification or phase separation occurs. The layer is much rougher than was usually observed for the sample doped with the solution of 0.041M (variation: about 800nm). For the other solutions, the flatness is very good (variation: about 30nm).

## 4.6 Rare-earth doping: study

Material characterisation of rare-earth solution doped samples has been realized using erbium and neodymium dopants. Erbium was used for the first experiments and neodymium for more precise characterisation as it is known to exhibit exceptionally favourable characteristics for laser action [22]. Ytterbium and thulium solutions have also been used to make samples but the emphasis was placed on spectroscopy more than material

study. The concentration dependence of these ions has not been characterised as thoroughly. Therefore, they will not be mentioned in this section. More information for these ions can be found in chapter 5.
Different erbium solutions have been used to dope the standard core layer of our three-layer system. The layer was pre-sintered at 850°C or 875°C depending on the sample (see table 4.2). Three solutions have been used: the first one containing 0.01M of $ErCl_3$-$6H_2O$ and 0.00083M of $AlCl_3$-$6H_2O$, the second one 0.005M of $ErCl_3$-$6H_2O$ and 0.0016M of $AlCl_3$-$6H_2O$ and the third one 0.031M of $ErCl_3$-$6H_2O$ and 0.31M of $AlCl_3$-$6H_2O$. The concentrations of erbium ions have been obtained using EDX technique and are expressed in normalised weight percent. This does not allow direct comparison with the results for neodymium or aluminium. Nevertheless, it was again observed that an increase in the pre-sintering temperature induces a decrease in the concentration in the resulting layer and that an increase in the solution strength induces an increase in the concentration in the resulting layer as shown in table 4.2.

The inclusion of neodymium ions into the silica layer has been studied as a function of the solution strength and the pre-sintering temperature. The subsequent dopant concentrations have been measured using the secondary ion mass spectrometry technique (SIMS) at LSA in Loughbourough (see figure 4.14). This technique is more precise than EDX therefore the data given in this section are thought to be much more accurate than that recorded for aluminium doping. The effect on the refractive index has also been studied for both erbium and neodymium doped substrates. The re-

| Pre sintering temperature (°C) | solution used (M of $ErCl_3$-$6H_2O$) | Dopant concentration (norm wt%) |
|---|---|---|
| 850 | 0.005 | 2.3 |
| 875 | 0.01 | 1.57 |
| 875 | 0.031 | 3 |

Table 4.2: Concentration of aluminium in the soot layer as a function of pre-sintering treatment

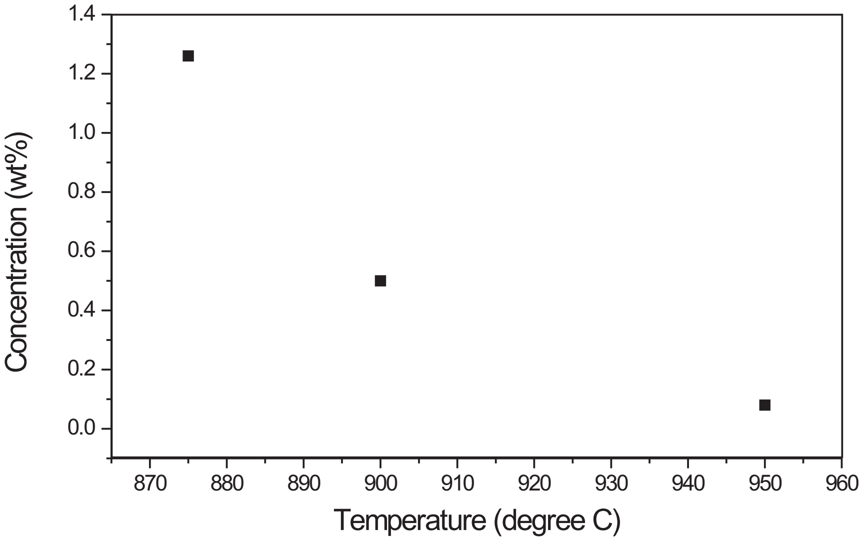

Figure 4.14: concentration of neodymium as a function of pre-sintering temperature

fractive indexes were measured using the prism coupling method with a He-Ne laser, giving the value for a wavelength at 633nm (see figure 4.15).

In these experiments, the composition used for the fabrication of the samples was the standard core layer of the three layer system. The samples were pre-sintered for 15 minutes and three different temperatures were used: 875°C, 900°C and 950°C. The samples were then doped using a solution containing a concentration of 0.011M of $NdCl_3$-$6H_2O$ and subsequently consolidated at 1225°C for one hour.

As seen for aluminium doping, an increase in the consolidation temperature results in a decrease in the concentration in neodymium in the resulting layer. The same trend can be observed for the refractive index. These two graphs can be compared to figure 4.5 that represents the density of the soot for different pre-sintering temperatures. The decrease in neodymium ions seems to follow the decrease in thickness of the soot, confirming the trend observed with aluminium. It also confirms the fact that the surface area of contact between the solution and the material influences the amount of dopants incorporated in the resulting layer.

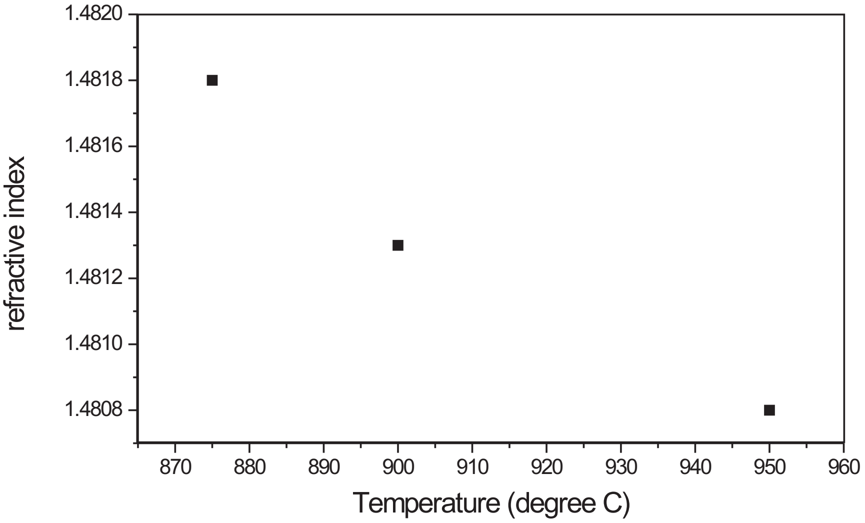

Figure 4.15: refractive index of neodymium doped glass as a function of pre-sintering temperature

To characterise the dependence of the concentration of neodymium in the resulting layer on the solution strength, the same standard treatment has been applied to the samples with only the strength of the solution used being altered. The composition used was once again that of the standard three layer system. It was pre-sintered for fifteen minutes at a temperature of 875°C. Five solution strengths were then used: 0.005M, 0.00875M, 0.011M, 0.02M and 0.03M and the samples were consolidated at 1225°C for one hour. The neodymium concentration was measured using SIMS whilst the refractive index was measured using the prism coupling technique at a wavelength of 633nm.

The concentration increase is expected to be linear. There are differences due to experimental errors, nevertheless the trends for the concentration and the refractive index are still very similar confirming the correctness of the results (see figure 4.16).

Surface profiles of a neodymium-doped core layer and an erbium-doped core layer are given for completeness. The flatness of the erbium and aluminium-doped layer (figure 4.19) can be seen to be somewhat worse

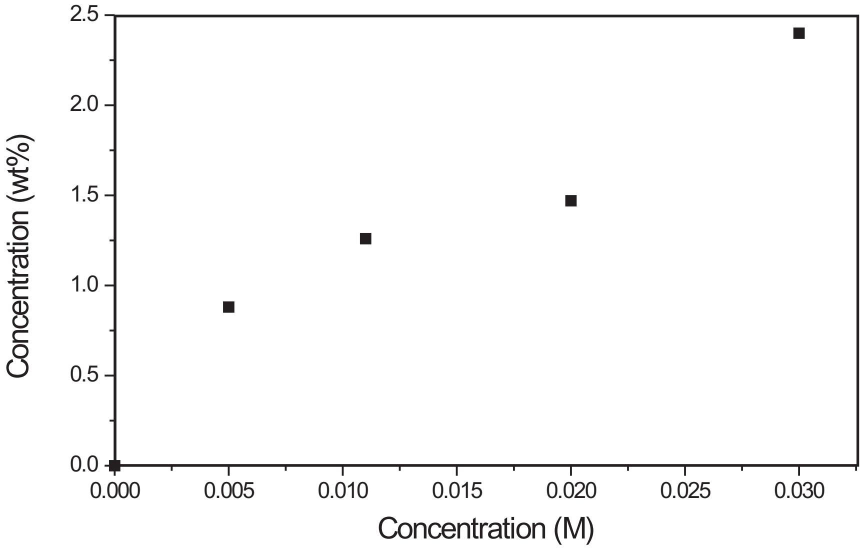

Figure 4.16: Incorporated concentration of neodymium as a function of solution strength

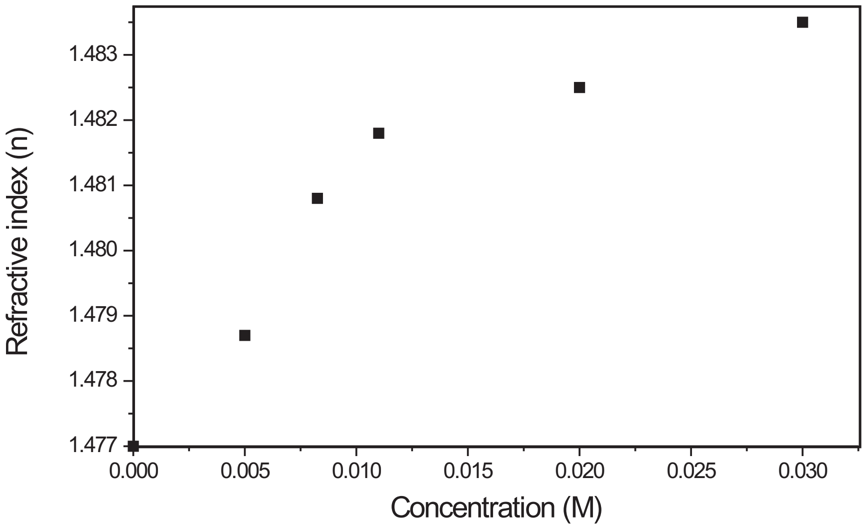

Figure 4.17: refractive index in neodymium as a function of solution strength

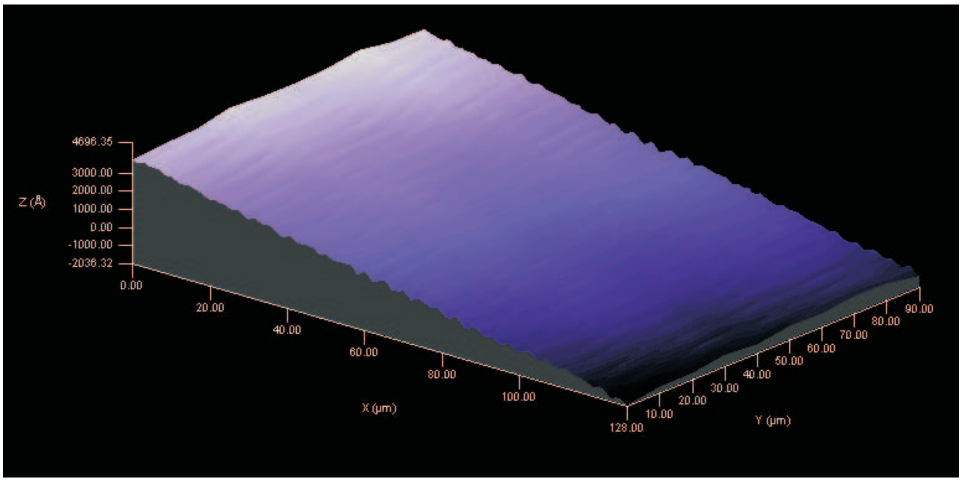

Figure 4.18: Surface profile of a layer doped with a solution of 0.011M of neodymium showing a roughness of approximately 50$nm$

than that of the neodymium-doped layer (figure 4.18). This is probably due to the fact that the erbium-aluminium solution was more concentrated. The neodymium solution strength is 0.011M whilst the erbium solution contained 0.031M of $ErCl_3$-$6H_2O$ and 0.31M of $AlCl_3$-$6H_2O$. Hence there would be a greater dopant density in the erbium-aluminium doped layer. This could explain the difference. Nevertheless, the flatness is very good, with a value of about 50nm for the neodymium sample and about 100nm for the erbium layer. The big peak seen in the bottom left corner on the erbium-doped layer profile (figure 4.19) is due to a contaminant incorporated into the layer during the consolidation.

## 4.7 Consolidation temperature

When consolidating passive FHD layers, there always is a window of possible temperatures for maximum quality layers. The size of that window depends on the composition itself. It is quite common to have a 50 degrees Celsius window, as is the case for the core layer of our three-layer index matched set. It has been found that depending on the amount of dopants incorporated in the layer, the temperature needed for complete consolida-

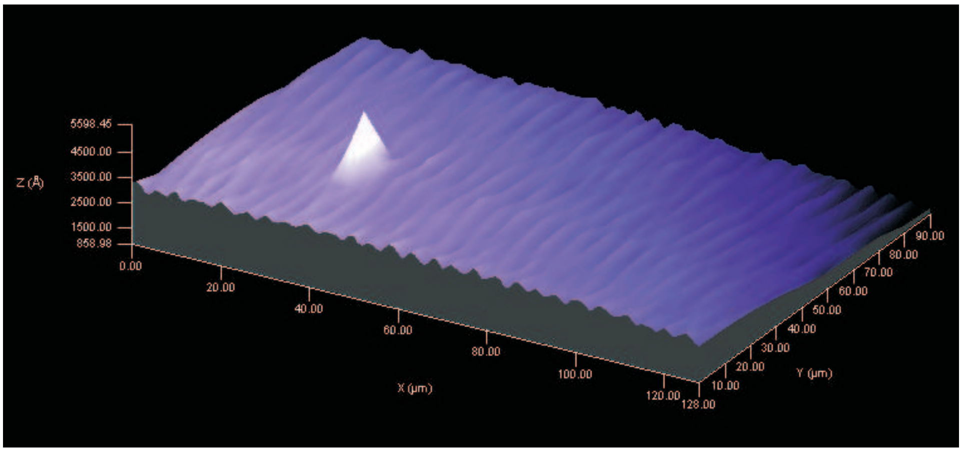

Figure 4.19: Surface profile of a layer doped with a solution of 0.031M of erbium and 0.31M of aluminium showing a roughness of approximately 100$nm$ or more. The large peak is due to particle contamination.

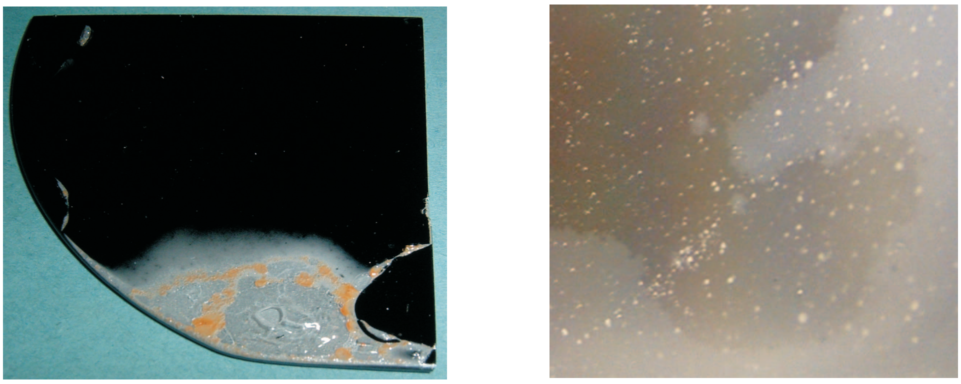

Figure 4.20: (a) Over-consolidated layer (b) overnight cracks

tion of the layer might need to be decreased. For instance, when the core layer was doped with a solution strength of up to 0.005M of $NdCl_3$-$6H_2O$, the temperature of 1250°C could be used with a resulting good quality layer. If the solution used was between 0.011M and 0.03M, the layer would be over-consolidated or would crack overnight (Fig. 4.20). A temperature of 1225°C was then used, giving a much better quality layer.

## 4.8 Summary

In this chapter, the solution doping of slab waveguides has been described. The history and the principles of solution doping have been related, as well as the protocol used by the author. Because of fabrication uncertainty and the fact that each composition will not respond in the same manner to doping, the results on the characterisation of the doping method cannot be used to obtain an absolute value but compilation of a comprehensive composition-property data set is beyond the scope of this thesis. Nevertheless, it is important to know how the different parameters affect the resulting doping value. From one given experiment, it is then possible to deduce what parameter has to be changed to obtain the desired value.

The influence of the pre-sintering temperature and of the solution concentration has been studied and related for aluminium and then for erbium and neodymium. The trends are very similar which lead us to believe that they are common to most ions that have been used during the course of this PhD.

Finally, the importance of the consolidation temperature has been discussed.

## 4.9 References

[1] S. Kobayashi, H. Nakagome, N. Shimizu, H. Tsuchiya and T. Izawa. Low-loss optical fibre with $Al_2O_3$-$SiO_2$ core. *Electronics Letters*, 10(20) : p410–411, 1974.

[2] P. Kiiveri and S. Tammela. Design and fabication of erbium-doped fibers for optical amplifiers. *Optical Engineering*, 39(7) : p1943–1950, 2000.

[3] J.E. Townsend, S.B. Poole and D.N. Payne. Solution-doping technique for fabrication of rare-earth doped optical fibres. *Optics Letters*, 23(7) : p329-331, 1987.

[4] D.L. Williams, B.J. Ainslie, J.R. Armitage, R. Kashyap and R. Campbell. Enhanced UV photosensitivity in Boron co-doped germanosilicate fibres. *Electronics Letters*, 29(1) : p45–47, 1993.

[5] J.R. Bonar, J.A. Bebbington, J.S. Aitchinson, G.D. Maxwell and B.J. Ainslie. Low-threshold Nd-doped silica planar waveguide laser. *Electronics Letters*, 30(3) : p229–230, 1994.

[6] R. Tumminelli, F. Hakimi and Haavisto. Integrated Optics Nd:glass laser fabricated by flame hydrolysis deposition using chelates. *Optics Letters*, 16(14) : p1098–1100, 1991.

[7] C.J. Koester and E. Snitzer. Amplification in a fiber laser. *Applied Optics*, 3(10) : p1182–1186, 1964.

[8] J. Stone and C.A. Burrus. Neodymium-doped silica lasers in end-pumped fiber geometry. *Applied Physics Letters*, 23(7) : p388–389, 1973.

[9] R.J. Mears, L. Reekie and D.N. Payne. Neodymium doped-silica single-mode fibre laser. *Electronics Letters*, 21 : p738–740, 1985.

[10] Y. Hibino, T. Kitagawa, M. Shimizu, F. Hanawa and A. Sugita. Neodymium-doped silica optical waveguide laser on silicon substrate. *IEEE Photonics Technology Letters*, 1(11) : p349–350, 1989.

[11] M.A. Fardad, E.M. Yeatman, E.J.C. Dawnay, M. Green, J. Fick, M. Guntau and G. Vitrant. Fabrication and characterisation of a CdS-doped silica-on-silicon planar waveguide. *IEE proceedings-optoelectronics*, 143(5) : p298–302, 1996.

[12] J.E. Townsend. The development of optical fibres doped with rare-earth ions. *PhD thesis, University of Southampton*, 1990.

[13] K. Hattori, T. Kitagawa, M. Oguma, Y. Ohmori and M. Horiguchi. Erbium-doped silica-based waveguide amplifier integrated with a 980/1530nm WDM coupler. *Electronics Letters*, 30(11) : p856–857, 1994.

[14] J.R. Bonar, M.V.D. Vermelho, A.J. McLaughlin, P.V.S. Marques, J.S. Aitchison, J.F. Martins-filho, and al. Blue light emission in thulium

doped silica-on-silicon waveguides. *Optics Communications*, 141 : p137–140, 1997.

[15] B. Wu and P.L. Chu. Fabrication of high concentration rare-earth-doped silica-based waveguide by MCVD method. *IEEE Photonics Technology Letters*, 7(6) : p655–657, 1995.

[16] D.S. Wilkinson and M.F. Ashby. The development of pressure sintering maps. *Sintering and catalysis: proceedings*, 10 : p474–476, 1995.

[17] W.D. Kingeri, H.K. Bowen and D.R. Uhlmann. Introduction to ceramics. *John Wiley and sons*, p469–555, 1960.

[18] G. Vienne. Fabrication and characterisation of ytterbium: erbium co-doped phosphosilicate fibres for optical amplifiers and lasers. *PhD thesis, University of Southampton*, 1996.

[19] Y. Ohmori, F. Hanawa and M. Nakahara. Fabrication of low-loss $Al_2O_3$-doped silica fibres. *Electronics Letters*, 18(18) : p761–763, 1982.

[20] J.R. Simpson and J.B. Macchesney. Optical fibres with an $Al_2O_3$-doped silicate core composition. *Electronics Letters*, 19(7) : p261–262, 1983.

[21] W.E. Worral. Clays and ceramic raw materials. *Applied science publishers Ltd*, 1975.

[22] W. Koechner. Solid-state laser engineering, Chap. 2. *Springer Verlag*, 1999.

# Chapter 5

# Channel waveguide fabrication

## 5.1 Introduction

The fabrication of a three-layer waveguiding structure, as described in previous chapters, provides vertical confinement of the light in the core by total internal reflection. The addition of a lateral confinement is required to lower the laser thresholds and allow routing of light. It would also provide an optical mode better suited to coupling to fibre-optic components and a means to integrate multiple functions on a single substrate. Two principal types of fabrication methods are often used to make channel waveguides in silica-on-silicon material : methods requiring masking and direct writing. A number of techniques are available but photolithography and subsequent etching is the most established technique [1]. This will be compared to UV-writing, a relatively new technique that provides lateral confinement through a localised increase in refractive index induced by a UV beam radiation. Here, a laser beam is focussed on the core layer of a sample which induces an increase of refractive index in the zone subjected to the radiation. The waveguide can be defined by scanning the sample under the beam to define the desired structure. This technique is discussed more in detail in section 5.2.2 and its merits are listed. The phenomenon of photosensitivity is then studied, followed by a description of the UV writing set up used. Finally, the results of the characterisation performed on channel waveguides and y-splitters realised during the course of this work are presented.

## 5.2 Review of PLC definition techniques

### 5.2.1 Photolithography and RIE

Photolithography and subsequent RIE is the most widely used approach for fabricating waveguides in silica-on-silicon. Photoresist is used to coat an existing slab waveguide (figure 5.1). It is spun into a thin film on the substrate. A mask is then used to protect certain zones of the photoresist during UV light exposure. The mask defines the waveguide shape with a resolution of under $0.5\mu m$ and is positioned using a mask aligner. The sample is then exposed to UV light through the mask and the photoresist is developed to leave either a positive or a negative image of the mask in the photoresist. The planar waveguide is then etched either by wet-chemical etching or reactive ion etching (RIE). The remaining resist acts as a mask to the etching process and the etchants have to be chosen so that the etching of the resist is negligible compared to the etching of the waveguide material. Wet etching of silicates consists in immersing the layer in a solution containing hydrofluoric acid (HF) [1]. This often results in channel walls not being straight due to the high isotropy of the process [2]. RIE is a dry, clean technique developed in the microelectronics industry [3] and is based on a combination of plasma and sputter etching. It provides a better anisotropy but a lower selectivity of the material etched [4]. After etching, the remaining resist is subsequently removed. Depositing an upper cladding layer then protects the waveguide, and sets the mode profile. The main advantage of this technique is that mass production of micron scale structure is easily feasible and it gives high quality definition of the waveguides. Also, a large refractive index change can be obtained by using very different materials for the core and the cladding. Nevertheless, this technique is expensive, and it is a long, multi-step process, making it unsuitable for the small-scale requirements of research.

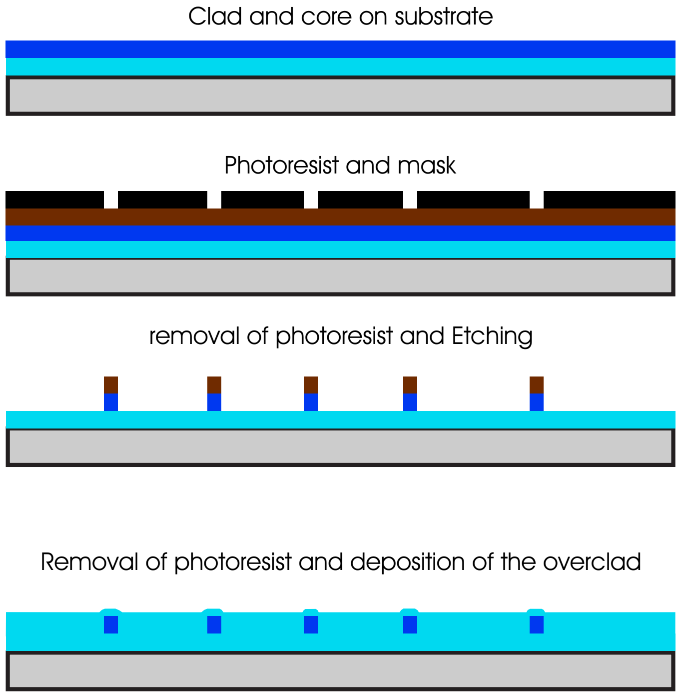

Figure 5.1: Photolithography and RIE

### 5.2.2 UV writing

Direct UV writing was developed relatively recently when compared to photolithography [5], but has already demonstrated performance in terms of loss that equals or surpasses photolithographic methods. The first channel waveguide defined by laser writing in germanium doped silica-on-silicon was written in 1993 and a refractive index increase of $2\times10^{-2}$ was reported [6], this was followed by a directional coupler in hydrogen loaded FHD planar silica in 1995 [7]. The method used by these two groups involved UV writing using a mask but no propagation loss lower than $1\text{dBcm}^{-1}$ was reported. The major breakthrough happened with Svalgaard and the first point-to-point writing of singlemode channel waveguides [8]. A photosensitive layer of the thickness of the desired structure is exposed to a focussed, high power UV laser beam (usually a continuous wave frequency doubled argon ion laser or a pulsed excimer laser). The refractive index increases, defining the channel waveguide. The UV beam is focussed to a spot of around $5\mu m$, which is slightly smaller than the size of the waveguide required. The sample is then translated under the beam

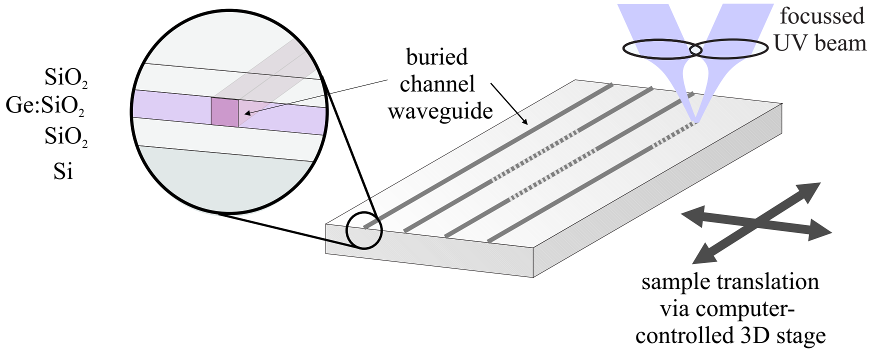

Figure 5.2: UV writing principle

to define the waveguide (see figure 5.2). The material characteristics and the laser fluence define the strength of the waveguide. Losses as low as 0.2dBcm$^{-1}$ have been reported [5] and devices such as splitters and couplers [9,10] have been realised. The major drawbacks of direct-UV-writing are the serial nature of the process making mass-production very time-consuming, and the limitations imposed on the choice of a substrate, since the material needs to be highly photosensitive. Nevertheless, the process is very flexible as it is based on a single-step principle. This is ideal for prototyping structures very rapidly. The size and strength of the channel waveguide can be varied during fabrication, allowing the fabrication of tapered and tapered index waveguides [2].

Bragg gratings are very desirable elements in integrated optics and UV writing naturally lends itself to the realisation of photo-written gratings. There are two possible routes : superimposition of gratings on previously defined channels and simultaneous channel and grating definition. This is reviewed in more depth in chapter 7. The first technique is to use a phase mask to create interference patterns. The interference of the diffracted plus and minus first order of the beam creates a diffraction pattern. The second technique, direct grating writing, consists of splitting the beam in two, and creating an interference pattern by crossing the two beams. The writing laser is modulated whilst the sample is translated, so that each illumination happens when the sample has moved by approximately the distance between two fringes [1]. The angle between the two beams determines the central period of the possible range of periods obtainable for the grating. Gratings of nearly any periodicity can be made by varying the modulation of the writing laser using an Acousto-Optic modulator (AOM). Direct grating writing is a very flexible technique however the precision required is very high, demanding sophisticated engineering.

## 5.3 Phenomenon of photosensitivity

The intrinsic photosensitivity in germanosilicate can give rise to a refractive index increases of the order of $10^{-4}$ [11]. Greater index changes have been observed but they are partially due to a modification of the stress and volume of the glass. The roles of these modifications is unclear [12]. In the following subsection, the principles of photosensitivity related to modifications of the lattice are described. Different methods have been used to increase the photosensitivity of the layer in order to obtain greater index changes. High temperature treatments have been reported [13]. Unfortunately, these also weaken the glass matrix and do not lead to refractive index changes of more than a few $10^{-3}$. Hydrogen loading of the sample before UV exposure has been found to be so far the most effective method [14]. It is reviewed in the remainder of this section.

### 5.3.1 Photosensitivity

Photosensitivity of silica is a light induced refractive index change and was first discovered in 1978 [15]. It is now widely accepted that photosensitivity is not the expression of a single mechanism. The index rise is the result of different mechanisms taking place simultaneously and depends on the material and the writing conditions. The role played by the modification of stress and volume of germanosilicate glass due to UV absorption remains unclear, so does the participation of the modification of distributed defects [5]. Nevertheless, the influence of point defects of the matrix is comparatively well understood. By doping the silica glass with a small amount of germanium, characteristics such as refractive index, UV absorption and melting temperature are modified, although the lattice structure stays almost untouched. This is due to the similarities between the germanium and silica atoms which have the same valence of 4. Nevertheless, this doping does insert defects of two types in the structure: point defects and distributed defects [2]. The interaction of these defects with the UV light are mainly responsible for the photosensitive nature of germanosilicate [16].

There are two types of point defects: diamagnetic where the electrons are paired and paramagnetic where they are unpaired [17] (see figure 5.3). Diamagnetic defects often appear during fabrication of the glass when a deficiency in oxygen occurs. They can take two forms, either a $Ge^{2+}$ defect or a Neutral Oxygen Vacancy where a germanium atom bonds directly to a silicon atom instead of an oxygen atom [18]. These are often classified under the term of Germanium related Oxygen Deficiency Centers (GODC). Paramagnetic defects can assume three forms [19]:

- Ge(1) electron-trap site where a free electron is trapped by a fully bound germanium atom
- GeE′ defects where a germanium atom is only bound to three oxygen atoms
- Non bridging oxygen hole centers where an oxygen atom does not participate in a bridge between a germanium and a silicon atom but is only linked to one Ge atom

The change in refractive index is thought to be due mainly to the matrix modification induced by UV exposure of GODC. The energy transferred to the system triggers the dissociation of electrons that leads to the modification and formation of paramagnetic defects. This alters the structure of the glass and therefore modifies the refractive index.

The variety of events responsible for this change in refractive index leads to three types of photosensitivity [20]. Type I is a linear increase in refractive index corresponding to the UV exposure time. Type IIa is a time

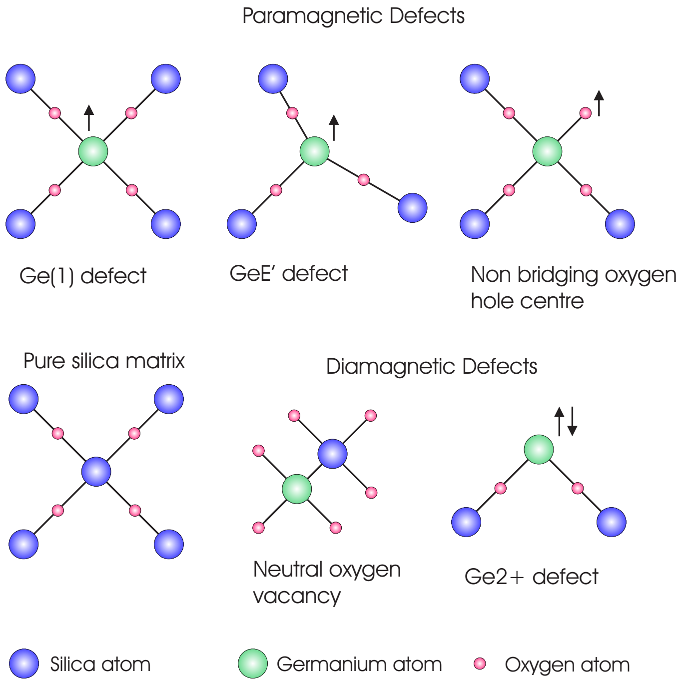

Figure 5.3: Structure of pure silica and germanosilicate showing principle defects

dependent decrease in index. It is associated with over-exposure. Type II is a very large index change resulting from physical damage due to the high intensity UV pulse at the absorbing/non absorbing layer boundary. Hence it is possible to obtain a large degree of control over the refractive index change by adjusting the UV exposure.

### 5.3.2 Deuterium loading

The following section reviews photosensitivity enhancement through deuterium loading of a germanosilica substrate layer. In fact, hydrogen can be used instead of deuterium with very little difference, but the disadvantage of using hydrogen is that it increases the number of OH bonds resulting in higher loss in the 1380nm spatial region. Otherwise, the diffusivity behaviour of both molecules are very similar, hence the same theory can be used.

Immersing the sample in a high pressure atmosphere of deuterium allows the incorporation of molecules in the structure. The loaded species are incorporated in vacancies or voids available in the matrix [21]. UV exposure inserts the particles into the glass matrix. Two effects are thought to participate in the refractive index rise of the material. The first is the formation of SiOD termination by the supply of enough energy to a Ge site that has a deuterium molecule in proximity [22]. The breaking of the Ge-O bonds, that are weaker than Si-O bonds, is triggered by either a thermal or photolytical process [22]. The second is the catalyst effect played by hydrogen on the photobleaching of GODC associated with the transition of diamagnetic to paramagnetic defects [23]. Every Ge site can potentially result in a GODC if enough hydrogen is provided, corresponding to a big improvement in the possible refractive index change. Hence, the concentration of deuterium present in the glass has a large effect on the photosensitivity of the material. It is therefore imperative to understand the theory behind the diffusion. A unidimensional equation derived from the Arrhenius equation can be used to express the diffusivity of hydrogen [14]:

$$D = \alpha e^{-\frac{E}{RT}} \tag{5.1}$$

where $\alpha$ is a proportionality factor, R is the gas constant and $T$ is the absolute temperature. For hydrogen, $\alpha$ is equal to $5.65 \times 10^{-4}$ and E is equal to 43.55$KJ/mole$. For deuterium, $\alpha$ is equal to $5 \times 10^{-4}$ and E is equal to 43.96$KJ/mole$ [14]. This shows how similar the behaviour of diffusion of both molecules is. The equilibrium concentration for hydrogen was found to be approximately 116$ppm/bar$ at 21°C [24]. Hence it is dependent on the pressure applied. For a pressure of 180 bar and a temperature of 21°C, it takes a value of about 2.09 mole%. The solubility of $H_2$ in silica is weakly dependent on temperature as it is proportional to $e^{8.67/RT}$ [11]. Higher temperatures result in lower solubilities. For a planar layer, the time necessary for a molecule to propagate in a sample of a distance $l$ is given by [25]:

$$\tau = \frac{l^2}{4D} \tag{5.2}$$

To determine the time necessary for the glass at the bottom of the glass layer to reach 95% of its equilibrium concentration, it is assumed that there is no indiffusion occurring through the silicon. For a film of a thickness $d$, it is then defined by [13]:

$$\tau_{0.95} = \frac{0.8d^2}{D} \tag{5.3}$$

The 95% equilibrium time for a 32 micron thick thin film is about 4 days. The rate of outdiffusion in planar samples was empirically determined at a pressure of 180 bar and can be expressed by:

$$\tau = -\ln(\alpha)\tau_0 exp(\frac{E}{RT} - \frac{E}{RT_0}) \tag{5.4}$$

with $\alpha$ the relative concentration compared to saturation, $\tau$ the decay time for a temperature $T$ and $\tau_0$ the experimentally determined decay time for a temperature of $T_0$. $\tau_0$ was measured to be 11.8 hours for 23°C [5]. With this value, the concentration can be calculated for any given time and temperature. The dynamics of the indiffusion rate are determined by the same equation as the diffusion rate [26]. Hence it takes about 4 days to reach 95% of the saturation value. The rate is dependent on the pressure as it determines the value of the solubility. In the work presented here, the samples are loaded in a stainless steel cell filled with a high purity deuterium gas at a pressure between 180 and 220 bar giving concentrations of deuterium of 2.09 to 2.55mole%. The samples are left in the deuterium atmosphere for 5 days or more to ensure saturation while avoiding long delays between sample fabrication and UV writing. The samples are then removed from the cell and placed in dry ice to slow down outdiffusion. It is assumed that if the writing times are short, the effects of outdiffusion during UV-writing are negligible.

## 5.4 Description of the UV writing set up

The UV writing system normally used for direct writing of optical channels into a planar glass sample is presented in figure 5.4. A new technique called Direct Grating Writing (DGW) has been developed in our group [27] to simultaneously write gratings and channels. The possibility of inserting gratings in an active channel waveguide can potentially lead to the fabrication of narrow line lasers such as DFB structure lasers. It could also allow

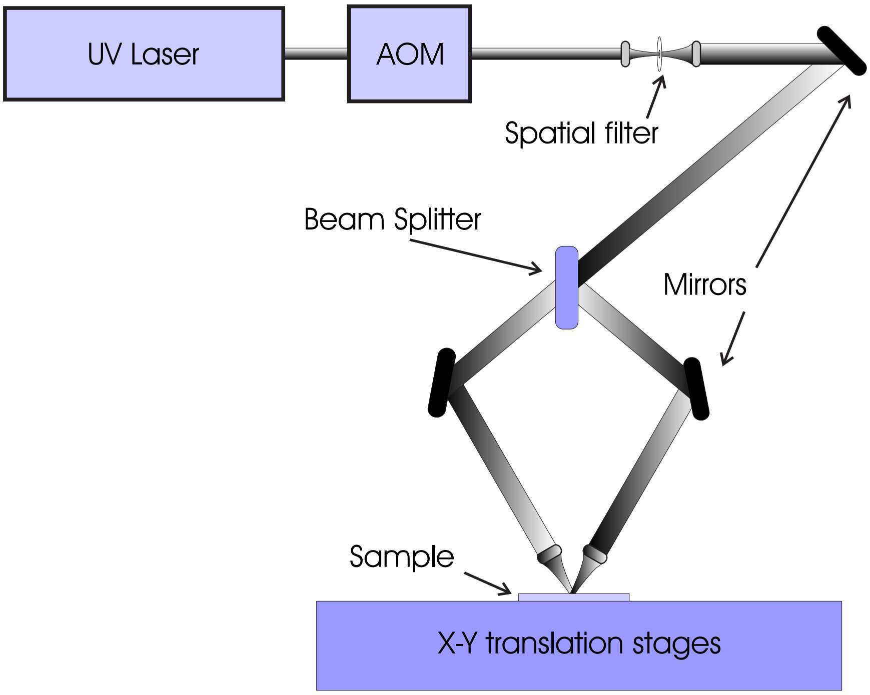

Figure 5.4: UV writing equipment

lasers, wavelength selective couplers, s-bends and splitters to be joined in a continuous device in a single processing step.

The laser used for UV writing is a frequency doubled argon ion laser operating at 244nm. The maximum output power is 500mW. The amount of power delivered to the sample is controlled by an acousto-optic modulator. Only the first order is used for UV writing, and the maximum efficiency of the AOM in that order is 74% [11]. Hence, the maximum usable power is 370mW. The beam shape is then tailored through a spatial filter and a beam expander. It consists of two pinholes that provide spatial filtering of the beam reducing the available power to 150mW but improving remarkably the beam quality and the stability of the beam. A set of mirrors is used to orientate the beam so that it is incident onto a beam-splitter. Both beams are then focussed using two independent lenses mounted on 3-d translational stages. The focal points are aligned so the intersection takes place at the beam waist of each beam. A UV interference pattern is produced by the intersection of the two tightly focussed coherent beams.

The AOM is used to control the duty cycle which is the percentage of time the beam is turned on during the writing process (see figure 5.4). If it is kept constantly on, during motion of the sample, the refractive index change produced by UV illumination is averaged out producing a continuous channel. If the writing beam is modulated, and the sample moved by such a distance that the beam is turned on again when the sample has been translated by approximately the distance of the period of the interference pattern, multiple exposures can lead to an extended Bragg grating. Also, as the period of the grating is determined by the modulation frequency of the AOM, and so chirped gratings or arrays of gratings of many different wavelength can be produced without having to modify the alignment of the system. The walls of the channels are effectively defined by the width of the average index change resulting from the UV illumination. As the same UV spot is used for both channels and gratings, the two waveguide dimensions are equal allowing optimum coupling. The sample is mounted horizontally on an x-y air bearing translation stage operated via a computer. The positional accuracy is about $0.5\mu m$ but an external interferometer improves that accuracy to around 1.24nm. A manual stage allows the user to bring the focus of the beam into the core layer and to level the sample. For more information on the UV writing set up, readers are directed to Greg Emmerson's thesis [1].

## 5.5 Doped layers produced

The first channel waveguides to be written during the course of this work were defined in an erbium-doped sample doped with a solution containing 0.005M of erbium and 0.0415M of aluminium. Channel waveguides were written in the core of 2-layer samples, ie. without upper-cladding, with a UV power of 100mW. The translation speed was varied between 10 and 120mm/min. Channels waveguides were obtained only for the lowest speeds (10, 20 and 30mm/min) and the Numerical Apertures (NA) were measured. The NA varied from 0.045 to 0.062. White light measurements were also taken but unfortunately, no absorption from the erbium ions was observed. Two facts were deduced from these experiments: firstly,

| Dopant | Solution strength M | Refractive index |
|---|---|---|
| Nd | 0.00875 | 1.4808 |
| Nd | 0.011 | 1.4818 |
| Nd | 0.03 | 1.4835 |
| Tm | 0.0139 | 1.4809 |
| Tm | 0.0274 | 1.482 |
| Yb | 0.011 | 1.4787 |
| Er+Al | 0.031+0.31 | 1.4821 |

Table 5.1: List of doped layers created

the resulting concentration of erbium was too low and secondly the next channels should be written using only the slow speeds. More layers were produced and the dopant contents analysed using the EDX technique before an acceptable amount of dopants, deduced from fibre fabrication data and absorption strength of each dopant at the corresponding absorption wavelength, was obtained.

Finally, seven different layers were produced that were thought to have a doping level high enough to allow material characterisation of UV-written channel waveguides. They are all based on the index-matched three-layer structure described in section 3.8.2. Neodymium, erbium, ytterbium and thulium have been used as active dopants. Three solution concentrations were used for neodymium, two for thulium and one for ytterbium and erbium. The parameters are listed in table 5.1.

## 5.6 Channel waveguide characterisation

A standard pattern of UV-writing conditions was used throughout this work. The samples were hydrogen loaded for $\geq$ 5 days and UV intensity power was kept at $100mW$. Waveguides were written at 5, 10 and 20mm/min on all compositions and also on an undoped sample to get

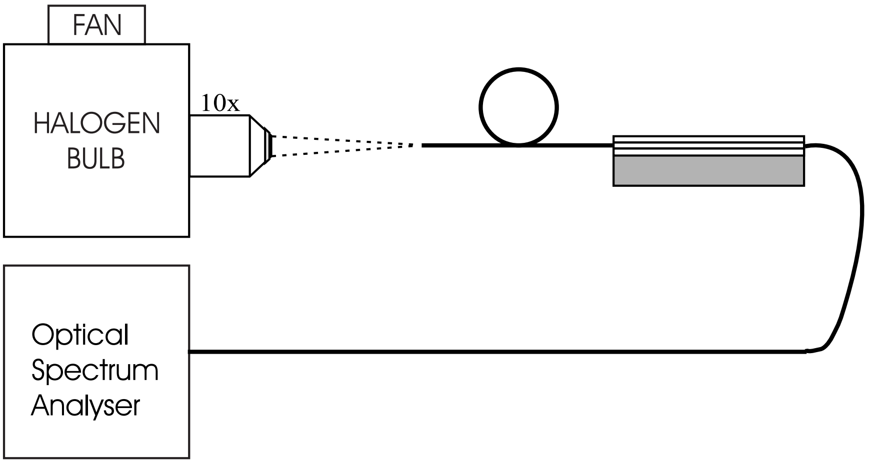

Figure 5.5: Apparatus for white light characterisation.

a comparison point. It can thus be observed whether rare-earth doping affects the photosensitivity of the glass and it can be confirmed that the effects observed are attributed to the active ions. It was found that 5mm/min writing speed gave better channels. These are the channels that have been characterised extensively and for which the data are related in the remainder of this section. Rare-earth ions have distinctive spectral characteristics and so the absorption and emission characteristics have been measured. The channel properties have also been studied and the NA and mode profiles are given in sections 5.6.4 and 5.6.5.

### 5.6.1 Absorption spectra

The measurement of the white light spectrum for a material allows the detection of absorption bands such as those associated with the absorption of a rare-earth ion. In the unexcited state, rare-earth ions in glass show characteristic absorption bands corresponding to electron transitions from the ground state to excited levels. The position and width of these bands are important factors to know as they will then be used for pumping of the ions. The equipment required to obtain an absorption spectra from the FHD fabricated samples consists of a broadband light source, a set of micrometer-controlled stages providing a fibre launch set-up and an Optical Spectrum Analyser (OSA). A schematic of the white light measurement equipment is given in figure 5.5. The broadband source is an air-cooled halogen bulb emitting in the 400-2000nm range. The output of the bulb is collimated and the focussing optimised to provide maximum launch efficiency into a standard multimode fibre, providing multimode propagation of the entire wavelength range. The other end of the fibre is butt coupled to a channel waveguide, leading to simultaneous excitation of the waveguide for all supported wavelengths. The coupling is optimised to obtain maximum output intensity using the stages. Another multimode fibre is then butt-coupled to the output of the waveguide and the coupling optimised to collect the signal and transmit it to the OSA. The graph obtained must be compared to the system dependent response, which means an absorption spectrum has to be plotted when the coupling is done from fibre to fibre, with no sample in between. This ensures that the absorption lines observed are due to the sample and not the system.

The spectral absorption characteristics of the four ions used for fabrication of samples can be seen in figures 5.6, 5.7, 5.8, 5.9 and 5.10. The respective absorption lines of each ion has a known absorption strength coefficient [28]. Using these and the amplitude of the corresponding absorption peaks, an approximation of the doping levels can be calculated. They are listed in table 5.2 for each major absorption line. Unfortunately, this technique has a high uncertainty as can be noted in the difference between the four strong absorption lines for the neodymium sample or the two strong absorption lines for the erbium sample.

### 5.6.2 Lifetime measurements

Rare-earth ions emit fluorescence which is the result of an excited ion decaying to its ground state. The fluorescence lifetime is defined as the time for the emission intensity to decay to $e^{-1}$ of its original value. It is dependent on the composition of the host glass. It can also be reduced because of energy sharing by two neighbouring ions if the doping level is high. This is known as concentration quenching. It is important to measure the fluorescence decay time as too low a value would reduce the efficiency of

| Dopant | wavelength nm | absorption strength dB/km/ppm [28] | measured concentration ppm |
|---|---|---|---|
| Nd | 590 | 227 | 5874 |
| Nd | 750 | 88 | 8265 |
| Nd | 810 | 100 | 8430 |
| Nd | 890 | 38 | 7336 |
| Er | 980 | 9 | 9876 |
| Er | 1535 | 52 | 8654 |
| Tm | 780 | 24 | 8333 |
| Yb | 970 | 88 | 9090 |

Table 5.2: List of solution doped layers

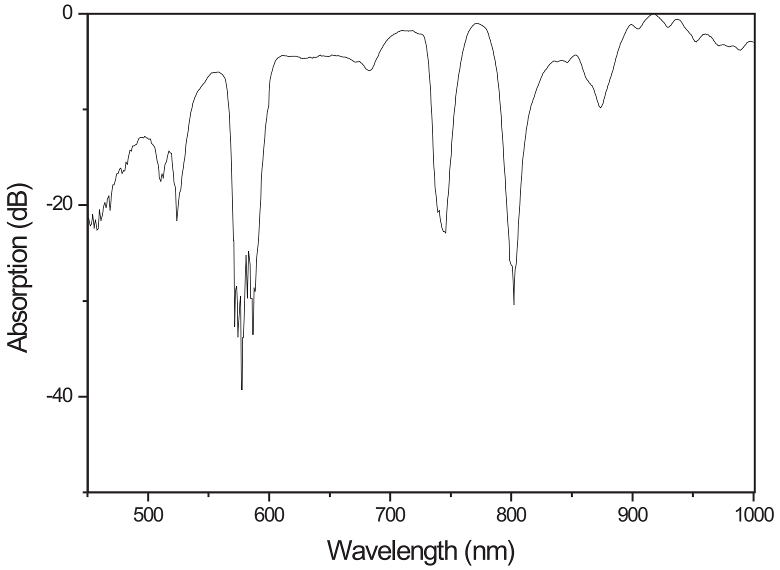

Figure 5.6: White light spectrum of a 30mm long neodymium-doped sample.

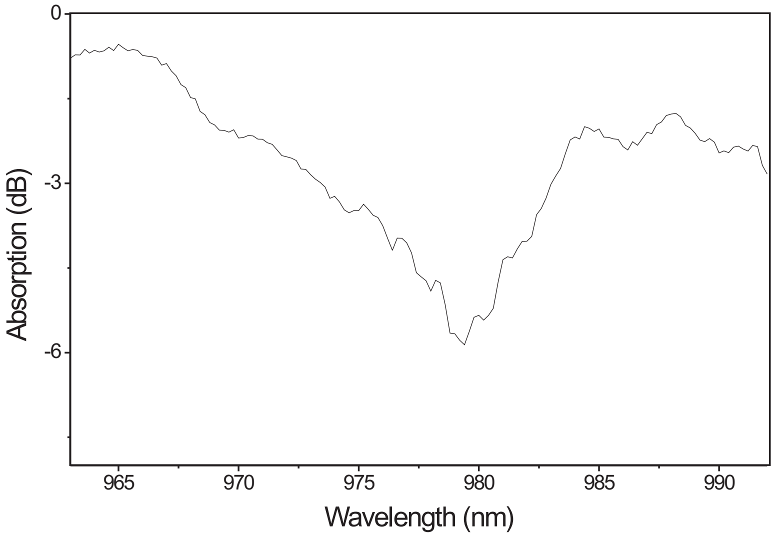

Figure 5.7: White light spectrum of a 45mm long erbium-doped sample at 980nm.

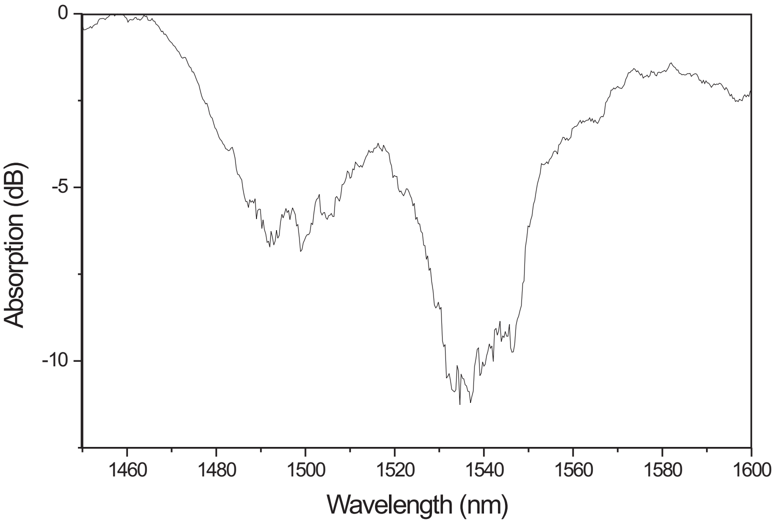

Figure 5.8: White light spectrum of a 20mm long erbium-doped sample at 1535nm.

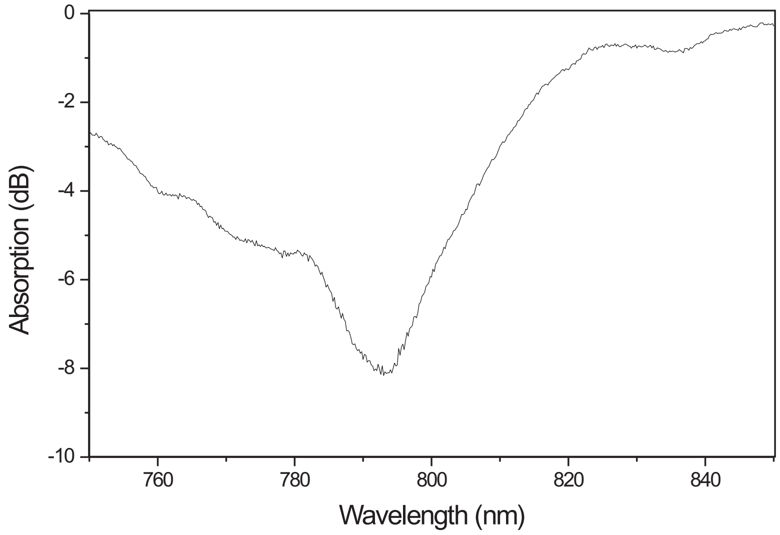

Figure 5.9: White light spectrum of a 20mm long thulium-doped sample.

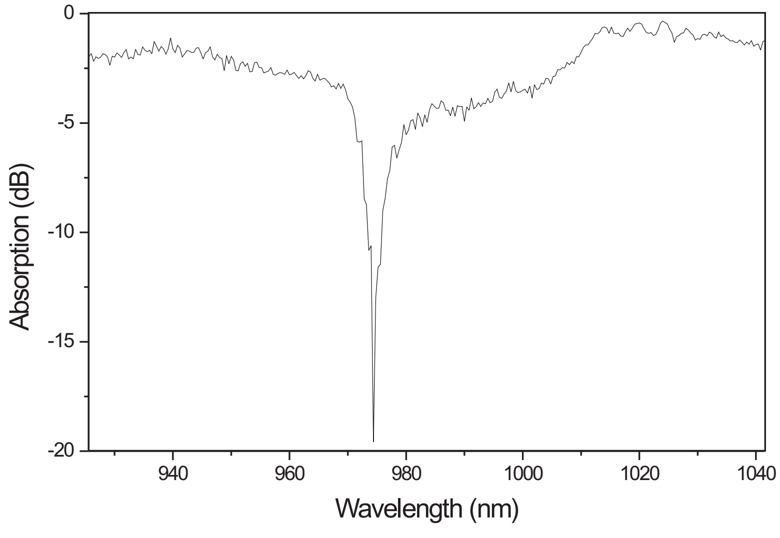

Figure 5.10: White light spectrum of a 10mm long ytterbium-doped sample.

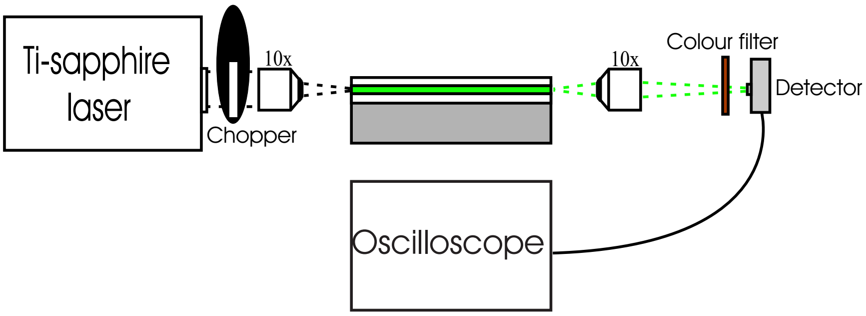

Figure 5.11: Apparatus for lifetime measurements.

the lasing or even in some cases prevent it.

The experimental configuration represented in figure 5.11 was used to measure the fluorescence lifetime for radiative transitions for the four active ions investigated. A tunable Ti:sapphire laser was used to excite the dopants at a suitable pump wavelength. An optical chopper was placed before the input objective and the coupling was optimised to obtain the strongest fluorescence signal. The output is collected by a microscope objective and focussed through a colour filter used to remove the remaining pump signal onto a detector connected to a digital oscilloscope.

The fluorescence lifetime of neodymium for the 1.06$\mu m$ transition is known to be about 500$\mu s$ in germanosilicate and phosphosilicate fibres [28]. The lifetime of the $^4F_{3/2} \Longrightarrow ^4 I_{11/2}$ transition was found to be between 237 and 268$\mu s$ using a silicon detector. This is similar to the value of 250$\mu s$ measured by Hattori et al [29] for a non uniform distribution of $Nd^{3+}$ in planar silica. No noticeable difference was observed between the lifetime of the sample doped with a 0.011M solution of neodymium and the sample doped with a 0.00875M solution.

The fluorescence lifetime of erbium is known to be about 10$ms$ in germanosilicate and phosphosilicate fibres [30]. Nevertheless, lifetime values as low as 5 or even 2$ms$ have been reported in heavily doped planar silica [31]. With little variation due to the pump power, lifetime values of 2 to 2.5$ms$ were observed in the solution doped samples.

Thulium fluorescence lifetime is very host dependent. Values of 250$\mu s$ and

200$\mu s$ have been reported for germanosilicate and phosphosilicate respectively [28]. In silica-on-silicon waveguides, a fluorescence lifetime of 280$\mu s$ was witnessed by Bonar et al for homogeneously doped glass, and 81$\mu s$ when quenching occurred [32]. In this work, the thulium ions produced a fluorescence signal with a decay time of approximately 50$\mu s$.

For ytterbium doped silica, lifetime values of 840 to 990$\mu s$ have been reported [33, 34]. The samples used in the course of this work exhibited shorter values of 717$\mu s$.

Although the relatively short value witnessed for ytterbium could simply be due to the glass host composition, the more pronounced shortening observed for the other ions suggests the occurrence of a quenching phenomenon, probably clustering.

### 5.6.3 Fluorescence spectra

If a sample is pumped with a laser source of the appropriate wavelength, the spontaneous decay of the excited electron to its ground state emits a weak fluorescence signal. The samples must be pumped at low intensity to reduce Amplified Spontaneous Emission (ASE) which distorts the emission spectrum. The equipment used to plot the fluorescence spectra is described in figure 5.12. It comprises a tunable Ti:Sapphire laser used to excite the rare-earth ions. The pump signal is launched into the core layer using a microscope objective. The fluorescence spectrum is collected by another microscope objective after passing through a colour filter to remove the remaining pump signal and coupled into a fibre. It is then launched into and recorded by an Optical Spectrum Analyser (OSA). The fluorescence spectra are provided in figures 5.13 to 5.15 except for the thulium doped sample. No fluorescence signal was recorded for that sample as the expected signal is out of the wavelength range of the OSA. The peak wavelength of the Nd$^{3+}$ fluorescence spectrum is strongly dependent on the host composition. For germanosilicate hosts, the fluorescence peak of the $^4F_{3/2} \Longrightarrow^4 I_{11/2}$ transition is situated around 1088nm. For phosphosilicate hosts, it is closer to 1054nm [35]. The glass composition used

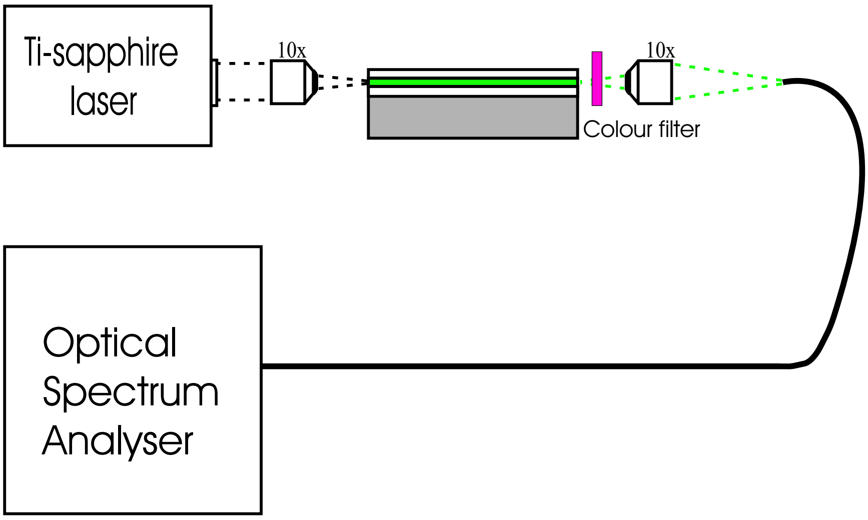

Figure 5.12: Apparatus for Fluorescence characterisation.

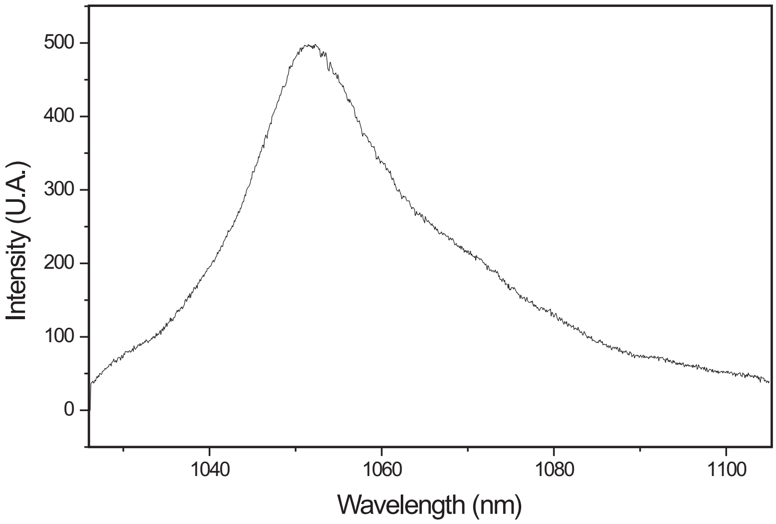

Figure 5.13: Fluorescence spectrum for neodymium ions in doped silica host.

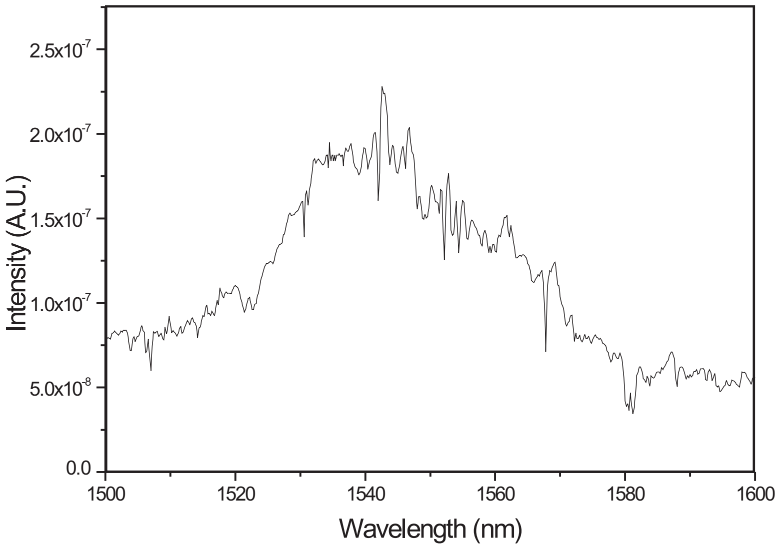

Figure 5.14: Fluorescence spectrum for erbium in doped silica host.

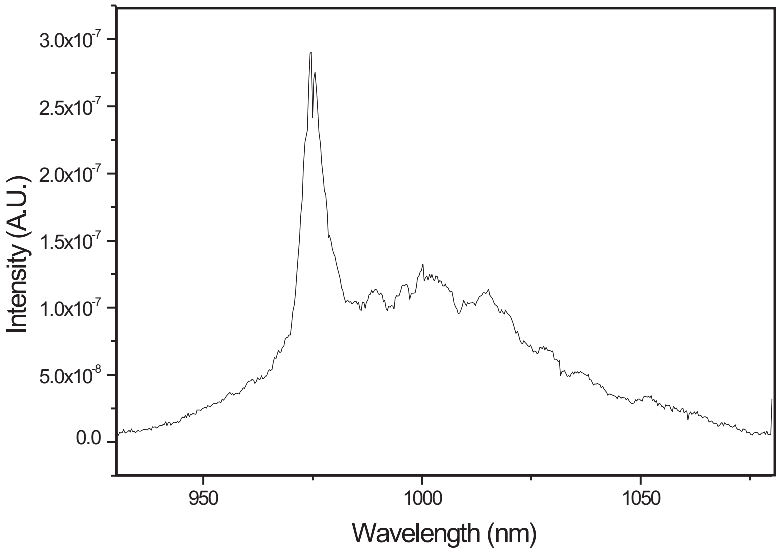

Figure 5.15: Fluorescence spectrum for ytterbium in doped silica host.

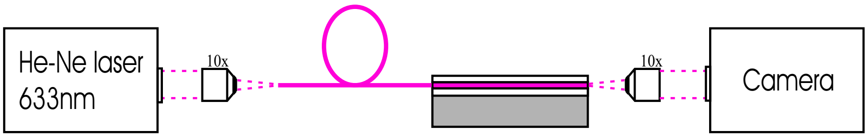

Figure 5.16: Apparatus for NA measurements.

| Dopant | Y direction | X direction |
|---|---|---|
| Nd | 0.057 | 0.15 |
| Er | 0.042 | 0.1 |
| Tm | 0.054 | 0.14 |
| Yb | 0.055 | 0.127 |
| Undoped | 0.054 | 0.141 |

Table 5.3: NA values

here can be assumed to be mainly phosphosilicate as the peak is centered around 1050nm.

### 5.6.4 Numerical aperture

The numerical aperture is the expression of the angular acceptance cone for launched light into the waveguide. This is defined by the conical half angle for which launched light is below the critical angle for propagation along the waveguide by internal reflection. Analysis of this data gives an idea of the strength of the waveguide i.e. the refractive index difference.

This characterisation set up is based on a HeNe laser at 632.8nm. The light from the laser is launched into an optical fibre butt-coupled to the waveguide. The light is collected from the output facet and focussed onto a CCD camera. Prior calibration of the CCD pixel size allows rapid dimensioning of the images captured. By moving the entire output signal collection equipment, in focus and out of focus images are captured and the dimensions of the spots used to calculate the NA of the channel. The results are listed in table 5.3. It is expected to have two different values for the different axis as in the x direction, the refractive index difference is primarily

Figure 5.17: Apparatus for mode profile plotting.

due to the different index of the different layers, 1.4641 for the cladding layers and 1.4818 for the core layer. In the y direction, the only refractive index difference is UV induced. Using the following equation that links the NA to the refractive index difference [36]:

$$NA = n\sqrt{2\Delta n} \tag{5.5}$$

Where n is the refractive index of the core layer. We can calculate the refractive index difference. It is approximately equal to $1 \times 10^{-3}$ for an NA value of 0.055. Another point worth noting is that values for an undoped sample and rare-earth doped samples are very similar suggesting very little change in photosensitivity due to the inclusion of rare-earth ions. This will be examined in more detail later in section 7.4.3.

### 5.6.5 Mode profiles

Mode profiles have been captured using the experimental configuration shown in figure 5.17. It uses a 1550nm laser with an output power regulator. The output beam is launched into the channel and the output beam focussed on a Spiricon mode profiler. By moving the sample slightly, the input coupling can be modified to excite separate individual modes. The results are presented in figure 5.18, 5.19 and 5.20. It can be seen that different modes can effectively be excited. Hence the waveguides produced are multimode at 1550nm, thus also at 1050nm. Once more, it can be noted that there is little difference in the behaviour exhibited by the undoped sample and the rare-earth doped samples. This suggests again that the photosensitivity is not modified significantly by the inclusion of rare-earth ions in the layer. 3 different modes can be excited in the y direction for

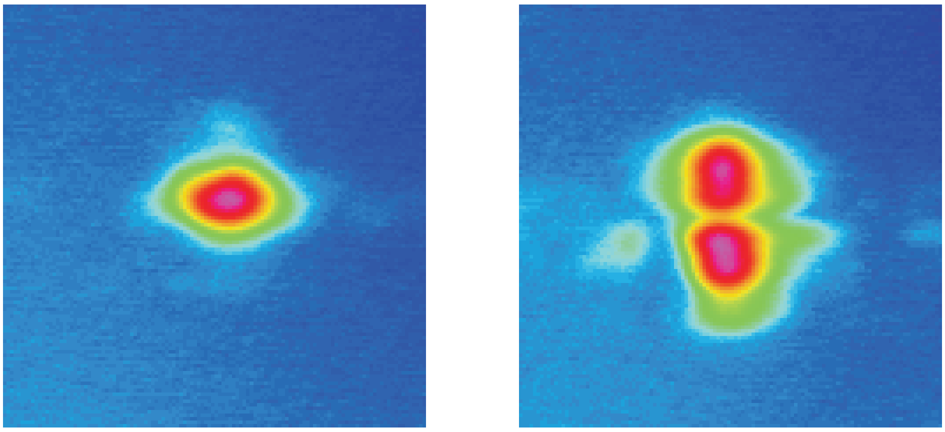

Typical fundamental mode Typical second mode

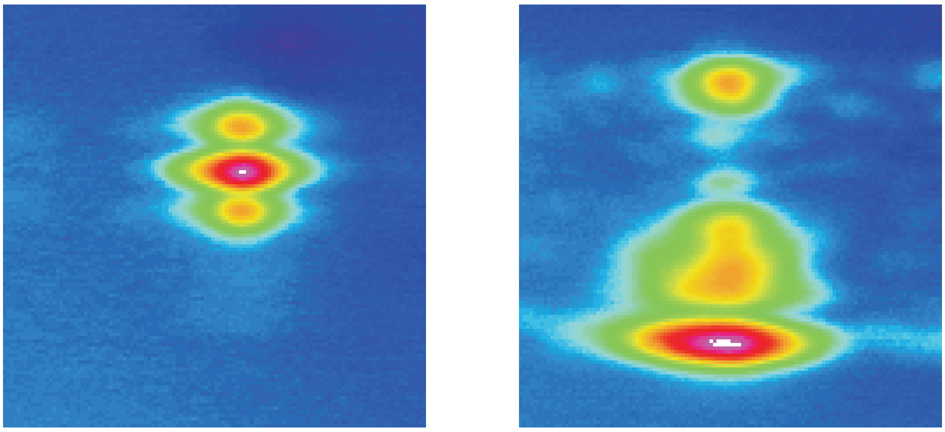

Typical third mode Mode for Nd 0.03M

Figure 5.18: 2 dimensional mode profiles.

each of the doped samples but only two for the undoped samples. This is logical as the refractive index of the undoped core layer is lower than for the doped layers (1.476). Another interesting fact is that for the sample doped with a 0.03M solution of neodymium, no waveguide is defined in the core layer (fig. 5.18). Only the two weak waveguides written in the weakly photosensitive cladding layers can be observed. This is suspected to be due to a poor sample rather than a suppression of photosensitivity due to rare-earth doping.

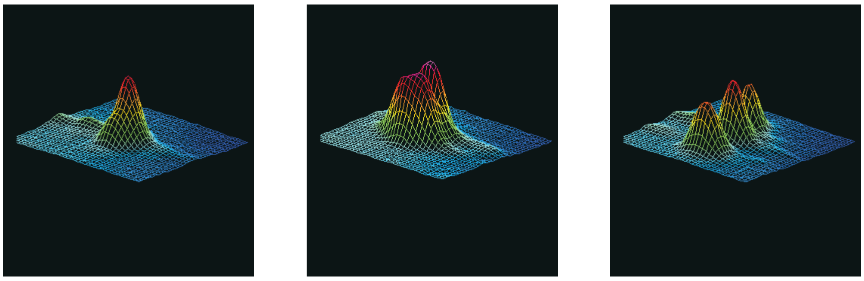

Propagating modes for Nd 0.011M sample

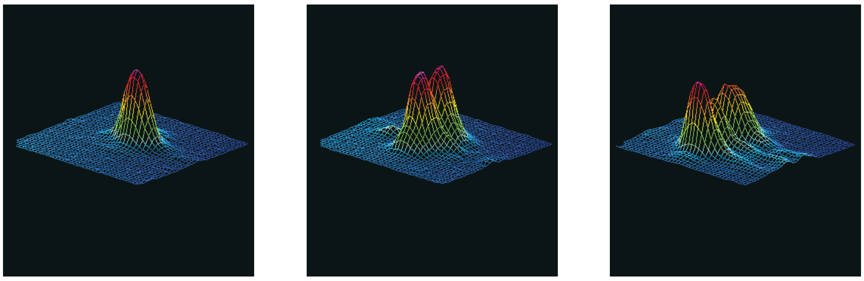

Propagating modes for Tm 0.0274M sample

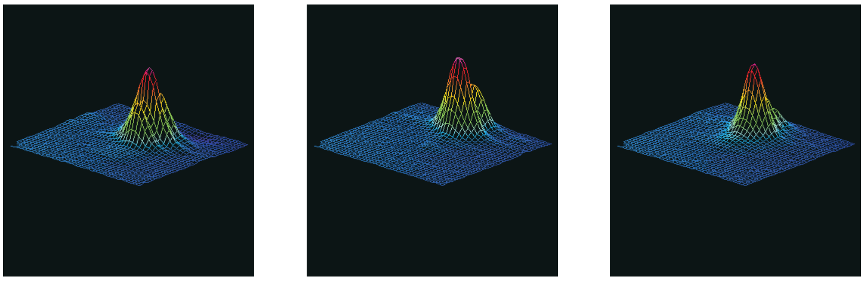

Propagating modes for Yb 0.011Msample

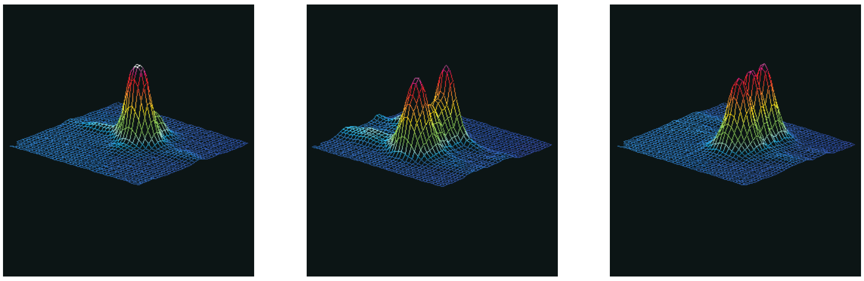

Propagating modes for Nd 0.00875Msample

Figure 5.19: 3 dimensional mode profiles.

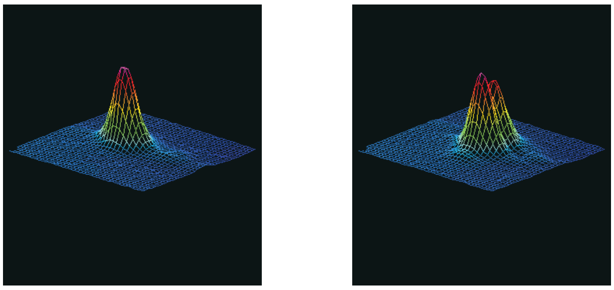

Propagating modes for undoped sample

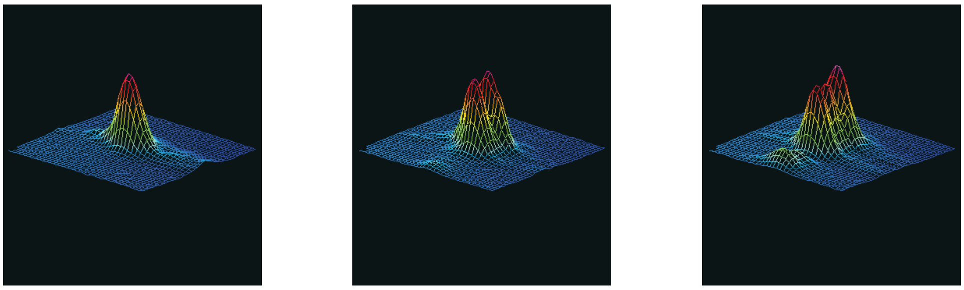

Propagating modes for Er/Al 0.031-0.31M doped sample

Figure 5.20: Other 3 dimensional mode profiles.

## 5.7 Y-splitters

In the latest stages of this work, due to the deterioration of the laser, it was difficult to obtain a stable UV writing beam for high powers which meant a power of 90mW had to be used instead of 100mW as in the experiments reported previously. Nevertheless, Y-splitters have been produced in a 13mm long Nd doped sample. The speed of the sample translation during the writing of the second arm of the splitter is greater than the speed for the first arm to create a difference in the output power proportion in the first and second arm [5]. The fabrication of such 2D structures indicates that the production of more complicated structures are possible. For instance, if a DFB laser can be produced with gratings as couplers, a series of DFB lasers with different output wavelengths could be produced with a number of Y-splitters used to excite simultaneously a number of lasers from a unique pump signal, thus providing a simple laser waveguide array.

Two Y-splitters have been created with different ratios between each arm's UV-writing speed. The first one was written with a speed of 10mm/min for the first arm and 1.5 times that value for the second arm, the second with a speed of 10mm/min for the first arm and 1.25 times that value for the second arm. A power meter was used to measure the output power coming out of each arm. For the first Y-splitter it was observed that 65% of the launched power came out of the first arm and 35% out of the second arm. For the second, it was closer to 75% of the power out of the first arm and 25% out of the second arm. This shows that by modifying the UV-writing speed difference between the two arms, a 50-50 Y-splitter could very likely be produced.

## 5.8 Summary

Two waveguide definition techniques, namely photolithography followed by reactive ion etching and direct UV writing, have been described and the respective advantages listed. The former was developed for the semiconductor technology and was then transferred to optical waveguide fabrication. It is a multi-step process that allows mass production but is very costly and time-consuming when design and prototyping of devices is the main aim. Direct UV writing allows this as it is a single step process but due to the serial nature of the process, it is a less mass-production friendly technique. The theory behind photosensitivity and deuterium loading has also been described. The system used for channel waveguide definition has then been reviewed and the compositions of the layers used during the course of this work described.

Following this, the results obtained from characterisation experiments on the UV-defined channel waveguides have been listed, starting with the spectroscopy. The absorption, fluorescence lifetime and fluorescence spectrum have been given for each ion except for the fluorescence of thulium which was not detected during the experiment. The characteristics of the channel waveguides were then analysed with numerical aperture and mode profiles being measured. Finally, the fabrication of Y-splitters, paving the way to more complex waveguiding structures and devices, has been reported.

## 5.9 References

[1] G.D. Emmerson. Novel direct UV written devices. *PhD thesis, University of Southampton*, 2003.

[2] S.P. Watts. Flame Hydrolysis Deposition of photosensitive silicate layers suitable for the definition of waveguiding structure through direct ultraviolet writing. *PhD thesis, University of Southampton*, 2002.

[3] M. Kawachi. Silica waveguides on silicon and their application to integrated-optic components. *Optical and Quantum Electronics*, 22 : p391–416, 1990.

[4] J.R. Bonar. Waveguide lasers in rare-earth doped planar silica. *PhD thesis, University of Glasgow*, 1995.

[5] M. Svalgaard. Ultraviolet light induced refractive index structures in germanosilica. *PhD thesis, Technical University of Denmark*, 1997.

[6] V. Mizrahi, P.J. Lemaire, T. Erdogan, W.A. Reed, D.J. DiGiovanni and R.M. Atkins. Ultraviolet laser fabrication of ultrastrong optical fiber gratings and of germania-doped channel waveguides. *Applied Physics Letters*, 63(13) : p1727–1729, 1993.

[7] G.D. Maxwell and B.J. Ainslie. Demonstration of a directly written directional coupler using UV-induced photosensitivity in a planar silica waveguide. *Electronics Letters*, 31(2) : p95–96, 1995.

[8] M. Svalgaard, C.V. Poulsen, A. Bjarklev and O. Poulsen. Direct UV writing of buried singlemode channel waveguides in Ge-doped silica films. *Electronics Letters*, 30(17) : p1401–1403, 1994.

[9] D. Zauner, K. Kulstad, J. Rathje and M. Svalgaard. Directly UV-written silica-on-Silicon planar waveguides with low insertion loss. *Electronics Letters*, 34(16) : p1582–1584, 1998.

[10] K. Faerch and M. Svalgaard. Symmetrical waveguide devices fabricated by direct UV writing. *IEEE Photonics Technology Letters*, 14(2) : p173–175, 2002.

[11] C. Riziotis. Advanced Bragg grating based integrated optical devices for wavelength division multiplexing systems. *PhD thesis, University of Southampton*, 2001.

[12] H.G. Limberger, P.Y. Fonjallaz, R.P. Salathe and F. Cochet. Compaction and photoelastic-induced index changes in fiber Bragg gratings. *Applied Physics Letters*, 68(22) : P3069–3071, 1996.

[13] Y. Hibino, M. Abe, H. Yamada, Y. Ohmori, F. Bilodeau, B. Malo and K.O. Hill. Increase in photosensitivity in silica-based optical waveguides on silicon. *Electronics Letters*, 29(7) : p621–623, 1993.

[14] P.J. Lemaire. Reliability of optical fibers exposed to hydrogen: prediction of long-term loss increase. *Optical Engineering*, 30(6) : p780–788, 1991.

[15] K.O. Hill, Y. Fujii, D.C. Johnson and B.S. Kawasaki. Photosensitivity in optical fiber waveguides: Application to reflection filter fabrication. *Applied Physics Letters*, 32(10) : p647–649, 1978.

[16] V.M. Marchenko. Photoinduced transformation of oxygen-deficient centers in silica and germanosilicate glasses. *Glass Physics and Chemistry*, 21(4) : p263–272, 1995.

[17] V.B. Sulimov, V.O. Sokolov and B. Poumellec. Cluster modelling of the Oxygen Vacancy in the $SiO_2$-$GeO_2$ system. *Phys. Stat. Sol (b)*, 196 : p175–192, 1996.

[18] A. Othonos and K. Kalli. Fiber Bragg gratings: Fundamentals and applications in telecommunications and sensing. *Artech house, Inc.*, 1999.

[19] R. Kashyap. Fiber Bragg gratings. *Academic press*, 1999.

[20] M. Douay, W.X. Xie, T. Taunay, P. Bernage, P. Niay, P. Cordier, B. Poumellec, L. Dong, J.F. Bayon, H. Poignant and E. Delevaque. Densification involved in the UV-based photosensitivity of silica glasses and optical fibers. *Journal of Lightwave Technology*, 15(8) : p1329–1342, 1997.

[21] B. Malo, J. Albert, K.O. Hill, F. Bilodeau and D.C. Johnson. Effective index drift from molecular hydrogen diffusion in hydrogen-loaded optical fibres and its effect on Bragg grating fabrication. *Electronics Letters*, 30(5) : p442–444, 1994.

[22] A. Iino, M. Kuwabara and K. Kokura. Mechanisms of hydrogen-induced losses in silica-based optical fibers. *Journal of Lightwave Technology*, 8(11) : p1675–1679, 1990.

[23] R.M. Atkins, P.J. Lemaire, T. Erdogan and V. Mizrahi. Mechanisms of enhanced UV photosensitivity via hydrogen loading in germanosilicate glasses. *Electronics Letters*, 29(14) : p1234–1235, 1993.

[24] J.F. Shackelford, P.L. Studt and R.M. Fulrath. Solubility of gases in glass II. He, Ne, and $H_2$ in fused silica. *Journal of Applied Physics*, 43(4) : p1619–1626, 1972.

[25] J. Stone. Interactions of hydrogen and deuterium with silica optical fibres: A review. *Journal of Lightwave Technology*, LT-5(5) : p712–733, 1987.

[26] R.W. Lee, R.C. Frank and D.E. Swets. Diffusion of hydrogen and deuterium in fused quartz. *Journal of Chemical Physics*, 36(4) : p1062–1071, 1962.

[27] G.D. Emmerson, S.P. Watts, C.B.E. Gawith, V. Albanis, M. Ibsen, R.B. Williams and P.G.R. Smith. Fabrication of directly UV-written channel waveguides with simultaneously defined integral Bragg gratings. *Electronics Letters*, 38(24) : p1531–1532, 2002.

[28] J.E. Townsend. The development of optical fibres doped with rare-earth ions. *PhD thesis, University of Southampton*, 1990.

[29] K. Hattori, T. Kitagawa, Y. Ohmori and M. Kobayashi. Laser-diode pumping of waveguide laser based on Nd-doped silica planar lightwave circuit. *IEEE Photonics Technology Letters*, 3(10) : p882–884, 1991.

[30] B.J. Ainslie. A review of the fabrication and properties of erbium-doped fibers for optical amplifiers. *Journal of Lightwave Technology*, 9(2) : p220–227, 1991.

[31] X. Orignac, D. Barbier, X.M. Du, R.M. Almeida, O. McCarthy and E. Yeatman. Sol-gel silica/titania-on-silicon Er/Yb-doped waveguides for optical amplification at 1.5$\mu m$. *Optical Materials*, 12 : p1–18, 1999.

[32] J.R. Bonar, M.V.D. Vermelho, A.J. McLaughlin, P.V.S. Marques, J.S. Aitchison, J.F Martins-Filho, A.G. Bezerra-Jr, A.S.L. Gomes and C.B. de Araujo. Blue light emission in thulium doped silica-on-silicon waveguides. *Optics Communications*, 141 : p137–140, 1997.

[33] H.M. Pask, R.J. Carman, D.C. Hanna, A.C. Tropper, C.J. Mackechnie, P.R. Barber and J.M. Dawes. Ytterbium-doped silica fiber lasers: versatile sources for the 1-1.2 $\mu m$ region. *IEEE Journal of Selected Topics in Quantum Electronics*, 1(1) : p2–13, 1995.

[34] B. Schaudel, P. Goldner, M. Prassas and F. Auzel. Cooperative luminescence as a probe of clustering in $Yb^{3+}$ doped glass. *Journal of Alloys and Compounds*, 300-301 : p443–449, 2000.

[35] M.J.F. Digonnet. Rare-earth doped fiber lasers and amplifiers. *Marcel Dekker, Inc.*, 2001.

[36] A. Ghatak and K. Thyagarajan. Introduction to fiber optics. *Cambridge University Press*, 1998.

# Chapter 6

# External cavity lasers

## 6.1 Introduction

In this chapter, we report the first demonstration of an all-UV-written waveguide laser in silica-on-silicon. In the previous chapter, the fabrication of uniform channel waveguides in rare-earth doped silica-on-silicon has been outlined and the spectroscopic proprieties of the rare-earth doped substrate have been analysed. This chapter discusses the laser characterisation of these structures. Lasing was not observed in the erbium, thulium or ytterbium channels. It seems likely that the doping level in these samples is insufficiently high to allow lasing to occur, or that the losses of the waveguides are too high, as previous work has reported lasing in these materials for higher doping levels [1], fibre geometry [2] or alternative fabrication methods [3]. In the neodymium doped material, lasing has been observed for different lengths, substrate types and at different wavelengths. The results are described and examined in section 6.3.

## 6.2 Review

Since direct-UV-writing has been proven to be a quick and simple technique for the fabrication of low-loss waveguide channels [4], some research has been focussed on UV-writing of channels in rare-earth doped materials [5] although to the best of the author's knowledge, no laser results have been reported by other groups. In the ORC, the first all-UV-written laser reported was fabricated in neodymium doped fluoride glass with a laser threshold of $60mW$ of absorbed power and a slope efficiency of 26% for a 56% output coupler [6]. Some success has also been achieved in chalcogenide glass with a single mode output and a reported laser threshold of $15.1mW$ of absorbed power, using two high reflectivity couplers and having a slope efficiency of 17% using a 12.5% transmission output coupler [7]. The only result reported in silica was published by Gawith et al [8], where the sample preparation involved direct bonding, ion exchange and UV writing. The laser threshold was reported to be $2.7mW$ for high reflectivity couplers and the slope efficiency 9%. The results reported below demonstrate the viability of UV-writing as a cost efficient technique for laser waveguide fabrication in silica-on-silicon, with the results being comparable or better than those reported for earlier work in neodymium doped silica-on-silicon waveguide lasers fabricated with alternative channel definition techniques [15–17].

## 6.3 Results for neodymium doped lasers

This section details the results obtained for neodymium doped UV-written channel waveguide lasers. The waveguides were written with the conditions described in section 5.6, with the exception that some have been written with $100mW$ of incident power and others with only $80mW$, giving only a negligible difference in behaviour. To carry out the characterisation, the set-up shown in figure 6.1 was used. A tunable Ti:Sapphire laser was employed to pump the lasing medium. A laser cavity is created by bonding dielectric thin film mirrors onto the end faces of the waveguides, using the surface tension of a very thin layer of fluorinated liquid for adhesion. Pump radiation was focused for launch into each buried channel waveguide by means of a $\times 10$ microscope objective which was found to give the best launch efficiency into the channel. The output sig-

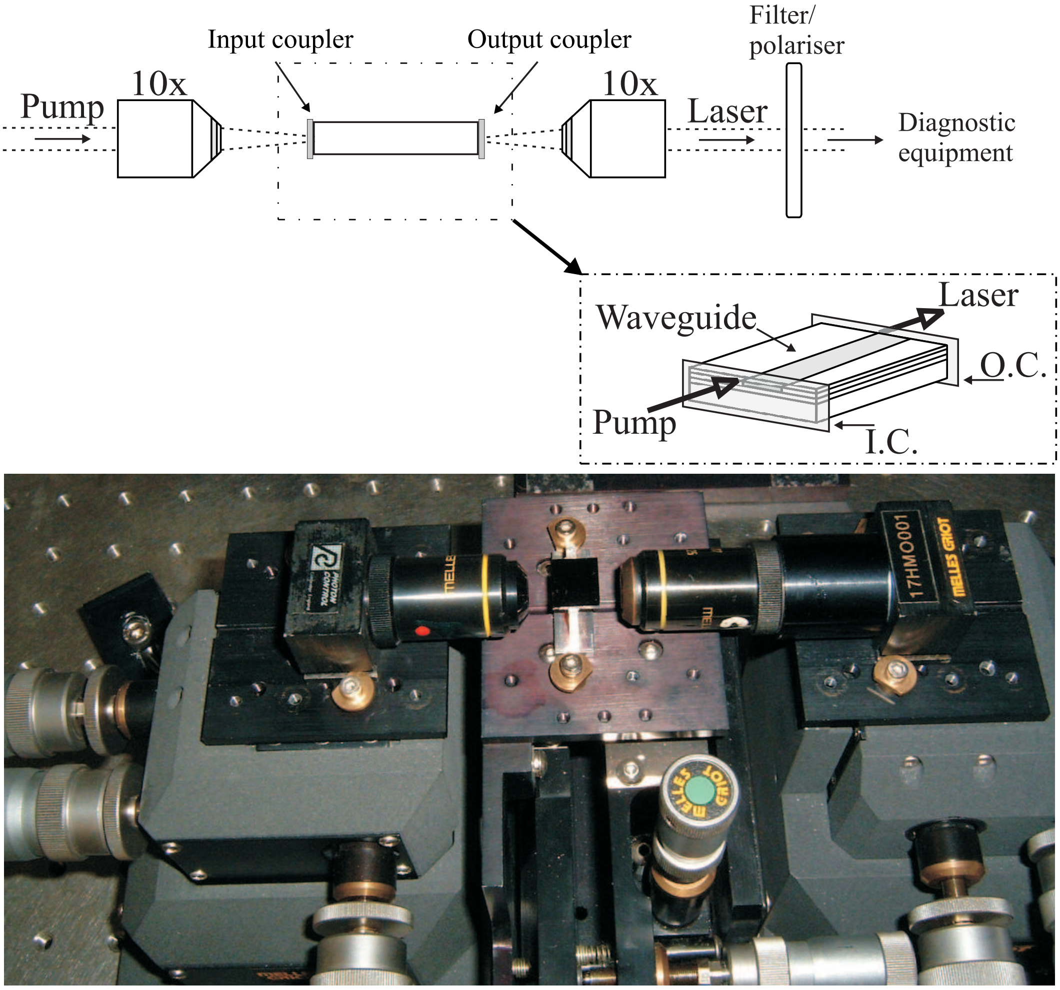

Figure 6.1: Apparatus for laser characterisation.

nal is focussed onto the diagnostic equipment via another $\times 10$ microscope objective. An RG1000 colour filter is placed in the beam path after the sample to block residual pump signal (transmittance of $< 10^{-5}$ at 808$nm$ and 68% at 1.05$\mu m$), and a polariser is also inserted in the case of laser output polarisation characterisation.

In the remainder of this chapter, the threshold powers for activation of the lasing effect are presented along with slope efficiencies. Then the lasing spectrum is detailed with explanation of the diverse phenomena observed and the output profile is described. Next, estimations of loss inside the channel are demonstrated. Finally, an interesting effect affecting the polarisation of the output of the laser is mentioned and a possible explanation given.

### 6.3.1 Threshold results and slope efficiency

After UV-writing, the sample was cut and both end faces were polished providing 18mm long waveguides. The launch efficiency was optimised in relation to the fluorescence measured by a silicon detector connected to an oscilloscope and was found to be approximately $84\%$ by tuning the pump laser wavelength out of the absorption range and measuring the intensity of the light propagated down the channel waveguide. The absorption was calculated from measurements of input and output pump power before and after the waveguide and absorption was found to be nearly $100\%$. Then the output signal was measured by a silicon detector connected to a power meter. A mask was applied to the power meter, blocking the signal potentially propagating through the slab waveguide and ensuring that only light emitted by the channel was incident on the detector. Laser action was achieved in the Nd $^4F_{3/2} \Longrightarrow ^4 I_{11/2}$ transition by pumping a selected channel waveguide at 808nm and using two highly reflecting (HR) mirrors with $> 99.9\%$ reflectivity at the lasing wavelength ($\sim 1.05 \mu m$) and a transmission of $87\%$ at the pump wavelength. A lasing threshold of 21mW absorbed power was recorded after taking the launch and absorption efficiencies into account together with the transmission of the input mirror and the launch objective. Optimisation of the output coupler was required before investigation of the lasing properties. Four output mirrors were available with transmission values ranging from 8 to 34$\%$. The threshold was investigated for each output coupler and a transmission of $25\%$ was found to be the optimum value for output power characterisation. The threshold was found to increase to 28mW of absorbed power and the slope efficiency was measured to be $24 \pm 2\%$ (Figure 6.2) using a HR input coupler and that output coupler. The maximum output was found to be approximately 160mW for about 850mW of absorbed pump power (the maximum power available from the pump laser).

After characterisation, the sample was cut into two pieces and end faces

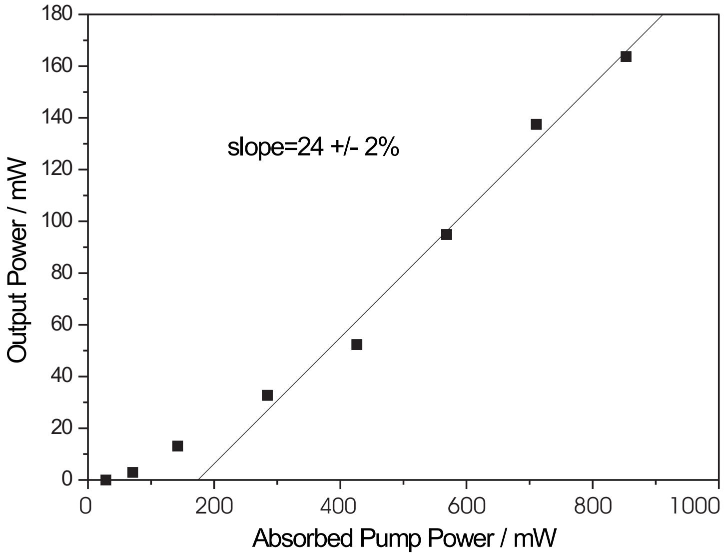

Figure 6.2: Output power versus absorbed pump power for the 18mm long sample, HR/25% transmission around 1050nm.

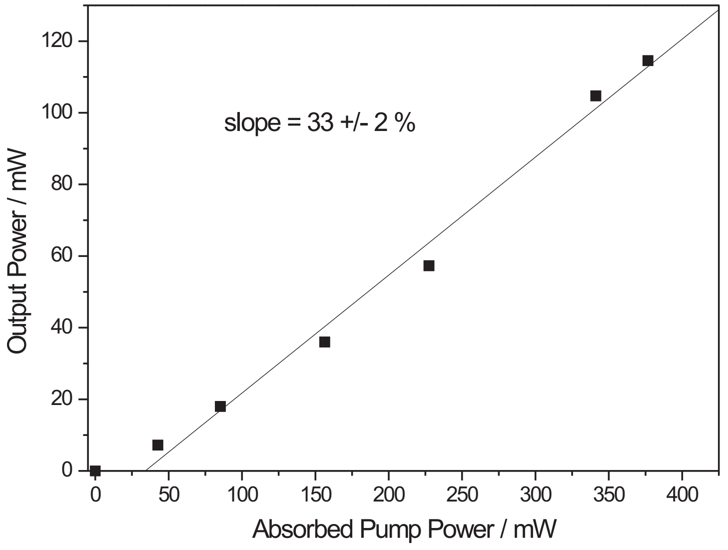

Figure 6.3: Output power versus absorbed pump power for the $10mm$ long sample, HR/25% transmission around 1050nm.

of both resulting samples were polished to provide waveguide channels of 4.5mm and 10mm. Absorption was found to be $60\%$ for the 4.5mm long waveguide and $92\%$ for the 10mm long waveguide. Thresholds of 62mW and 200mW of absorbed power were obtained for the 4.5mm waveguide using respectively two HR mirrors and an HR mirror as input coupler with an output coupler with a transmission of $25\%$. It decreased to 4mW for the 10mm long waveguide using two HR mirrors. For the same sample, a threshold of 11mW and a slope efficiency of $33 \pm 2\%$ were observed using a $25\%$ transmission output coupler (Figure 6.3) which again was found to be the optimum value for lasing properties characterisation. It should be noted that the output coupler reflected the unabsorbed pump power allowing the assumption of 100% absorption in this case.

### 6.3.2 Lasing spectra and output mode profile

The results listed in the remainder of this chapter were obtained for the 10mm long sample as the threshold and slope efficiency results were better and this was assumed to be the near optimum length for this composition. Mode profiling of the 1050$nm$ output signal from the waveguide laser was performed with a silicon camera and computer-based evaluation software. As can be seen in figure 6.6, the laser output is slightly asymmetric and single-lobed, where the single-lobe is an indication of single-mode operation. The lasing occurs in the fundamental spatial mode, with a Gaussian mode profile in both guided directions. The mode radii within the cavity were calculated using Gaussian optics and the mode widths measured on the Charge Coupled Device (CDD) camera. A guided output spot size (1/e$^2$ intensity radius) was calculated to be, in the x and y direction, 4.4$\mu m$ and 6.9 $\mu m$ respectively. Lasing was observed at wavelengths ranging between 1048 and 1056nm. As shown in figures 6.4 A and B, the laser has a single peak at threshold around 1050.3nm with a linewidth of about 0.5nm. This is the same wavelength as the maximum of the fluorescence spectra of neodymium in this material as can be seen in figure 5.13 (the resolution of the measurement is 0.05nm). If the pumping power is increased, lasing action starts happening simultaneously at 1052.5nm, then at 1048nm and finally at 1055nm. These different wavelengths are not thought to be due to different longitudinal modes as the spacing between them is quite large. The cavity mode spacing can be expressed as:

$$\Delta\lambda = \frac{\lambda^2}{2nl} \tag{6.1}$$

where $\lambda$ is the lasing wavelength, $n$ the refractive index and $l$ the length of the waveguide. At 1050nm, for a waveguide of 10mm and a refractive index of 1.4818 at 633nm, the typical mode spacing is calculated to be approximately 0.037nm. The observed spacing of the different lasing wavelengths is approximately 2.3nm. Therefore they are not due to different cavity modes but are attributed to the intra-cavity etalon effect appearing from the reflections due to the thickness of the thin mirrors used, creating different cavity lengths thus allowing lasing to occur at different wavelengths.

Laser action was also achieved in the Nd $^4F_{3/2} \Longrightarrow^4 I_{13/2}$ transition at 1356.1nm at a threshold of 370mW of absorbed power using two highly reflecting mirrors. This result is thought to be affected by ASE on the $^4F_{3/2} \Longrightarrow^4 I_{11/2}$ transition [9]. The result gives a higher threshold than expected. Again, if the pump power is increased from close to threshold to a higher value, lasing starts occurring at a second wavelength of 1352.5nm (see figure 6.5). With a cavity length of 10mm, a refractive index of 1.4818 at 633nm and a wavelength of 1356nm, the mode spacing is calculated to be 0.062nm. Once again, the second lasing wavelength is thought to be due to intra-cavity etalon effects.

### 6.3.3 Loss calculations

A number of methods are available to calculate the round trip propagation loss of a laser cavity. First of all, the slope efficiency can be related to the propagation loss by the equation [10]:

$$\eta = \frac{\lambda_P}{\lambda_L}\left(\frac{-\ln R}{-\ln R + 2\alpha l}\right)\eta_{PL}\eta_q \tag{6.2}$$

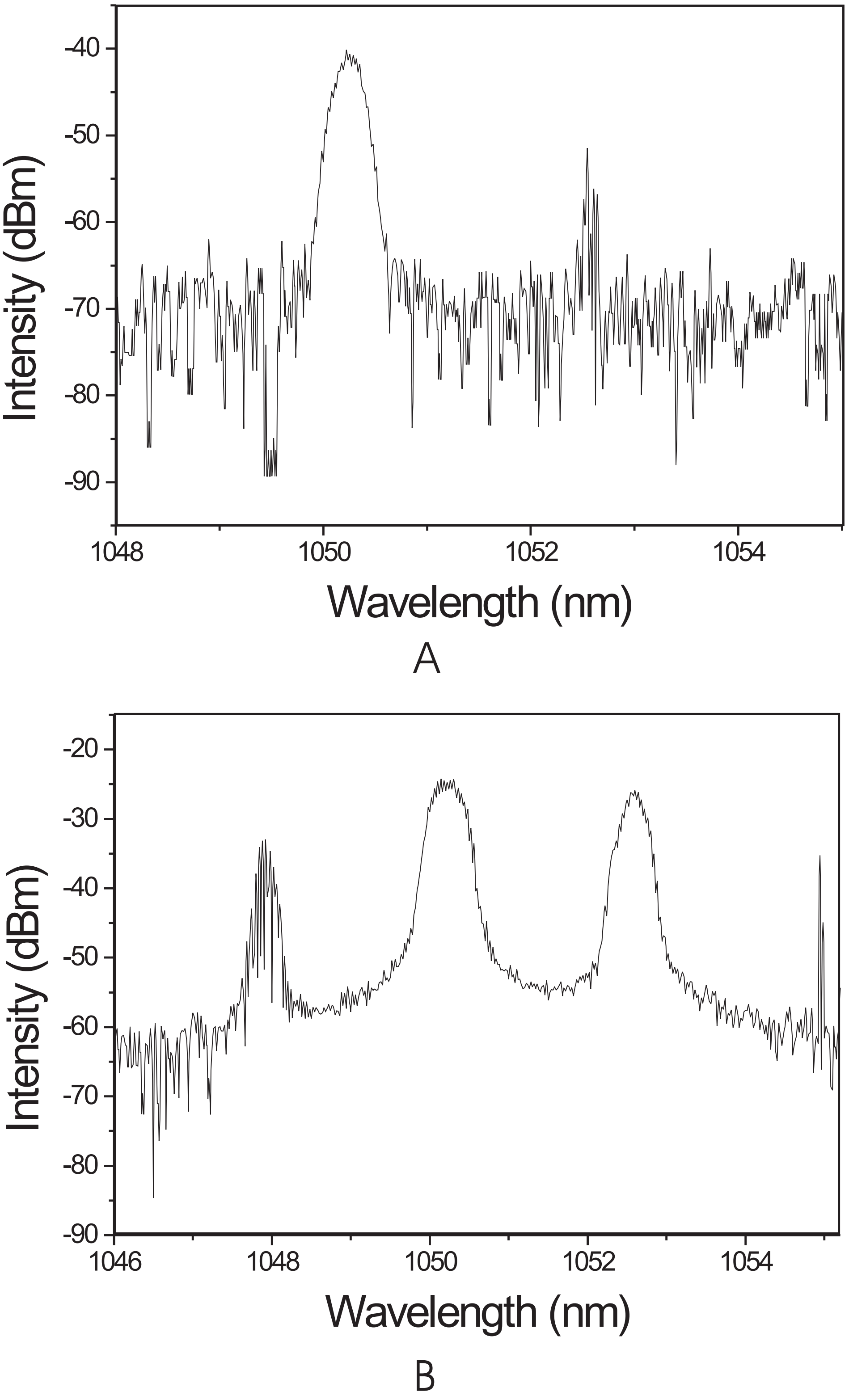

Figure 6.4: Output spectra of the laser. A : at low pumping power ( 10mW). B : at high pumping power ( 400mW).

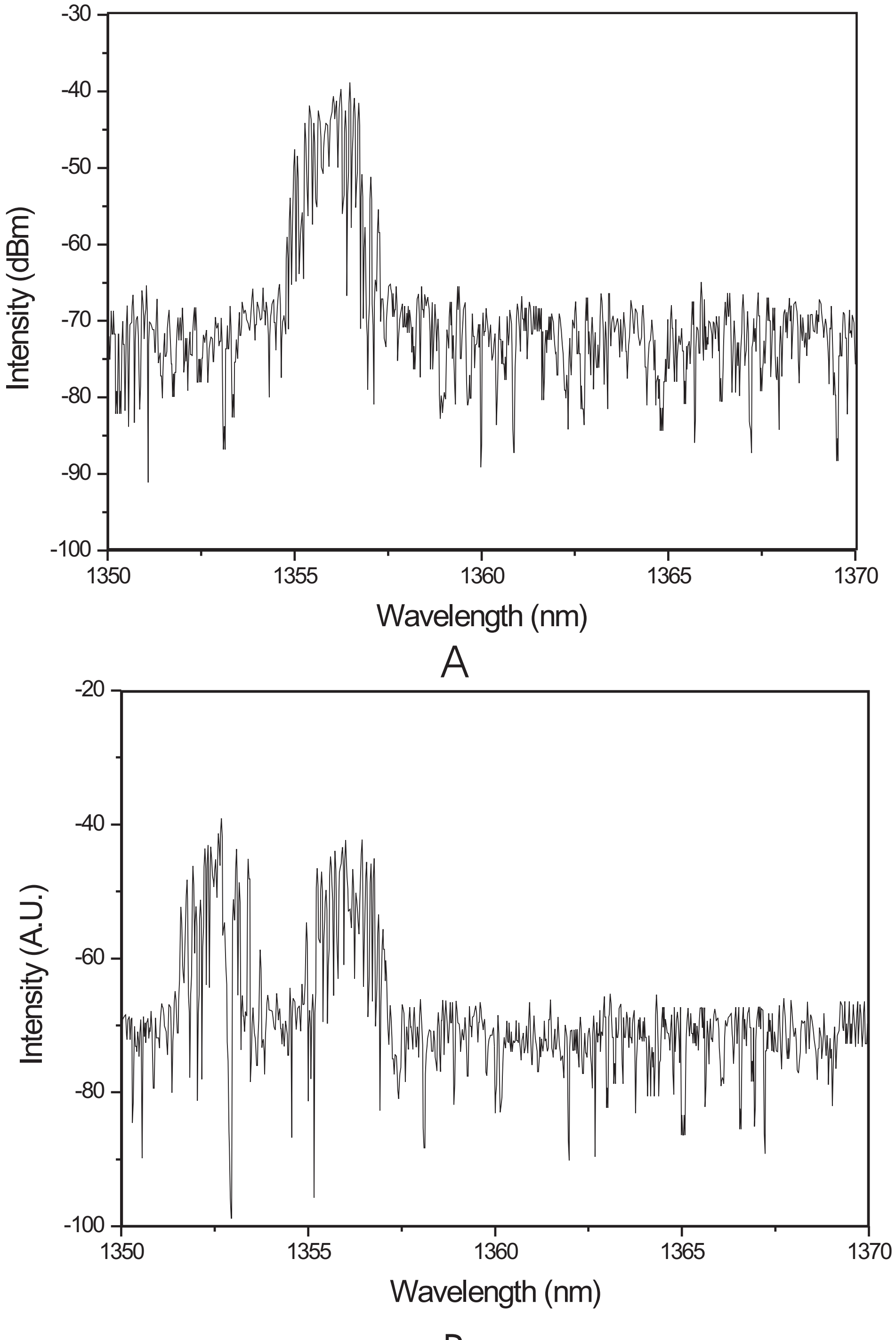

Figure 6.5: Output spectra of the laser. A : at 370mW pumping power. B : at about 600mW pumping power.

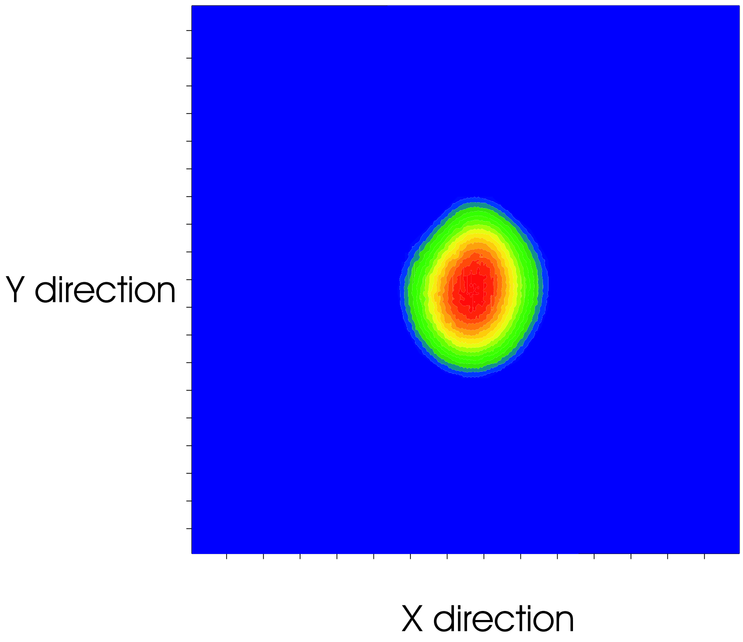

Figure 6.6: Imaged mode profile of the output of the waveguide laser.

Where $\lambda_P$ is the pump wavelength, $\lambda_L$ is the laser wavelength, $R$ is the reflectivity of the output coupler and $2\alpha l$ is the remaining round trip loss, which is assumed to be dominated by the propagation loss ($2\alpha_p l$). A 100% spatial overlap between the pump and laser modes ($\eta_{PL} = 1$) and a 100% quantum efficiency ($\eta_q = 1$) where all neodymium ions excited into a higher energy level state will participate in laser action, are assumed, leading to an upper estimate of propagation loss.

The round trip propagation loss coefficient in $dBcm^{-1}$ is performed using the value of $2\alpha l$ from equation 6.2 with:

$$\alpha_p = \frac{-10\log(e^{-2\alpha l})}{2l} \tag{6.3}$$

Where $l$ is the cavity length in $cm$. An absolute upper value for the propagation loss of $0.8dBcm^{-1}$ was calculated, as the overlap is not actually $100\%$.

Another possible derivation of the loss value uses the threshold power equation. Using equation 2.42 and assuming that there is zero re-absorption loss, a 100% quantum efficiency ($\eta_p = 1$) and the overlap of pump and signal is almost equal to 1 [11]:

$$P_{th} = \frac{\pi hc}{4\sigma_m \tau \lambda_P}\left(2\alpha l - \ln R\right) 2W_x W_y \tag{6.4}$$

Where $h$ is Planck's constant, $c$ is the speed of light, $\sigma_m$ is the measured stimulated emission cross-section ($1.9 \times 10^{-24} m^2$ [13]) where $\sigma_m = \frac{\sigma}{f}$, $\tau$ is the upper laser level lifetime, $\lambda_P$ is the pump wavelength, $R$ is the mirror reflectivity, $W_x$ is the pump and laser mode radius in the x-direction (assumed to be the same) and $W_y$ is similarly the pump and laser mode radius in the y-direction. $2\alpha l$ is the round-trip propagation loss as in equation 6.2 for which the general notation $L$ was used in 2.42. The transmission loss $T$ is equal to $-lnR$ for small values. Using the values of the laser mode radii given in section 6.3.2 and the absorbed threshold power of $4mW$, measured for this waveguide using two HR mirrors, the propagation loss value becomes $0.3dBcm^{-1}$.

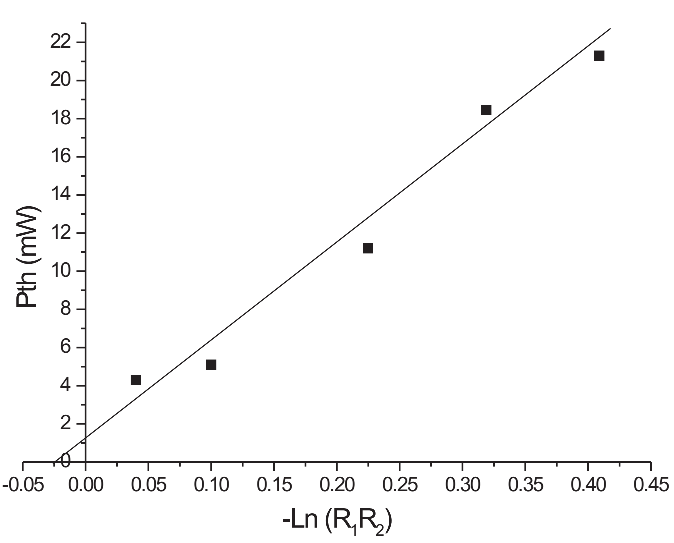

Figure 6.7: Dependence of laser threshold power on output coupling where the intercept with the x axis gives the waveguide propagation attenuation coefficient.

Another method is the Findlay-Clay loss measurement that investigates the correlation between laser threshold and output coupling [12]. If the lower laser level population is assumed to be negligible and the loss and laser mode size constant, the threshold of the laser can be expressed as:

$$P_{th} = k[2\alpha l - \ln(R_1 R_2)] \tag{6.5}$$

where k is a constant taking into account the material parameters and the pump and signal spatial properties, $l$ is the length of the laser cavity, $\alpha$ is the propagation loss coefficient and $R_1$ and $R_2$ are the mirrors reflectivity at the laser wavelength. By changing the output coupler, a plot of threshold versus -ln($R_1 R_2$) is produced (Figure 6.7) where the intersection of the slope with the x axis gives an estimate of the propagation loss coefficient at 1050nm, in this case $\alpha \sim 0.0125 cm^{-1}$. The propagation loss can be deduced from this value using equation 6.3.

The loss is calculated to be approximately $0.11 dBcm^{-1}$. The waveguide definitely has relatively low loss as lasing action occurs. Results from these three calculations and comparison of the waveguide output with previous work by Sam Watts [14] on loss measurements of UV-written waveguides leads us to believe that our losses are between 0.11 and 0.3dB/cm.

### 6.3.4 Polarization of the laser output

The polarisation of the output laser beam was measured using a polarising cube. The output at 1050nm was observed to be strongly horizontally polarised. On the other hand, the output around 1350nm was found to be strongly vertically polarised. A definite explanation for this phenomenon has not been uncovered and no mention of a similar effect has been found in the literature. Nevertheless, the change in polarisation between these two transitions is thought to be due to a difference in scattering at these two wavelengths. From previous work, the waveguide was found to be lossier around 1300nm than around 1050nm [14]. It is possible that the scattering could stop the horizontal mode from lasing at 1350nm making the vertically polarised mode lower loss and hence favouring its lasing. Another plausible explanation is that this effect is due to heating of the sample, the pump power necessary for lasing at 1356nm being so much higher than at 1050nm.

## 6.4 Summary

The beginning of this chapter reviews previous work that has been done on all-UV-written waveguide lasers. It has been mentioned that all previous UV-written lasers have been produced in non silica-on-silicon glasses. The main advantages of the laser reported here is that it is made in planar silica-on-silicon therefore having the inherent advantages of using this material. Also, the performance of this laser has been proved to be better than the performances of the lasers made in fluoride or chalcogenide glasses [6,7]. A laser has been previously produced in neodymium-doped silica by direct-bonding and ion exchange [8] at a depth of 200$\mu m$. Nevertheless, the fabrication process of the laser reported here is much simpler making it a more cost effective method for the production of waveguide lasers. Also, the waveguide is only 16$\mu m$ under the surface making the integration of UV-written Bragg gratings much more feasible. Results on this aspect are reported in the next chapter. The properties of what is, to the best of the author's knowledge, the first all-UV-written laser in silica-on-silicon were then reported including lasing threshold power, slope efficiency, output mode profile, output spectrum and polarisation considerations. The results were found to be an improvement on the proprieties of neodymium doped silica-on-silicon waveguide lasers made by other methods [15–17]. The lasing threshold and slope efficiency results were used to estimate the propagation loss of the cavity, along with the Findlay-Clay analysis, and gave a limit of 0.8dBcm$^{-1}$ and an estimate of 0.11 to 0.3dBcm$^{-1}$ .

Two interesting effects had to be noted, firstly the appearance of lasing signals at different powers in the presence of high pumping power which are attributed to intra-cavity etalon effects and secondly, a change in the polarisation of the output between the two transitions for which lasing occurs, which was attributed to a difference in scattering loss of the channel at these two different wavelengths.

## 6.5 References

[1] C. Florea and K.A. Winick. Ytterbium-doped glass waveguide laser fabricated by ion exchange. *Journal of Lightwave Technology*, 17(9) : p1593–1601, 1999.

[2] D.C. Hanna, I.R. Perry, J.R. Lincoln and J.E. Townsend. A 1-Watt thulium-doped cw fibre laser operating at 2$\mu m$. *Optics Communications*, 80(1) : p52–56, 1990.

[3] T. Kitagawa, K. Hattori, M. Shimizu, Y. Ohmori and M. Kobayashi. Guided-wave laser based on erbium-doped silica planar lightwave circuit. *Electronics Letters*, 27(4) : p334–335, 1991.

[4] M. Svalgaard and M. Kristensen. Directly UV written silica-on-silicon planar waveguides with low loss. *Electronics Letters*, 33(10) : p861–863, 1997.

[5] M. Svalgaard. Ultraviolet light induced refractive index structures in germanosilica. *PhD thesis, Technical University of Denmark*, 1997.

[6] D. Harwood, A. Fu, E.R. Taylor, R.C. Moore, Y.D. West and D.N. Payne. A 1317nm neodymium doped fluoride glass waveguide laser. *ECOC2000, Munich*, 4-7 Sept, vol. 2 : p191–192, 2000.

[7] A.K. Mairaj, A.M. Chardon, D.P. Shepherd and D.W. Hewak. Laser performance and spectroscopic analysis of optically written channel waveguides in neodymium-doped gallium lanthanum sulphide glass. *IEEE Journal of Selected Topics in Quantum Electronics*, 8(6) : p1381–1387, 2002.

[8] C.B.E. Gawith, A. Fu, T. Bhutta, P. Hua, D.P. Shepherd, E.R. Taylor, P.G.R. Smith, D. Milanese and M. Ferraris. Direct-UV-written buried channel waveguide lasers in direct-bonded intersubstrate ion-exchanged neodymium-doped germano-borosilicate glass. *Applied Physics Letters*, 81(19) : p3522–3524, 2002.

[9] F. Hakimi, H. Po, R. Tumminelli, B.C. McCollum, L. Zenteno, N.M. Cho and E. Snitzer. Glass fiber laser at 1.36$\mu m$ from $SiO_2$:Nd. *Optics Letters*, 14(19) : p1060–1061, 1989.

[10] K. Kubodera and K. Otsuka. Single-transverse-mode $LiNdP_4O_12$ slab waveguide laser. *Journal of Applied Physics*, 50(2) : p653–659, 1979.

[11] W.A. Clarkson and D.C. Hanna. Effects of transverse-mode profile on slope efficiency and relaxation oscillations in a longitudinally-pumped laser. *Journal of Modern Optics*, 36(4) : p483–498, 1989.

[12] D. Findlay and R.A. Clay. The measurement of internal losses in 4-level lasers. *Physics Letters*, 20(3) : p277–278, 1966.

[13] M.J.F. Digonnet. Rare-earth doped fiber lasers and amplifiers. *Marcel Dekker, Inc.*, 2001.

[14] S.P. Watts. Flame Hydrolysis Deposition of photosensitive silicate layers suitable for the definition of waveguiding structure through direct ultraviolet writing. *PhD thesis, University of Southampton*, 2002.

[15] Y. Hibino, T. Kitagawa, M. Shimizu, F. Hanawa and A. Sugita. Neodymium-doped silica optical waveguide laser on silicon substrate. *IEEE Photonics Technology Letters*, 1(11) : p349–350, 1989.

[16] J.R. Bonar, J.A. Bebbington, J.S. Aitchison, G.D. Maxwell and B.J. Ainslie. Low threshold Nd doped silica planar waveguide laser. *Electronics Letters*, 30(3) : p229–230, 1994.

[17] T. Kitagawa, K. Hattori, Y. Hibino and Y. Ohmori. Neodymium-doped silica based planar waveguide lasers. *Journal of Lightwave Technology*, 12(3) : p436–442, 1994.

# Chapter 7

# Bragg gratings

## 7.1 Introduction

A Bragg grating consists of a short periodic variation of the refractive index of a waveguide. The light of an incident mode is reflected (i.e. coupled into a counter-propagating mode) by such a device. The ability to create such refractive index perturbation has facilitated the development of devices such as filters or reflectors in a highly efficient, low loss manner [1] and can also be used to produce narrow-linewidth lasers (DFB). The first laser-written in-fibre grating was reported by Hill et al. in 1978 [2]. Intense light at 488$nm$ was launched into a one meter long germanium-doped silica fibre. A decrease in the transmission of the fibre was observed as a function of time along with an increase of the intensity of the light back-reflected from the fibre. It was found that the incident signal was reflected off the end of the fibre, producing a standing wave pattern. The refractive index of the Ge-doped core was increased permanently at the high intensity points. This was labelled a *self-induced* grating as it formed from the reflection due to the end face of the fibre. The main draw-back of this method was that the period of the grating was determined by the writing wavelength [3]. It was later determined that the process responsible for this refractive index perturbation was a two-photon bleaching phenomenon occurring at 244$nm$ [4,5].

The major development happened in 1989, when Meltz et al. reported the first UV-written grating using single-photon absorption at $244nm$ through side-exposure [6]. Using the interference pattern produced by two interfering beams of coherent light to illuminate the side of a fibre, they produced a reflection grating in the visible part of the spectrum. The interference pattern period was defined by the intersection angle, allowing alteration of the periodicity of the gratings using a single laser wavelength.

The first fibre laser operating from the reflection of a UV-written in-fibre grating was reported in 1990 [7] and this lased at about $1537nm$. It opened the way for a number of grating-based lasers including distributed Bragg-reflector (DBR) lasers [8–10]. Distributed feedback (DFB) lasers, common in semiconductor technology, were developed in optical fibres from 1994 [11, 12]. The cavity consists of a grating inscribed in an active medium, with a $\pi/2$ phase shift. These lasers exhibit single-frequency lasing and a very narrow linewidth with a better stability and stronger side-mode suppression than DBR lasers [13]. DFB lasers were then developed in glass planar geometry [14–16] as they are very useful for WDM technology [17, 18].

In this chapter, the basics of the theory behind Bragg reflectors will be described and the fabrication techniques for UV-written gratings in planar geometry will be reviewed. Then the results obtained during the course of this work will be described. First, the reflection and transmission spectra of gratings written in rare-earth doped layers will be given before being compared to undoped samples results. Then the modelling of the number of modes propagating through our waveguiding structures will be detailed. Finally, the dispersion of our neodymium doped waveguides will be investigated. For more insight on Bragg gratings, the reader is directed towards Othonos and Kalli [1] and Kashyap [3].

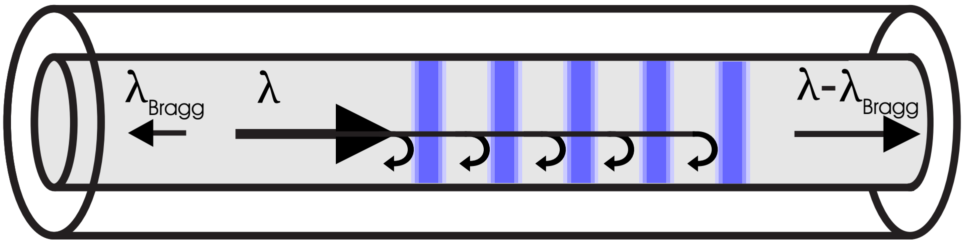

Figure 7.1: Schematic of coupling in a counter-propagating mode by a grating

## 7.2 Basics of Bragg grating theory

In this section, the definition of a Bragg grating is given along with the Bragg condition, followed by the coupled-mode approximation. It provides a good model for the wavelength response of gratings, leading to parameters expression that will be used further in this chapter.

### 7.2.1 The Bragg condition

A Bragg grating is a short-period refractive index perturbation. In such a structure, the power can be coupled between two counter-propagating modes. If an incident guided wave has a wavelength equal to the Bragg wavelength, i.e. the free space centre wavelength that will be reflected from the Bragg grating, each grating plane scatters some of the light that will add constructively in the backward direction to form a back-reflected wave with a wavevector opposite to the one of the incident wave.

The peak wavelength and bandwidth of this wave is defined by the grating parameters. The laws of energy and momentum conservation have to be respected. Hence the two counter-propagating modes will have the same frequency and the reflected wave wavevector must be equal to the incident wave wavevector coupled with the wavevector in the structure i.e. [1]:

$$k_i + K = k_r \tag{7.1}$$

Where $k_i$ is the incident wave wavevector, $k_r$ is the reflected wave wavevector and $K$ is the wavevector of the grating section so it has a direction normal to the grating planes and a magnitude of $2\pi/\Lambda$ where $\Lambda$ is the grating period. The incident and reflected wave wavevectors have the same magnitude but are opposite in direction. Hence, equation 7.1 becomes:

$$2\left(\frac{2\pi n_{eff}}{\lambda_B}\right) = \frac{2\pi}{\Lambda} \tag{7.2}$$

Where $\lambda_B$ is the Bragg wavelength and $n_{eff}$ the effective refractive index at the Bragg wavelength. This simplifies to the well-known Bragg condition:

$$\lambda_B = 2n_{eff}\Lambda \tag{7.3}$$

### 7.2.2 The coupled-mode analysis

If the Bragg grating is assumed to be uniform, the refractive index profile of such a structure in the z-direction can be expressed as follows [1]:

$$n(z) = n_0 + \Delta n \cos\left(\frac{2\pi z}{\Lambda}\right) \tag{7.4}$$

Where $n_0$ is the average refractive index and $\Lambda$ is the period of the Bragg grating. Using the coupled-mode theory it has been showed that [5]:

$$R(\lambda, L) = \frac{\kappa^2 \sinh^2(sL)}{\Delta k^2 \sinh^2(sL) + s^2 \cosh^2(sL)} \tag{7.5}$$

Where $R(\lambda, L)$ is the reflectance as a function of wavelength and grating length $L$, $\kappa$ is the coupling coefficient, $\Delta k$ is the detuning wavevector, equal to $k - (\pi/\Lambda)$, $k$ is the propagation constant, which is equal to $2\pi n_0/\lambda$ and s is the factor:

$$s = \sqrt{\kappa^2 - k^2} \tag{7.6}$$

For sinusoidal variation of the index perturbation, the coupling coefficient can be expressed as:

$$\kappa = \frac{\pi \Delta n}{\lambda} I \tag{7.7}$$

Where $I$ is the fraction of the mode contained in the core. At the Bragg grating wavelength, $\Delta k = 0$ so the expression 7.5 for the reflectivity of the grating becomes:

$$R(\lambda, L) = \tanh^2(\kappa L) \tag{7.8}$$

The bandwidth of the reflected signal can be expressed as:

$$\Delta\lambda = \lambda \frac{\Delta n_{eff}}{n_{eff}} \sqrt{1 + \left( \frac{\lambda_B}{\Delta n_{eff} L} \right)^2} \tag{7.9}$$

In the case of a small refractive index perturbation ($n < 10^{-4}$), where $\Delta n_{eff} \lll \lambda_B / L$, this reduces to:

$$\frac{\Delta\lambda}{\lambda} \rightarrow \frac{\lambda_B}{\Delta n_{eff} L} \tag{7.10}$$

Whilst in the case of a strong refractive index perturbation ($n > 10^{-4}$), this reduces to:

$$\frac{\Delta\lambda}{\lambda} \rightarrow \frac{\Delta n_{eff}}{n_{eff}} \tag{7.11}$$

So the bandwidth is directly related to the length of the grating structure in the case of a small refractive index variation and to the refractive index contrast in the case of a strong refractive index perturbation.

## 7.3 Review of grating definition techniques

Although lasers have been produced using external gratings defined in the cladding [20], the gratings used nowadays are mainly UV-written in the core. Since Meltz et al. reported grating fabrication by side exposure [6], a number of variations have been developed. They used two intersecting beams to create an interference pattern in the focal plane of approximately $4mm$ length and $125\mu m$ width. The length of the grating was inherently limited by the spot size. The angle of intersection could be modified, allowing different grating periods to be written. Reflection gratings were demonstrated between 571 and $600nm$.

An important improvement was the development of phase masks as a component of the interferometer. It is a relief grating etched in a material transparent at the writing wavelength such as silica [3]. The incident beam is diffracted by the mask such that the zero-order is minimised and the diffracted first orders are maximised [1]. The interference of the plus and minus first order creates a diffraction pattern. This leads to a permanent refractive index perturbation with a refractive index difference as high as $6 \times 10^{-4}$ [21] and allows higher tolerance on the coherence of the writing beam. This technique was refined in 1995 through the introduction of mask translation and beam scanning relative to a fibre [22]. This allows the fabrication of chirped and apodised gratings as well as conventional Bragg reflectors.

A point-by-point technique was also developed by Malo et al. [23, 24] where each laser illumination is used to define a single grating plane. The fibre is then translated by a distance equivalent to the grating period in a direction parallel to the fibre axis and the following grating plane written. A very stable and precise translation system is compulsory to obtain a grating.

Gratings have been produced in planar geometry by similar techniques [25–27]. The gratings can be written in a RIE defined channel using a phase mask [25] or on top of a previously UV-written channel using two-beam interference [28] or a phase mask [29]. The gratings defined in the work done for the remainder of this chapter have been written using the direct grating writing technique (DGW) described in section 5.4.

## 7.4 Results in rare-earth doped channels

The characterisation set-up used for gratings is described in figure 7.2. Two light sources can be used: an EDFA based ASE source giving high power signal in a 1520 to 1570$nm$ range, or an LED broad-band source, giving low power from 1300 to 1700$nm$. The signal goes through a fibre polariser then a manual polarisation controller which can be used to select which mode will be excited: TE or TM. This can only be executed with the ASE source as the broadband source intensity is too low. The fibre is butt-coupled to the sample and index-matching oil is used to improve the coupling efficiency and reduce Fabry-Perot oscillations due to the reflections of the signal in the fibre-sample cavity. The input fibre and sample are positioned using high-precision, 3-dimension, translation stages. Power reflected from the gratings goes back through the polariser and is re-directed by the coupler onto an OSA so that the reflected signal can be plotted and examined. The transmitted signal can be imaged onto an infra-red camera through a microscope objective to optimise the launching conditions. If required, the microscope objective can be removed and the transmitted signal collected with a fibre and directed onto an OSA to be analysed.

In the remainder of this section, the results obtained for gratings UV-written in the doped samples presented earlier are listed and analysed. Firstly, the transmission spectra are given. Secondly, the reflection spectra from the Bragg gratings are reviewed. They are then compared to reflection spectra from similar undoped samples. In the following section, simulations of transmission of our waveguide are presented to confirm the multimode behaviour observed in the gratings. Finally, a study of the dispersion and the wavelength dependence of the effective refractive index is given.

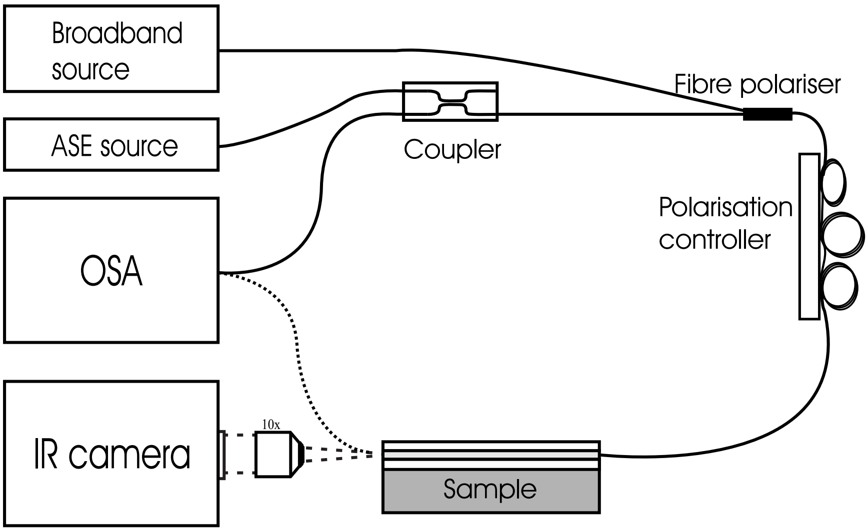

Figure 7.2: Grating characterisation set-up

### 7.4.1 Grating measurements in transmission

The transmission spectra of gratings were observed to estimate the strength of the output coupler available through UV-writing. Unfortunately, as was noted in section 5.6.5, the waveguides are multimode. In this case, the grating couples the incident light in different counter-propagating modes hence reducing its efficiency at a given wavelength as can be observed in figure 7.3.

The same effect is expected to happen in neodymium doped samples. It is not clear in the case of figure 7.4 probably because the fundamental mode amplitude is so small that the dips at other wavelengths are not noticeable.

To confirm that the dip in figure 7.4 corresponds to the actual grating strength and is not due to low signal to noise ratio, the reflectivity of the grating can be calculated from its bandwidth. On the graph, the strength of the grating is measured to be approximately $0.667dB$ and its bandwidth $0.2nm$. The reflectivity R of the grating can be expressed as [30]:

$$R = \tanh^2(\kappa L) \tag{7.12}$$

Where $L$ is the length of the grating and $\kappa$ is the coupling coefficient given

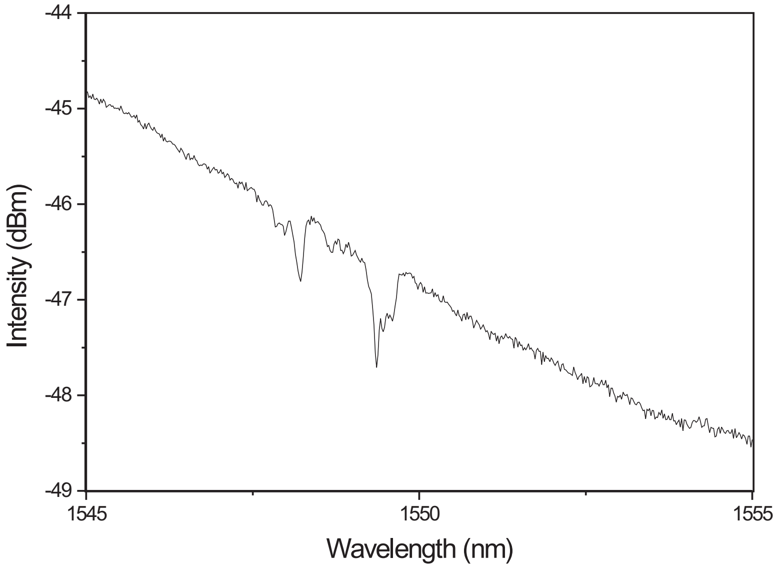

Figure 7.3: Transmission from gratings in erbium doped sample (Solution concentration 0.031M)

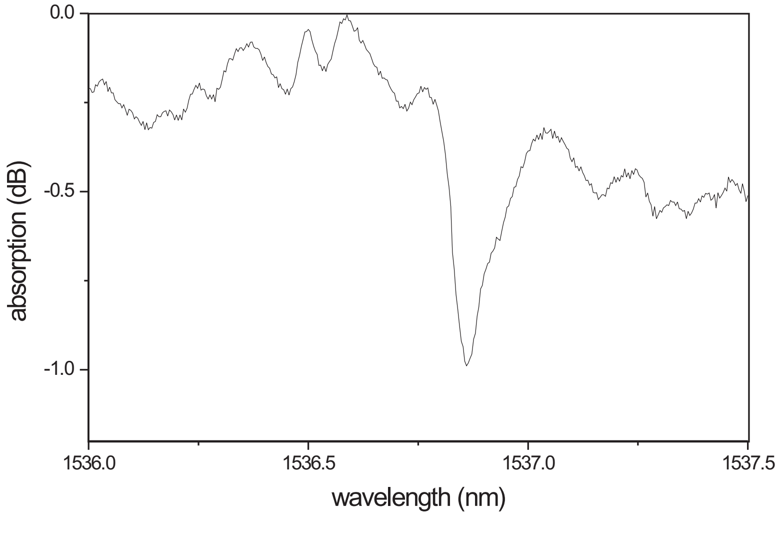

Figure 7.4: Reflection from gratings in neodymium doped sample (Solution concentration 0.011M)

by:

$$\kappa^2 \simeq \left(\frac{\Delta\lambda\ \pi n_{eff} L}{\lambda_B^2}\right)^2 \frac{1}{L^2} - \left(\frac{\pi}{L}\right)^2 \tag{7.13}$$

Where $\Delta\lambda$ is the grating bandwidth, $n_{eff}$ is the effective refractive index and $\lambda_B$ is the Bragg wavelength of the grating. Hence the calculated value for the reflection coefficient of the grating is equal to $0.6704dB$. This agrees closely to the measured value which confirms the actual value of the coupler to be 14.3%. Unfortunately, this value being so low, it is quite unlikely that a grating with that kind of strength can be used as an output coupler in the lasing experiments as we never observed lasing action from the end facet of the sample ($\approx 4\%$).

Another useful expression for the coupling coefficient can be used to calculate the refractive index variation inside the grating [30]:

$$\Delta n = \frac{\kappa \lambda_B}{I\pi} \tag{7.14}$$

Where $I$ is a transverse overlap integral of the modal distribution with the region where the grating is formed ($\leq 1$). It accounts for the fact that only the field propagating in the core region interacts with the grating. It is assume to be equal to 1 in this case. In this case, the refractive index change responsible for the grating is calculated to be approximately $4.3 \times 10^{-5}$ which is inside the typical values range [1].

### 7.4.2 Grating measurements in reflection

The reflection spectra were plotted for 2 neodymium doped samples, an ytterbium doped sample and an erbium doped sample, for comparison purposes (See figures 7.5 to 7.8). One of the neodymium doped samples was fabricated using a $0.011M$ solution of neodymium, the other using a $0.00875M$ solution. All gratings were written with a period of $528nm$ and a writing power of $100mW$. The variation in refractive index between samples doped with different solutions has been mentioned earlier (see section

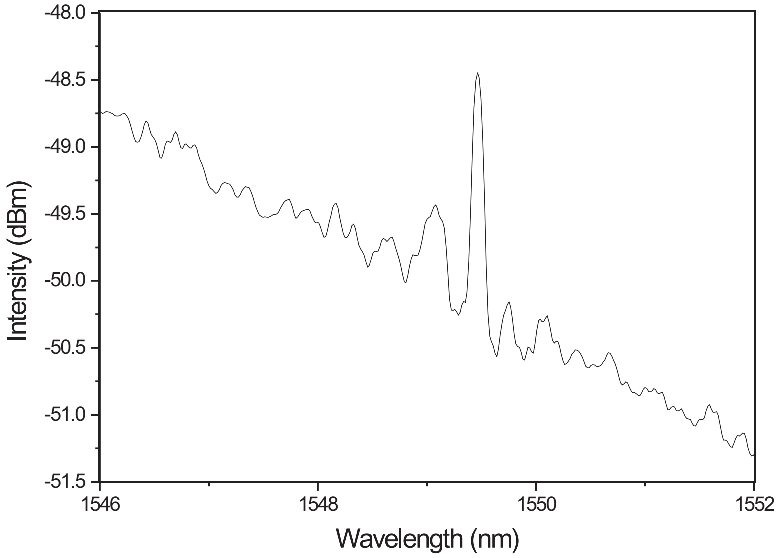

Figure 7.5: Reflection from gratings in neodymium doped sample (Solution concentration 0.011M)

5.5) and implies a difference in effective refractive index between the samples. As seen in the theory section (equation 7.3), the reflected wavelength can be expressed as the product of the effective refractive index and twice the grating period. Hence the centre wavelength varies between samples, with values ranging between 1548 and 1551$nm$.

Instead of having one clear reflection peak, the spectra are noticeably noisier around the Bragg wavelength which once again denotes the multimode behaviour of the gratings. This is much more obvious for the 0.00875$M$ neodymium doped sample than for the others. Nevertheless, the strength of all the gratings is comparable with a value of about 2$dB$ in reflection which indicates that there is very little variation of photosensitivity between samples doped with different ions and/or concentrations.

Gratings were also written on top of already defined channel waveguide but the strength was comparable to that of those mentioned earlier although the spectrum was not as noisy (see figure 7.9).

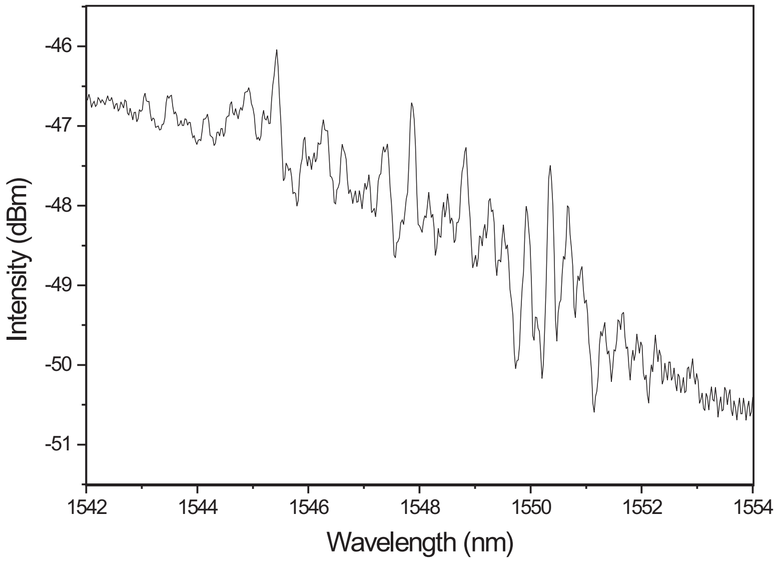

Figure 7.6: Reflection from gratings in neodymium doped sample (Solution concentration 0.00875M)

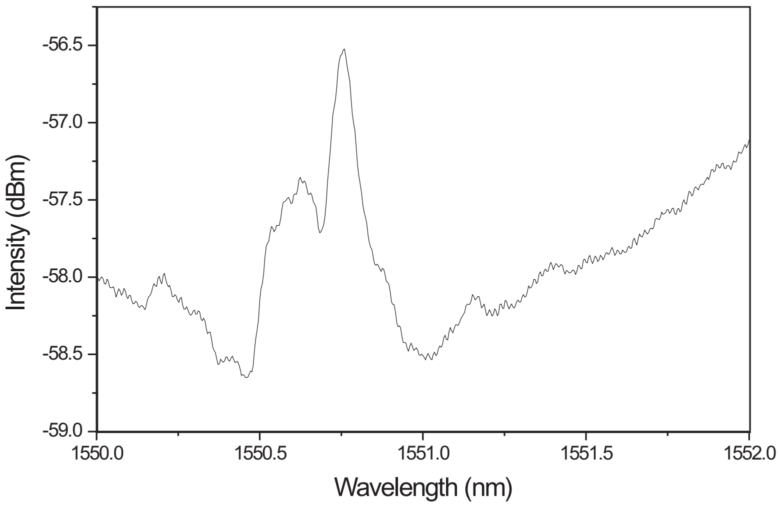

Figure 7.7: Reflection from gratings in erbium doped sample

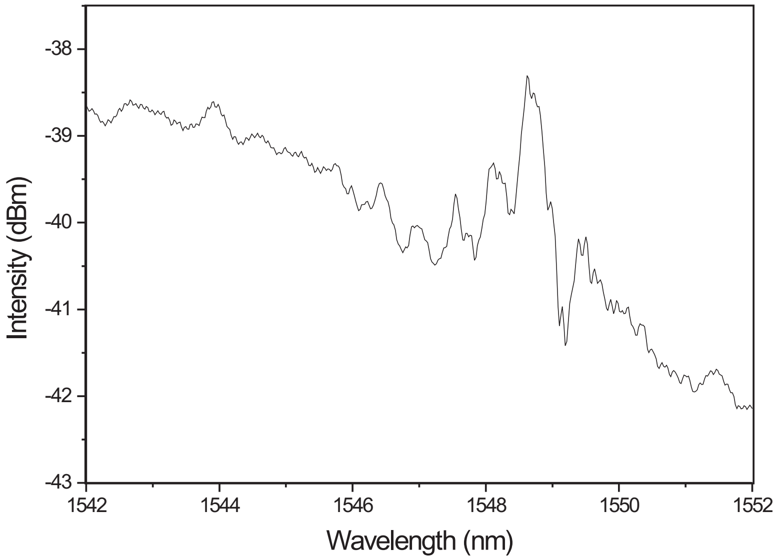

Figure 7.8: Reflection from gratings in ytterbium doped sample (Solution concentration 0.011M)

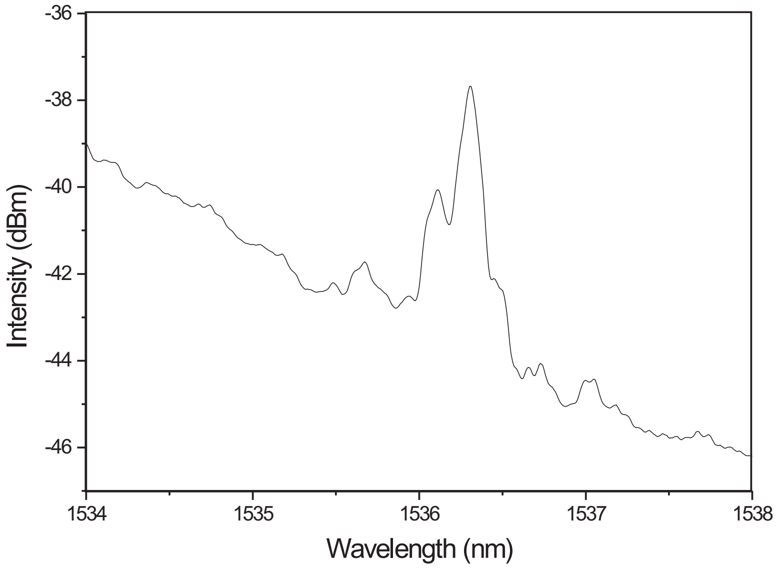

Figure 7.9: Reflection from gratings overwritten on previously defined channel in neodymium doped sample (Solution concentration 0.011M)

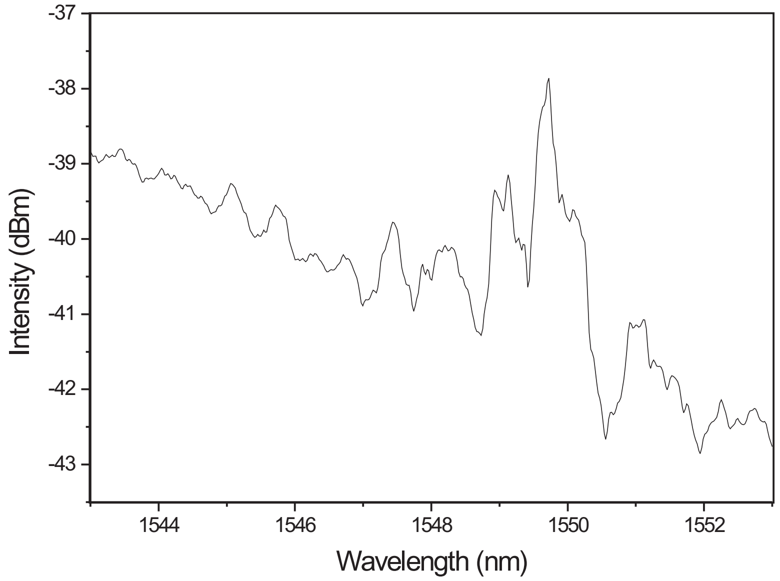

Figure 7.10: Reflection from grating in an undoped sample

### 7.4.3 Comparison with gratings in undoped material

In order to investigate the effect of solution doping, the grating spectrum of undoped samples is compared to those presented in the previous subsection. Once again the period used for the gratings was $528nm$ and the writing power was $100mW$.

It can be noted that once more, the peak wavelength and the strength of the grating are very similar to those of gratings written in solution doped samples. This is one more indication that the solution doping process does not seem to affect the photosensitivity of the sample as was hinted in section 5.6.4.

### 7.4.4 Modelling and comparisons with experiments

The grating spectra presented above indicate that the waveguides created are multimode. To confirm this hypothesis, a number of modelling studies were performed. They are based on the effective index method described in chapter 2, where the channel is effectively separated in three planar waveguides for which the effective refractive index is independently calculated. This in turn is considered to be a slab waveguide of its own for which the effective refractive index can easily be deduced, giving an approximation of the channel waveguide effective refractive index. Although this is obviously not an absolutely accurate method, it has the advantage of simplifying considerably the mathematics needed to obtain a reasonably good approximation.

The most relevant simulations are described here. They use the parameters of the laser channel waveguide described in chapter 6. The refractive index value is 1.4641 for the cladding layers and 1.482 for the core slab to account for the refractive index difference due to UV writing. For a core size of 4$\mu m$, the channel waveguide is found to sustain two modes at 1050nm (figure 7.12) and two at 1550$nm$. The core size was decreased to 2$\mu m$ and the number of propagating modes was found to be reduced to 1 (figure 7.11). Reducing the refractive index difference induced by UV writing was found not to reduce the number of modes.

The other possibility to reduce the number of modes was found to be a decrease in the refractive index difference between cladding and core layer. This can be verified using the following equation to calculate the number of modes [31]:

$$N_{modes} \leq \left(\frac{2D\ NA}{\lambda}\right) + 1 \tag{7.15}$$

Where $D$ is the size of the waveguide and $\lambda$ is the signal wavelength. Unfortunately, the fabrication of three layer samples with a thinner core layer or better index-matched 3 layer samples was not possible due to the lack of availability of the FHD system at that stage of the project.

### 7.4.5 Effective index measurements

The fabrication of gratings with a Bragg wavelength of 1550$nm$ has been reported earlier in this section. In order to use Bragg gratings as output

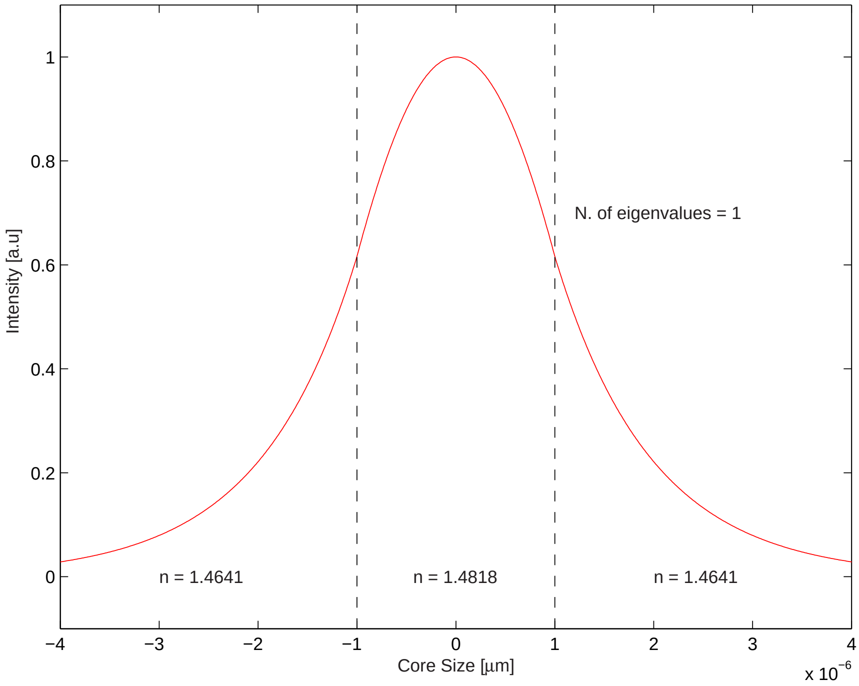

Figure 7.11: Modelling at 1050nm with a 2$\mu m$ core

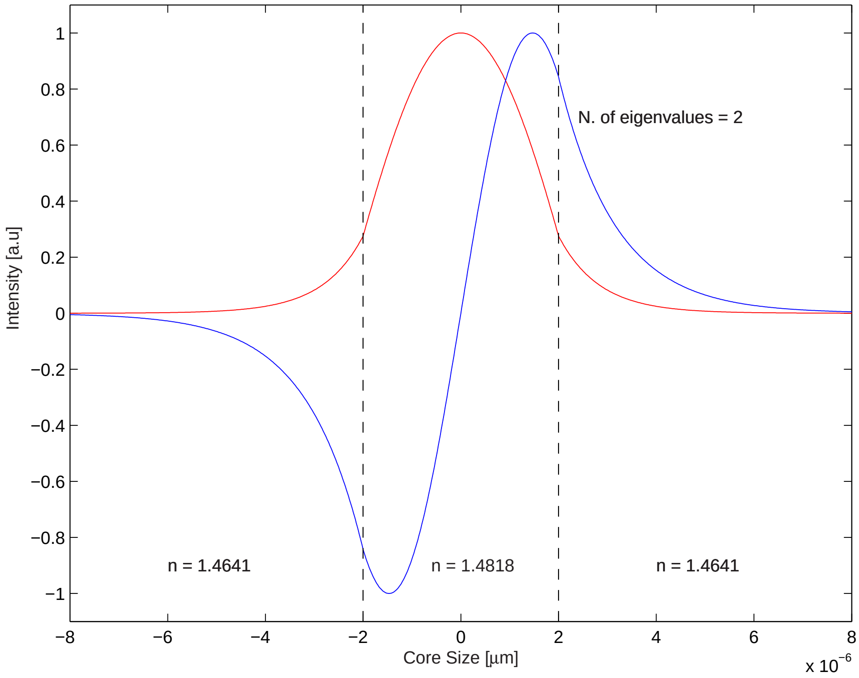

Figure 7.12: Modelling at 1050nm with a 4$\mu m$ core

couplers, the Bragg wavelength must be the same as the lasing wavelength (i.e. $1050nm$ for the laser reported in chapter 6). The following equation proves to be crucial:

$$\lambda_B = 2\Lambda n_{eff} \tag{7.16}$$

Where $\lambda_B$ is the Bragg wavelength and $\Lambda$ is the grating period. If a grating is fabricated with a given period, its characterisation will unveil its Bragg wavelength. Hence the exact effective refractive index can be calculated. Yet, the refractive index is wavelength dependent. In order to obtain the grating period needed for the Bragg wavelength of a grating to be $1050nm$ in this waveguide, a set of gratings with different periods have been written in the sample and characterised. The grating periods used were 532, 530, 528, 525, 523, 510, 493, 476 and $459nm$. The relation between grating period and Bragg wavelength can be seen in figure 7.13. By extrapolating this plot, the value for the grating period needed for the Bragg wavelength to be $1050nm$ can be deduced and a value of $355.64nm$ is found. The effective refractive index of this material can be calculated using equation 7.16. It is estimated to be 1.4762.

The effective refractive index has been calculated for all the grating characterised and is plotted versus the grating period in figure 7.14. Some gratings have been written around $1.3\mu m$ and between 1 and $1.1\mu m$ ; unfortunately, due to the lack of suitable light source, they could not be characterised.

### 7.4.6 Dispersion

When light of spectral width $\Delta\lambda_0$ propagates through a waveguide, the wavelength-dependent refractive index causes the broadening of the pulse [32]. This is called the total dispersion of the guiding structure, which comprises the material dispersion and the waveguide dispersion, and it can be approximated by characterising gratings over a wide spectral range. The measurement of the wavelength reflected by the gratings allows one to

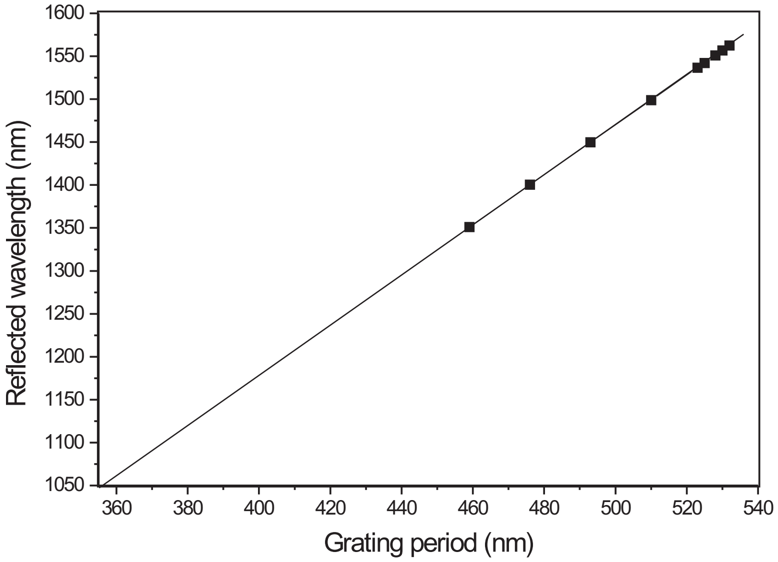

Figure 7.13: Reflected wavelength dependence on grating period

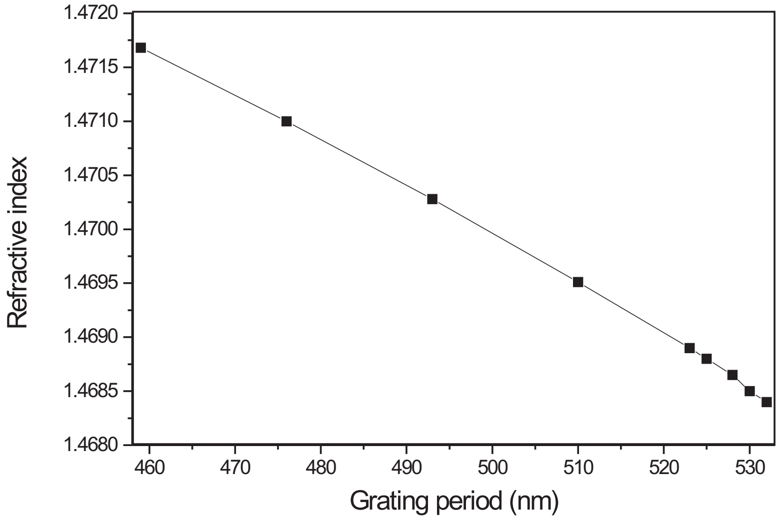

Figure 7.14: Effective index versus grating period

calculate the effective index at different wavelength, from which the total dispersion can be approximated. However, the main component being due to material dispersion, our results will be compared to material dispersion of pure silica [30] and commercial FHD samples [19].

#### 7.4.6.1 Refractive index dependence

A light pulse propagates through a homogeneous medium with a group velocity $v_g$ given by [30]:

$$\frac{1}{v_g} = \frac{1}{c}\left(n(\lambda_0) - \lambda_0 \frac{dn}{d\lambda_0}\right) \tag{7.17}$$

Where $\lambda_0$ is the free-space wavelength and c is the velocity of light. Hence a pulse will propagate through a length of material $L$ in an amount of time $\Delta(\lambda_0)$ which is wavelength dependent, defined by [33]:

$$\tau(\lambda_0) = \frac{L}{v_g} = \frac{L}{c}\left(n(\lambda_0) - \lambda_0 \frac{dn}{d\lambda_0}\right) \tag{7.18}$$

Thus each wavelength component will propagate through the sample with a different group velocity. This creates a broadening of the pulse. If the source exhibits a spectral width $\Delta\lambda_0$, the broadening can be expressed as follows [34]:

$$\Delta\tau = \frac{d\tau}{d\lambda_0}\Delta\lambda_0 = -\frac{L}{c}\left(\lambda_0^2 \frac{d^2n}{d\lambda_0^2}\right)\left(\frac{\Delta\lambda_0}{\lambda_0}\right) \tag{7.19}$$

This broadening is called *material dispersion*. It is expressed in terms of the spectral width $\Delta\lambda_0$ and the length $L$. It can also be expressed in a more general manner as the temporal broadening per length per spectral width unit [35]:

$$D_m = \frac{\Delta\tau}{L\Delta\lambda_0} = -\frac{1}{\lambda_0 c}\left(\lambda_0^2 \frac{d^2n}{d\lambda_0^2}\right) \times 10^9 \tag{7.20}$$

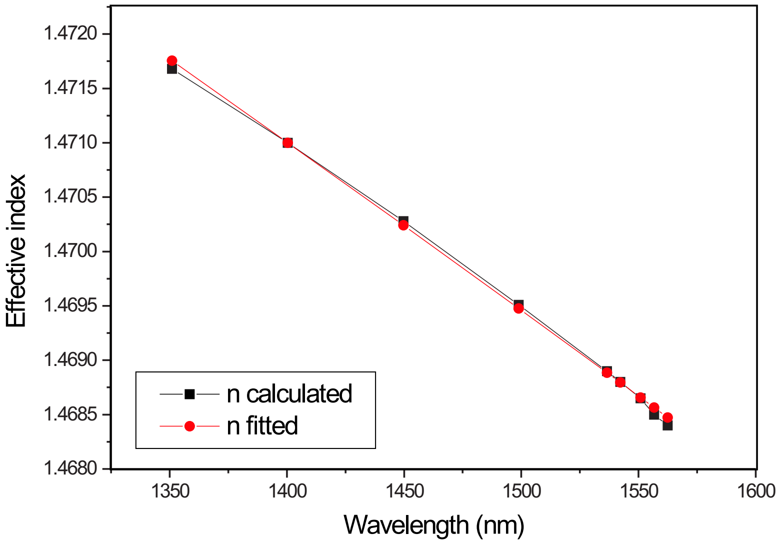

Figure 7.15: Effective index dependence on wavelength

Where $c = 3.10^5 km/s$, $\lambda$ is expressed in micrometers and $D_m$ in picoseconds per kilometer per nanometer (ps/km.nm). The modal confinement from the waveguide also affects the dispersion although it is negligible compared to the material dispersion [19].

#### 7.4.6.2 Measurement of total dispersion

The variation of effective refractive index with the wavelength is presented for the data calculated from the measured reflected wavelengths and fitted data in figure 7.15. It can be expressed by Sellemeier's equation [30]:

$$n^2(\lambda_0) = 1 + \frac{b_1\lambda_0^2}{\lambda_0^2 - a_1} + \frac{b_2\lambda_0^2}{\lambda_0^2 - a_2} + \frac{b_3\lambda_0^2}{\lambda_0^2 - a_3} \tag{7.21}$$

From the fitting of exponential values, the constants, which are different for each material, are deduced. They are listed in table 7.1.

Using these constants, the fitted plot is derived twice and used in equation 7.20. It is plotted in figure 7.16. The dispersion of pure silica [30] and of a typical commercial germanium-doped three-layer FHD sample [19] are

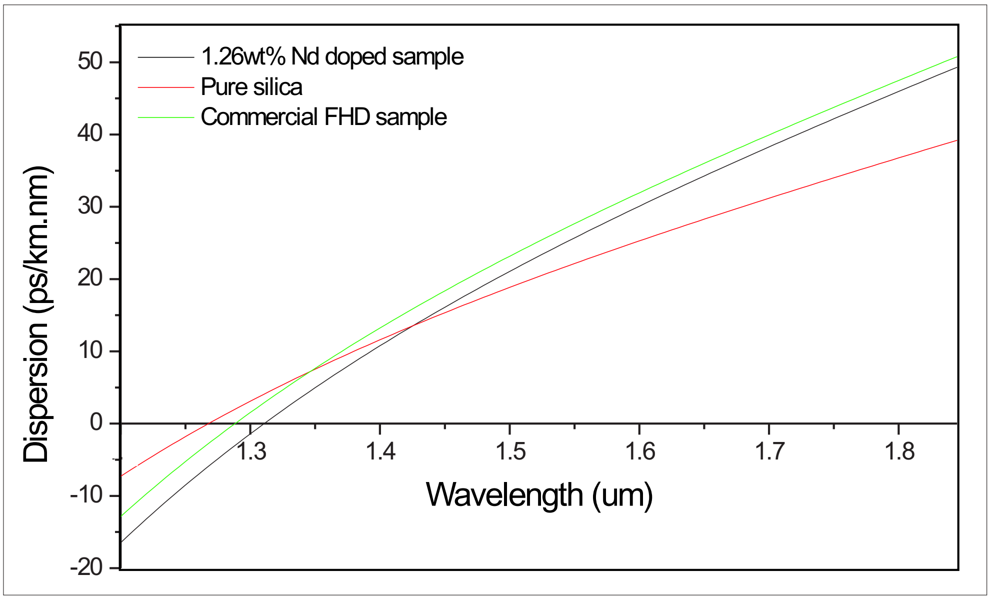

Figure 7.16: Dispersion of Nd-doped material, pure silica [30] and commercial photosensitive three-layer FHD sample [19].

| constant | 1 | 2 | 3 |
|---|---|---|---|
| a | 0.007174269 | 0.017887296 | 97.93111648 |
| b | 0.731467728 | 0.449750623 | 1.184405516 |

Table 7.1: Constants $a_1$, $a_2$, $a_3$, $b_1$, $b_2$ and $b_3$ for Sellemeier's equation from fitted data.

plotted as well for reference.

In the sample doped with $1.26wt\%$ of neodymium, the point of minimum dispersion, called the zero material dispersion point, is found for a wavelength of $1310nm$.

## 7.5 Summary

This chapter began with a brief historical perspective of UV-written gratings in silica including the discovery and refinement of this technique and its possible applications in the field of lasers. The basic theory necessary to the understanding of Bragg gratings was then described. This was followed by a review of the fabrication techniques before the results obtained during the course of this work were detailed. This included the reflection and transmission spectra of the gratings defined in the rare-earth doped samples fabricated. The typical reflection spectrum of such a Bragg grating inscribed in an undoped sample was then given for the purpose of photosensitivity comparison between similar doped and undoped samples. The process of doping was found not to affect the photosensitivity of the sample, as was mentioned in section 5.6.4. Some modelling of propagation in the channel waveguides was performed to confirm that the channels sustain the propagation of various modes at 1050 and $1550nm$ as was suggested by the grating responses.

This implies that a DFB laser cannot be fabricated in these samples as the reflection obtained for the fundamental mode is too weak. It also demonstrates that in order to get monomode propagation in the channel waveguide, the core layer thickness has to be reduced under a two microns value or the composition of the three-layer system has to be modified so the refractive index difference between cladding and core is reduced. Unfortunately, this could not be achieved during the course of this work due to the unavailability of the FHD system towards the final stages. It is believed that if the cladding compositions are modified to match the doped core refractive index, the same core composition and doping procedure could be used to create monomode channels in which the grating would be strong enough to act as an output coupler. A DFB structure would then be easily fabricated. Such a structure has been defined in our sample although it could not be characterised, as the grating was too weak to produce lasing action in the structure due to its multimode behaviour and no other light source was available that was bright enough at 1050nm.

Finally, the effective refractive index dependence on grating period and Bragg wavelength was investigated, from which the grating period corresponding to a Bragg wavelength of 1050nm and the dispersion of the material was extracted. The latest was compared to pure silica and commercially available germanium-doped three-layer FHD samples. The zero material dispersion point was found to be 1310$nm$.

## 7.6 References

[1] A. Othonos and K. Kalli. Fiber Bragg gratings: Fundamentals and applications in telecommunications and sensing. *Artech house, Inc.*, 1999.

[2] K.O. Hill, Y. Fujii, D.C. Johnson and B.S. Kawasaki. Photosensitivity in optical fiber waveguides: Application to reflection filter fabrication. *Applied Physics Letters*, 32(10) : p647–649, 1978.

[3] R. Kashyap. Fiber Bragg gratings. *Academic press*, 1999.

[4] J. Bures, S. Lacroix and J. Lapierre. Reflecteur de Bragg induit par photosensibilite dans une fibre optique: modele de croissance et reponse en frequence *Applied Optics*, 21(19) : p3502–3506, 1982.

[5] D.K.W. Lam and B.K. Garside. Characterisation of single-mode optical fiber filters. *Applied Optics*, 20(3) : p440–445, 1981.

[6] G. Meltz, W.W. Morey and W.H. Glenn. Formation of Bragg gratings in optical fibers by a transverse holographic method. *Optics Letters*, 14(15) : p823–825, 1989.

[7] R. Kashyap, J.R. Armitage, R. Wyatt, S.T. Davey and D.L. Williams. All-fibre narrowband reflection gratings at $1500nm$. *Electronics Letters*, 26(11) : p730–732, 1990.

[8] G.A. Ball, W.W. Morey and W.H. Glenn. Standing-wave monomode erbium fiber laser. *IEEE Photonics Technology Letters*, 3(7) : p613–615, 1991.

[9] J.L. Zyskind, V. Mizrahi, D.J. DiGiovanni and J.W. Sulhoff. Short single frequency erbium-doped fibre laser. *Electronics Letters*, 28(15) : p1385–1387, 1992.

[10] V. Mizrahi, D.J. DiGiovanni, R.M. Atkins, S.G. Grubb, Y.K. Park and J.P. Delavaux. Stable single-mode erbium fiber-grating laser for digital communication. *Journal of Lightwave Technology*, 11(12) : p2021–2025, 1993.

[11] J.T. Kringlebotn, J.L. Archambault, L. Reekie and D.N. Payne. $Er^{3+}$ : $Yb^{3+}$-codoped fiber distributed-feedback laser. *Optics Letters*, 19(24) : p2101–2103, 1994.

[12] A. Asseh, H. Storoy, J.T. Kringlebotn, W. Margulis, B. Sahlgren, S. Sandgren, R. Stubbe and G. Edwall. $10cm$ $Yb^{3+}$ DFB fibre laser with permanent phase shifted grating. *Electronics Letters*, 31(12) : p969–970, 1995.

[13] J.L. Archambault and S.G. Grubb. Fibre gratings in lasers and amplifiers. *Journal of Lightwave Technology*, 15(8) : p1378–1390, 1997.

[14] T. Voss, D. Scheel and W. Schade. A microchip-laser-pumped DFB-polymer-dye laser. *Applied Physics B: Lasers and Optics*, B 73 : p105–109, 2001.

[15] J. Hubner, S. Guldberg-Kjaer, M. Dyngaard, Y. Shen, C.L. Thomsen, S. Balslev, C. Jensen, D. Zauner and T. Feuchter. Planar Er- and Yb-doped amplifiers and lasers. *Applied Physics B: Lasers and Optics*, B 73 : p435–438, 2001.

[16] X. Zhu and D. Lo. Sol-gel glass distributed feedback waveguide laser. *Applied Physics Letters*, 80(6) : p917–919, 2002.

[17] J. Hubner, P. Varming and M. Kristensen. Five wavelength DFB fibre laser source for WDM systems. *Electronics Letters*, 33(2) : p139–140, 1997.

[18] M. Ibsen, S. Alam, M.N. Zervas, A. Grudinin and D.N. Payne. 8- and 16-channel all-fibre DFB laser WDM transmitters with integrated pump redundancy. *IEEE Photonics Technology Letters*, 11(9) : p1114–1116, 1999.

[19] G.D. Emmerson. Novel direct UV written devices. *PhD thesis, University of Southampton*, 2003.

[20] I.M. Jauncey, L. Reekie, R.J. Mears, D.N. Payne, C.J. Rowe, D.C.J. Reid, I. Bennion and C. Edge. Narrow-linewidth fibre laser with integral fibre grating. *Electronics Letters*, 22(19) : p987–988, 1986.

[21] K.O. Hill, B. Malo, F. Bilodeau, D.C. Johnson and J. Albert. Bragg gratings fabricated in monomode photosensitive optical fiber by UV exposure through a phase mask. *Applied Physics Letters*, 62(10) : p1035–1037, 1993.

[22] M.J. Cole, W.H. Loh, R.I. Laming, M.N. Zervas and S. Barcelos. Moving fibre/phase mask-scanning beam technique for enhanced flexibility in producing fibre gratings with uniform phase mask. *Electronics Letters*, 31(17) : p1488–1489, 1995.

[23] K.O. Hill, B. Malo, K.A. Vineberg, F. Bilodeau, D.C. Johnson and I. Skinner. Efficient mode conversion in telecommunication fibre using externally written gratings. *Electronics Letters*, 26(16) : p1270–1272, 1990.

[24] B. Malo, K.O. Hill, F. Bilodeau, D.C. Johnson and J. Albert. Point-by-point fabrication of micro-Bragg gratings in photosensitivity fibre using single excimer pulse refractive index modification technique. *Electronics Letters*, 29(18) : p1668–1669, 1993.

[25] G.D. Maxwell, R. Kashyap, G. Sherlock, J.V. Collins and B.J. Ainslie. Demonstration of a semiconductor external cavity laser using a UV written grating in a planar silica waveguide. *Electronics Letters*, 30(18) : p1486–1487, 1994.

[26] M. Ibsen, J. Hubner, J.E. Pedersen, R. Kromann, L.-U.A. Andersen and M. Kristensen. $30dB$ sampled gratings in germanosilicate planar waveguides. *Electronics Letters*, 32(24) : p2233–2235, 1996.

[27] T. Tanaka, H. Takahashi, M. Oguma, T. Hashimoto, Y. Hibino, Y. Yamada, Y. Itaya, J. Albert and K.O. Hill. Integrated external cavity laser composed of spot-size converted LD and UV written grating in silica waveguide on Si. *Electronics Letters*, 32(13) : p1202–1203, 1996.

[28] K.O. Hill and G. Meltz. Fibre Bragg grating technology fundementals and overview. *Journal of Lightwave Technology*, 15(8) : p1263–1275, 1997.

[29] M. Svalgaard. Ultraviolet light induced refractive index structures in germanosilica. *PhD thesis, Technical University of Denmark*, 1997.

[30] A. Ghatak and K. Thyagarajan. Introduction to fiber optics. *Cambridge University Press*, 1998.

[31] T. Bhutta. Novel rare-earth doped planar waveguide lasers. *PhD thesis, University of Southampton*, 2002.

[32] J.T. Verdeyen. Laser electronics. *Prentice-Hall international editions*, 1989.

[33] O. Svelto. Principles of lasers. *Plenum Press*, 1989.

[34] D.L. Lee. Electromagnetic Principles of Integrated Optics. *J. Wiley & Sons*, New York, Ch.2, 1986.

[35] B.E.A. Saleh and M.C. Teich. Fundamentals of photonics. *J. Wiley & Sons*, 1991.

# Chapter 8

# Conclusion

The first all-UV-written laser in silica-on-silicon was demonstrated during the work described in this thesis, using neodymium ions. The fabrication process involves a combination of flame hydrolysis deposition (FHD), solution doping and UV writing techniques. It exhibited high efficiency operation, better or comparable to previously reported neodymium-doped lasers in silica-on-silicon fabricated with different channel definition techniques [1–3].

This laser possesses all the inherent benefits of silica-on-silicon technology and of channel waveguide geometry but also exhibits extra advantages due to the fabrication process. First of all, the laser is fabricated within the ORC, from glass fabrication to laser testing. Thanks to the versatile nature of FHD and solution doping, countless compositions can be fabricated, allowing a number of rare-earth ions to be used and permitting a quick and simple optimisation of the material. Also, UV-writing is a one-step process whose serial nature makes it very suitable for prototyping. This makes it a very time and cost effective method compared to, for instance, RIE definition and lithography. Nevertheless, a number of lasers were fabricated, showing the repeatability of the process. Finally, grating fabrication, again by UV writing technique, is possible, allowing a number of laser configurations useful for WDM technology to be fabricated, including DBR and DFB structures or laser arrays.

## 8.1 Summary

The work related here is presented as a progression through the steps leading to a new technique for the fabrication of lasers:

- FHD technique is used to fabricate photosensitive glass suitable for UV writing of channel waveguides. Chapter three establishes the comparative benefits of various glass fabrication techniques and introduces the FHD system and principles. A suitable sample for this projects requires a system comprising three layers of appropriate refractive index with a decreasing consolidation temperature. To obtain such a set of compositions, a three-dopant system is used. A boron-chloride source had to be added to the existing FHD that used germanium and phosphorus as co-dopants.

- Rare-earth doping of the core layer was performed in order to create active devices. A number of fabrication techniques are available although solution doping was found to be the most versatile as well as the easiest to implement. Different apparatus were developed and compared to obtain the best layers possible. The different parameters influencing the resulting layers were also studied in detail. For consistency, it was decided that all parameters should be kept constant between different samples, except for the solution concentration when other doping levels were required.

- Optimum conditions for channel waveguides definition were found and used throughout the work related here. A spectroscopic study of the rare-earth doped materials fabricated was realised and characteristics such as absorption spectra, fluorescence spectra and fluorescence lifetime were reviewed for samples doped with neodymium, erbium, thulium and ytterbium. Physical properties of the channels were also looked into such as numerical aperture and mode profiles. Y-splitters were also fabricated and characterised to prove the feasability of UV writing of more complicated structures in rare-earth doped material making structures such as laser arrays possible.

- External cavity thin film mirrors were used as output couplers to obtain laser action in a neodymium-doped sample. Thresholds as low as $4mW$ and slope efficiencies as high as $33\%$ were witnessed and the waveguide laser was studied. This includes lasing spectra, output mode profile and polarisation of the laser. Propagation loss values were calculated from the threshold and slope efficiency results, and the Findlay-Clay analysis was performed to confirm those. An upper limit for the loss was calculated to be $0.8dB/cm$ with the actual value thought to be in the 0.11-0.3$dB/cm$ range.

The work presented here can be seen as the ground work of a more ambitious project. To establish the potential of this technique for grating-based lasers development and DFB-laser arrays for WDM technology, some extra experiments have been realised. Erbium-doped samples have been developed although no lasing was observed. Bragg gratings have been inscribed with theoretical reflected wavelengths in the 1050-1570$nm$ range, including DBR structures. Finally, a DFB structure formed by a continuous grating including an asymmetrically positioned $\pi/2$ phase shift. Unfortunately, lasing action was not observed in these structures, as the strength of these gratings was too weak. Therefore, due to the lack of light sources bright enough at wavelengths below 1300$nm$, only gratings with a Bragg wavelength superior to this value could be characterised.

## 8.2 Future work

It has been established that the waveguides produced during the course of this work exhibited multimode behaviour. As a consequence, the transmission spectra shows a dip of under one decibel at the Bragg wavelength. Previous work by other members of the group has demonstrated single-mode grating responses in transmission of over $30dB$ [4, 5]. In the case presented here, the cause for the waveguides being multimode is the increase in refractive index due to the rare-earth doping of layers. Hence, the core thickness has to be reduced under two micron or new cladding compositions have to be developed in order to reduce this refractive index difference. This would make the waveguides monomode and allow the use of Bragg gratings as output couplers or DFB structures. Unfortunately, the lack of availability of the FHD system in the last stages of this work prevented us from developing new suitable samples.

Once DFB lasers are developed, creating a laser array should be straightforward as the grating period can easily be modified and y-splitters have been fabricated that could allow a single pump signal to be used to pump many lasers simultaneously.

Also, sources at different wavelengths including 1530-1560$nm$ for WDM telecom technology may be developed by using rare-earth ions other than neodymium. Thulium, ytterbium and erbium have been used during the course of this work but no lasing action was observed. This is thought to be mainly due to too low a doping level. The study of higher doping levels and sensitisation of erbium ions using ytterbium co-doping [6] should be studied to provide lasing action. Another possibility is to modify the core layer composition as the phosphorus content affects the spectroscopy of the rare-earth ions [7,8].

## 8.3 References

[1] Y. Hibino, T. Kitagawa, M. Shimizu, F. Hanawa and A. Sugita. Neodymium-doped silia optical waveguide laser on silicon substrate. *IEEE Photonics Technology Letters*, 1(11) : p349–350, 1989.

[2] J.R. Bonar, J.A. Bebbington, J.S. Aitchison, G.D. Maxwell and B.J. Ainslie. Low threshold Nd doped silica planar waveguide laser. *Electronics Letters*, 30(3) : p229–230, 1994.

[3] T. Kitagawa, K. Hattori, Y. Hibino and Y. Ohmori. Neodymium-doped silica based planar waveguide lasers. *Journal of Lightwave Technology*, 12(3) : p436–442, 1994.

[4] S.P. Watts. Flame Hydrolysis Deposition of photosensitive silicate layers suitable for the definition of waveguiding structure through direct ultraviolet writing. *PhD thesis, University of Southampton*, 2002.

[5] G.D. Emmerson. Novel direct UV written devices. *PhD thesis, University of Southampton*, 2003.

[6] E. Snitzer and R. Woodcock. $Yb^{3+} - Er^{3+}$ glass laser. *Applied Physics Letters*, 6 : p45–46, 1965.

[7] K. Arai, H. Namikawa, K. Kumata and T. Honda. Aluminium or phosphorus co-doping effects on the fluorescence and structural properties of neodymium-doped silica glass. *Journal of Applied Physics*, 59(10) : p3430–3436, 2002.

[8] M.J.F. Digonnet. Rare-earth doped fiber lasers and amplifiers. *Marcel Dekker, Inc.*, 2001.

# Appendix A

# List of Publications

## A.1 Journal Publication

D.A. Guilhot, G.D. Emmerson, C.B.E. Gawith, S.P. Watts, D.P. Shepherd, R.B. Williams and P.G.R. Smith. Single mode direct-UV-written channel waveguide laser in neodymium-doped silica on silicon. *Optics Letters*, 29(9) : p947–949, 2004.

## A.2 Conference Publications

**D.A. Guilhot**, G.D. Emmerson, C.B.E. Gawith, D.P. Shepherd, R.B. Williams and P.G.R. Smith. Channel waveguide laser in neodymium doped silica-on-silicon by direct-UV-writing. *CLEO*, San Francisco, 16–21 May, 2004, CTuD5.

**D.A. Guilhot**, G.D. Emmerson, C.B.E. Gawith, D.P. Shepherd and P.G.R. Smith. Fabrication of a single mode laser by UV-writing in neodymium doped silica-on-silicon. *Europhoton*, Lausanne, 29 August–3 Sept., 2004. ThD5.

**P.G.R. Smith**, G.D. Emmerson, C.B.E. Gawith, R.B. Williams, D.A. Guilhot, I.J.G. Sparrow and M.F.R. Adikan. All-UV written integrated glass devices including planar Bragg gratings and lasers. *XX International Congress on Glass (ICGXX)*, Kyoto, 26 Sept.–1 Oct., 2004 (Invited).